Doctoral Dissertation

2017

Investigating the role of dendrites in sparse representations in the hippocampus using computational models

Spyridon Chavlis

Department of Biology, University of Crete

and

Institute of Molecular Biology & Biotechnology, Foundation for Research and Technology Hellas

Acknowledgements

Foremost, I would like to express my sincere appreciation and thanks to my advisor, Dr. Panayiota (Yiota) Poirazi, you have been a tremendous mentor throughout these years. I would like to thank you for encouraging my research and for allowing me to grow as a research scientist and as a person. Your guidance on both research questions and personal issues has been priceless. Also, I would like to thank you for giving me the opportunity to be a part of your lab and make my dream true by doing my PhD in such a delightful field. I could not have imagined having a better advisor and mentor for my Ph.D. studies. Working with Yiota has been an invaluable experience that shaped my character and expanded my scientific horizons.

I would also like to thank my advisory committee members, Professors Kyriaki Sidiropoulou and Alessandro Treves for their encouragement, insightful comments, and hard questions during our yearly reports. Thank you very much for making a stressful process not to be a strict examination, but to be a fruitful discussion. Also, I would like to thank the members of the examination committee, Dr. Nikoletopoulou, Dr. Simos, Prof. Charalambopoulos and Prof. Delidakis for making the PhD defense such a special moment and also for their valuable comments on my dissertation.

I would like to express my sincere thanks to Dr. Panagiotis Petrantonakis for sharing his time and knowledge during the first years of my studies and also for his guidance in our first project. Also, I would like to thank Dr. Attila Losonscy and Dr. Nathan Danielson for the collaborative work we have together.

I show extensive gratitude to all of the people who warmly contributed their stories, histories, and experiences. Without this willingness to share, the research would not have even been possible. In the same vein, I would like to extend great thanks to my current and former lab members and especially to Athanasia (Nasi), Stefanos, Panagiotis, George, Alexandra, and Constantinos, who offered their time,

support and commitment. This piece of research looks very different because of their input, influence and expert knowledge.

Apart from their input to my research interests, I would like to thank Panagiotis and Nasi for the supportive role through this hard period. Always I knew that they were nearby to offer their help in personal issues and difficult times. Of course, I could not forget Alexandra for being such a patient and smiley person with whom I spend days and nights at the lab.

I would have never even embarked on this journey without the spiritual support of my closest friends and, of course, my family; my mother Efi, my grandmother Anastasia and my sister Eirini. I thank them for having faith in me and for encouraging me to go after my dreams.

Last but not least, I would like to express my honest appreciations to Garyfallia (Garito) for being to my side through the most productive years of my PhD thesis. Put it simply, I have never met anyone who believes in me more and who enables me to keep going even during the most difficult periods of my life. Thank you for making me more than I am.

Abstract

Memory formation, consolidation and recall are essential brain functions for ordinary life and these mnemonic processes are widely associated with hippocampus. Although hippocampus is a broadly studied brain region, both experimentally and computationally, the mechanisms underlie memory function remain a mystery. Hippocampus is widely hypothesized that involves in distinct mnemonic processes, such as pattern separation/completion and spatial encoding. Specifically, different regions accomplish the aforementioned tasks with dentate gyrus to be crucial for distinguishing overlapping memories, while CA1 subregion with spatial navigation and formation of the spatial map of the brain. Taking advantage of computational modeling, we implemented two different computational networks in order to reveal and study in-depth the mechanisms being key mediators during these functions. Our results indicate that sparsity is a key feature of dentate gyrus principal cells and we showed that various mechanisms could mediate this feature, such as the number of dendrites, the dendritic path-length as well as the mossy cells. In addition, we explored the role of each interneuron during spatial navigation. Our results show that each type of interneuron has a distinct role during place cell formation, with PV^+ and VIP^+/CCK^+ basket cells being more critical. Our model generates a number of experimentally testable predictions that may lead to a better understanding of the physiological and pathological function of hippocampus.

Abstract in Greek

Ο σχηματισμός, η αποθήκευση και η ανάκληση της μνήμης είναι απαραίτητες λειτουργίες του εγκεφάλου για την καθημερινή ζωή. Συγκεκριμένα, αυτές οι μνημονικές διαδικασίες συνδέονται ευρέως με τον ιππόκαμπο. Αν και ο ιππόκαμπος είναι μια πλήρως μελετημένη περιοχή του εγκεφάλου, τόσο σε πειραματικό επίπεδο όσο και με χρήση υπολογιστικών μοντέλων, οι ακριβείς μηχανισμοί που εμπλέκονται στη λειτουργία της μνήμης παραμένουν ένα άλυτο μυστήριο. Ο ιππόκαμπος υποτίθεται ότι εμπλέκεται σε μνημονικές διαδικασίες, όπως ο διαχωρισμός και η ολοκλήρωση προτύπων, καθώς και χωρική κωδικοποίηση. Συγκεκριμένα, διαφορετικές περιοχές του ιππόκαμπου παίζουν ρόλο στις προαναφερθείσες λειτουργίες. Ειδικότερα, η οδοντωτή έλικα έχει έναν πολύ σημαντικό ρόλο στη διάκριση παρεμφερών εξωτερικών ερεθισμάτων, ενώ η περιοχή CA1 βοηθάει στη χωρική πλοήγηση και στο σχηματισμό του χωροταξικού χάρτη του εγκεφάλου. Αξιοποιώντας την ισχύ που μας παρέχει η χρήση υπολογιστικών μοντέλων, υλοποιήσαμε δύο διαφορετικά δίκτυα προκειμένου να αποκαλύψουμε και να μελετήσουμε σε βάθος τους μηχανισμούς που αποτελούν τις βασικές μεταβλητές κατά τη διάρκεια αυτών των λειτουργιών. Τα αποτελέσματά μας υποδεικνύουν ότι η αραιή ενεργοποίηση των κύριων κυττάρων της οδοντωτής έλικας αποτελεί βασικό χαρακτηριστικό και δείξαμε ότι διάφοροι μηχανισμοί θα μπορούσαν να το επηρεάσουν αυξομειώνοντας το, όπως ο αριθμός των δενδριτών, το μήκος των δενδριτικών διαδρομών καθώς και άλλα δευτερεύοντα κύτταρα που βρίσκονται στην ίδια περιοχή του ιππόκαμπου. Επιπλέον, διερευνήσαμε το ρόλο του κάθε διαφορετικού τύπου ενδονευρώνα κατά τη χωρική πλοήγηση ενός ζώου σε μία ευθύγραμμη πίστα. Τα αποτελέσματά μας δείχνουν ότι κάθε είδος ενδονευρώνα διαδραματίζει έναν ξεχωριστό ρόλο κατά τη διάρκεια του σχηματισμού κυττάρων που ενεργοποιούνται σε συγκεκριμένα σημεία στο χώρο. Ειδικότερα, οι ανασταλτικοί νευρώνες που εκφράζουν είτε την PV^+ είτε τις VIP^+/CCK^+ διαδραματίζουν έναν πολύ σημαντικό ρόλο στην προαναφερθείσα διαδικασία. Τα υπολογιστικά μοντέλα μας έχουν οδηγήσει σε μια σειρά από προβλέψεις, οι οποίες αν επιβεβαιωθούν και πειραματικά θα μπορούσαν δυνητικά να οδηγήσουν στην καλύτερη κατανόηση της φυσιολογικής αλλά και της παθολογικής λειτουργίας του ιππόκαμπου.

Abbreviations

AAC: axo-axonic cells

AMPA: α-amino-3-hydroxy-5-methyl-4-isoxazolepropionic acid

BC: basket cell

BSC: bistratified cells

CA: cornu ammonis areas

CCK: cholecystokinin

CR: calretinin

DG: dentate gyrus

EC: entorhinal cortex

GABA: γ-aminobutyric acid

GC: granule cell

HIPP: hilar perforant path-associated cells

NMDA: N-methyl-D-aspartate

OLM: oriens-lacunosum moleculare cells

PP: perforant path

PP: perforant pathway

PV: parvalbumin

SOM: somatostatin

VIP: vasoactive intestinal peptide

List of Figures

List of Tables

Table of Contents

Chapter 1 Introduction

1.1 Anatomy of the basic hippocampal subregions

The hippocampus, also referred to as archicortex, is a crucial component of the mammalian brain. Most mammals, including humans, have two hippocampi, one in each side of their brains. The hippocampus is located under the cerebral cortex, in the temporal lobe of mammals. It is a part of the limbic system and plays a significant role in memory formation, storage and consolidation (Squire et al., 2004), while it is also essential for spatial navigation (O'Keefe et al., 1998) and control of attention (Muzzio et al., 2009). The hippocampus consists of three subregions; the hippocampus proper (consisting of four Cornu Ammonis areas – CA4, CA3, CA2 and CA1), the dentate gyrus and the subiculum (Figure 1A). The hippocampus together with the presubuculum, parasubiculum and entorhinal cortex form a structure known as the hippocampal formation (Amaral and Lavenex, 2007). The cell types and basic connectivity properties of neurons within the hippocampal formation are similar across mammals.

The hippocampus receives its major input from cortical areas via the entorhinal cortex superficial layers. The first station of information is the Dentate Gyrus (DG). Subsequently, information flows into the CA3 area via strong connections called mossy fibers, and then passes to the CA1 area through the Schafer collaterals. Both directly from the CA1 and indirectly through the subiculum, processed information returns to the deeper layers of the Entorhinal Cortex (Figure 1B).

A

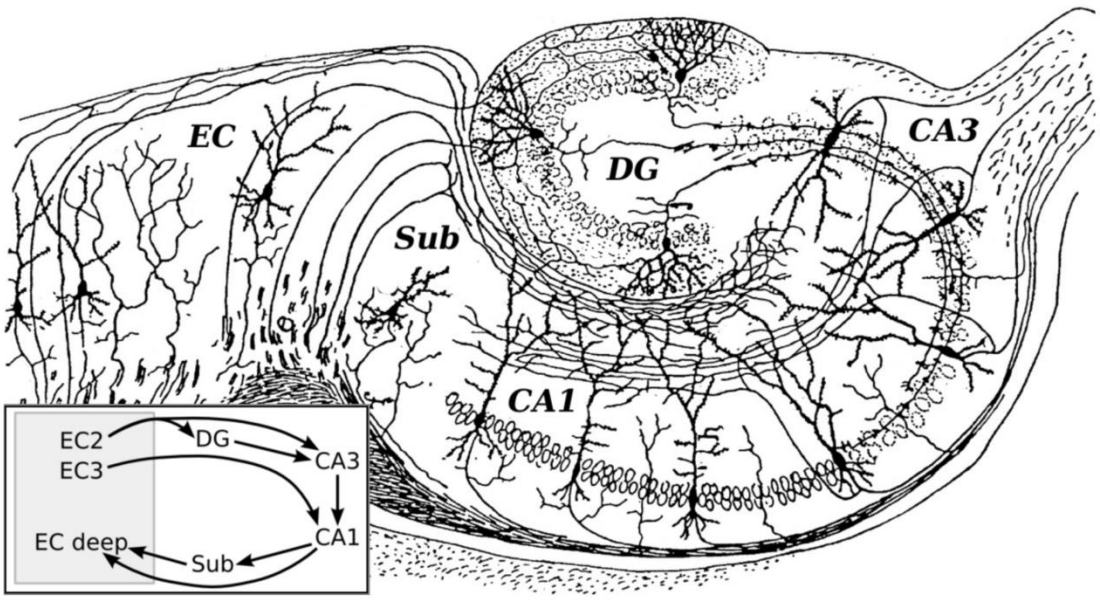

B

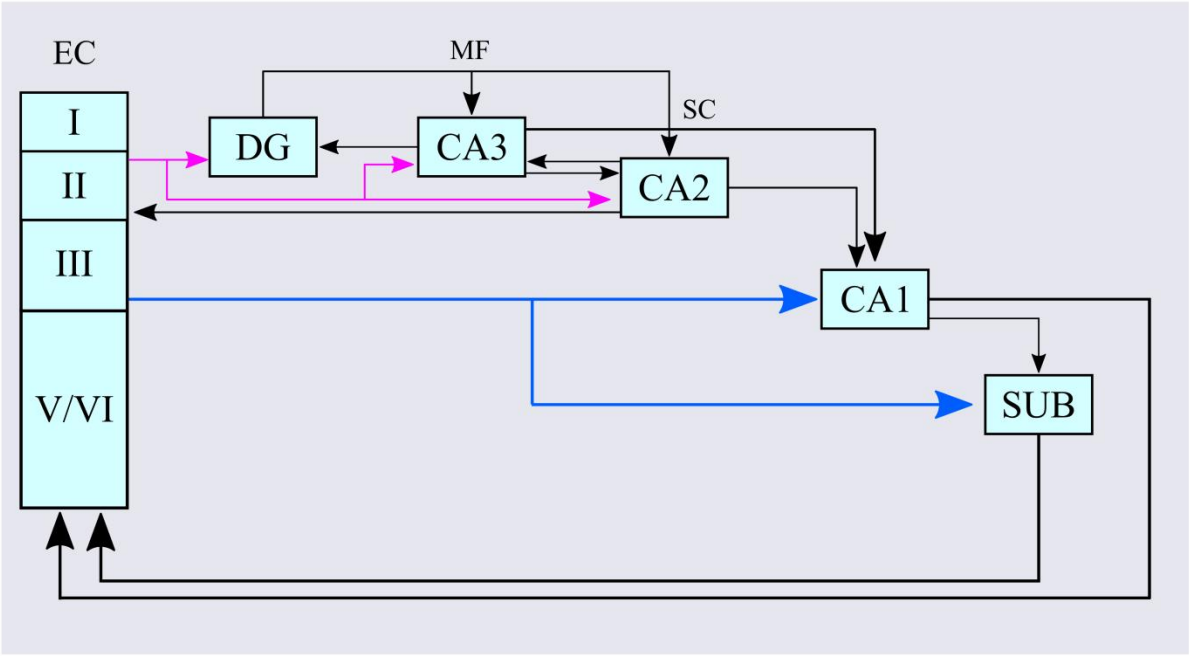

Figure 1. Hippocampal formation.

A. Basic circuit of the hippocampal formation as drawn by Santiago Ramón y Cajal. EC: entorhinal Cortex, DG: Dentate Gyrus, CA: Cornu Ammonis, Sub: Subiculum. At bottom left, a schematic diagram of the EC and the hippocampus is shown in which the famous trisynaptic loop is represented (EC → DG → CA3 → CA1). The image is adopted from

https://en.wikipedia.org/wiki/Hippocampus. B. Schematic diagram of the hippocampal network. MF: Mossy Fibers. SC: Schafer Collateral. The information enters the hippocampus via EC LII. From there it travels to DG, CA3 and the CA2 subregions. Latin numbers denote the different layers of the EC. Additionally, EC LIII sends afferents to CA1 and Subiculum directly. Information flows through hippocampus via the mossy fibers (DG to CA3) and the Schaffer collaterals (CA3 to CA1). The processed information returns to the deeper layers of the EC, via the CA1 direct connections and via the subiculum.

1.1.1 Dentate Gyrus

The DG is the first subregion of the hippocampus that receives incoming information from other brain areas, mainly via the EC LII. DG principal neurons, the Granule Cells (GCs), receive input from excitatory afferents coming from EC layer II cells and project to the CA3 subregion. In addition, they receive input from other DG excitatory cells, the Mossy Cells (MCs), and various types of interneurons (Sik et al., 1997) with Basket Cells (BCs) and Hilar Perforant Path associated (HIPP) cells being the most important. MCs form an inhibitory circuit as their axons contact the BCs. The net effect of MC excitation to both GCs and BCs is considered to be inhibitory (Jinde et al., 2012).

The DG is a three-layered structure. From the outside there is a relatively cell free layer called molecular layer, followed by the granule cell layer, which is densely packed with granule cells, followed by the polymorphic cell layer or hilus. Hilus is also referred to as the CA4 hippocampal subregion (Amaral, 1978). Dentate principal neurons, GCs, are small cells with elliptical somata that send their dendritic tree into the molecular layer. Under healthy conditions they do not have basal dendrites. GCs are one of the few cell types in the central nervous system that undergo adult neurogenesis, thus new neurons are continuously formed throughout adulthood. Both the molecular layer (albeit sparsely) and the polymorphic layer are occupied by multiple classes of (poorly characterized) neuron types. Underneath the granule cell layer a large number of different types of cells are laid, usually called hilar cells. The majority of cells in the hilus are GABAergic interneurons which provide inhibition to the network.

Excitatory MCs are also lying in the hilus, contacting GCs and BCs via excitatory glutamatergic synapses. Generally, the GCs are not recurrently connected.

Input from the EC LII arrives - through the perforant pathway- on the dendrites of the granule cells in the molecular layer (distal dendrites). The DG, in turn, projects to CA3 and CA2 via strong axons called mossy fibers originating from GCs (Kohara et al., 2013). Mossy fibers form unique connections with the dendrites of CA3/CA2 pyramidal neurons. There are no neurons that run in the reverse direction; therefore there are no bilateral connections between these two regions (dentate gyrus to entorhinal cortex).

There is also evidence that the DG receives smaller input from the presubiculum and parasubiculum areas (Köhler, 1985), but their specific dentate targets are highly elusive. Interestingly, the presubiculum is a region that receives all of its direct input from the thalamus, and hence provides a potential pathway through which thalamic information can reach the DG.

The DG receives very few inputs from subcortical structures which mainly arise from the septal nuclei (Swanson, 1977; Amaral and Kurz, 1985). These nuclei project profoundly to the hilus and their vast majority is cholinergic, whereas other septal neurons are inhibitory. The excitatory and inhibitory septal cells target different cell types preferentially, GABAergic afferents to GABAergic neurons lying in the polymorphic layer, while cholinergic fibers to GCs onto the inner third of the molecular layer of the DG, and a small population target MCs in the hilus (Amaral and Kurz, 1985; Lübke et al., 1997). Finally, DG receives input from hypothalamus, brainstem, ventral tegmental area, and raphe nuclei (Amaral et al., 2007).

1.1.2 The CA3 subregion

The second station of processed information in the hippocampus proper is the CA3 subregion. In contrast to DG, the CA3 is a five layer region. The somata of the principal cells of the CA3, namely the pyramidal neurons, lay in the Stratum Pyramidale (SP) layer. Their basal dendrites are located deeper, in the Stratum

Oriens (SO) layer. Many of the CA3-to-CA3 associational connections are in this layer and also few connections from DG via MFs. Just above the SP, Stratum Lucidum (SL) is one of the thinnest layers in hippocampus, hosting axons from DG neurons that terminate onto SP neurons. The next layer is the Stratum Radiatum (SR) in which most of the recurrent connections among pyramidal cells are formed. Finally, the last layer most superficial from SP is the Stratum Lacunosum-Moleculare (SLM). In this layer perforant path (EC LII) axons onto the distal apical dendrites of pyramidal neurons are found.

The vast majority of cells in the CA3 are pyramidal neurons, however there are also a large variety of interneurons (Freund and Buzsáki, 1996). Among others, Basket Cells provide the network with somatic inhibition, while OLM, RLM and Bistratified cells make contacts on the dendritic tree of pyramidal cells. Interneurons in CA3 can be found in all layers.

The CA3 area is also divided in three subregions: the CA3c, the CA3b and the CA3a. Input to the CA3 comes primarily from the DG via strong axons called mossy fibers, which form giant synapses onto proximal apical and basal dendrites of CA3 pyramidal neurons. DG also excites CA3 interneurons, creating a form of feed-forward inhibition. Interneurons also receive excitatory input from EC LII via the perforant path onto their distal apical dendrites. CA3 also exhibits strong recurrency among pyramidal neurons, which form synapses onto dendrites located in the SR and SO (Witter, 2007). CA3 pyramidal neurons also connect with DG mostly in the polymorphic layer, and thus excite both interneurons and MCs. In addition, they connect with the CA1 region via the Schaffer collateral pathway and with contralateral CA1 via a commissural pathway (Ishizuka et al., 1990).

Apart from these excitatory inputs from EC LII, DG and CA3 principal cells also receive input from other cortical areas. In contrast to DG, these inputs are rather limited. The main nonhippocampal connection of CA3 is with the septum, in that CA3 receives input from the medial septum/diagonal band complex and projects preferentially to the lateral septal nuclei (Witter, 2007). Other inputs to CA3 originate from the amygdaloid complex and endopiriform nucleus and some of the aminergic nuclei (Witter and Amaral, 2004). Notably, the CA3 region, similar to the DG, does not receive thalamic input (Vertes et al., 2006).

1.1.3 The CA1 subregion

The CA1 subregion is the last station of information flow through hippocampal proper. It is a four layer structure, in which the somata of pyramidal cells (CA1PCs) are tightly packed in the pyramidal cell layer or Stratum Pyramidale (SP). The narrow, relatively cell-free layer located deeper to the SP layer is the Stratum Oriens (SO). This layer contains the basal dendrites of pyramidal cells and several classes of interneurons. SO can be defined as the infrapyramidal region in which some of the Schaffer collateral connections are located. The Stratum Radiatum (SR) is found immediately above the SP and can be defined as the suprapyramidal region in which the majority of the CA3 input is located. The most superficial layer of the CA1 region is called Stratum Lacunosum-Moleculare (SLM) layer. In SLM the afferents from EC LIII terminate. Afferents from other regions, such as the nucleus reuniens of the midline thalamus, also terminate in the SLM. In both the SR and the SLM a variety of interneurons are present.

The most important interneurons that have been extensively studied are divided in three basic categories, according to the location of their postsynaptic targets (Freund and Buzsáki, 1996; Klausberger and Somogyi, 2008). The first category contains the interneurons that provide CA1PCs with perisomatic or axonal inhibition. The majority of these cells are Basket Cells (BCs), which contact pyramidal somata, and are either PV^+ or CCK^+ basket cells. Axoaxonic cells (AACs) contact CA1PCs at the axon. The second category consists of interneurons that synapse onto the dendrites of CA1PCs. Two main neuronal types are involved in dendritic inhibition; the Bistartified Cells (BSCs, PV^+ interneurons) and the Oriens Lacunosum-Moleculare cells (OLMs, SOM^+ interneurons), making synapses onto the proximal (SR) and distal (SLM) apical dendrites of pyramidal cells, respectively. The third category contains interneurons that mainly contact other interneurons providing the network with disinhibition. The majority of these cells are VIP^+ cells, which mainly inhibit BCs and OLMs (Chamberland and Topolnik, 2012; Tyan et al., 2014; Francavilla et al., 2015).

The CA1 area receives major input connections from several extrinsic sources (Takács et al., 2012). The major cortical input to CA1 comes from afferents originating in EC LIII and terminating onto the distal dendrites of CA1PCs, located in SLM, through the temporo-ammonic pathway (Steward and Scoville, 1976), as well as to several interneurons (Desmond et al., 1994). Likewise, CA3 provides CA1 with excitatory inputs via Schaffer collaterals which synapse onto proximal and basal dendrites of CA1PCs, located in SR and SO, respectively (Amaral and Witter, 1989). The predominant input to CA1 is coming through afferents from CA3 pyramidal cells also terminate onto several interneurons (Wittner et al., 2006). In addition to the excitation arriving from extrinsic sources, CA1PCs have sparse local collaterals which were shown to innervate both pyramidal cells (Deuchars and Thomson, 1996) and interneurons (Buhl et al., 1994).

Other glutamatergic inputs to the CA1 come from the thalamus (Dolleman-Van der Weel and Witter, 2000; Bokor et al., 2002), the amygdala (Pitkänen et al., 2000; Ghosh et al., 2013) and the perirhinal cortex (Naber et al., 1999; Burwell, 2006). There is a dual serotonergic and glutamatergic projection from the median raphe nucleus (Varga et al., 2009) while glutamatergic inputs also originate from the medial septum (Huh et al., 2010). The medial septum also connects to CA1 via GABAergic synapses onto interneuronal populations (Dragoi et al., 1999) and these connections are important for hippocampal network oscillations.

1.2 Anatomy of the Entorhinal Cortex

The entorhinal cortex (EC), together with the perirhinal cortex, the parahippocampal cortex and the hippocampus, form the medial temporal lobe in the mammalian brain. Specifically, EC constitutes the major node of cortico-hippocampal circuits. Thus, it is a crucial structure for memory formation due to its forceful reciprocal connections with the hippocampus. In mammals, the medial temporal lobe is organized in parallel circuits; an anterior circuitry connects perirhinal cortex to lateral EC, whereas a posterior links parahipocampal cortex with medial EC.

In the EC, like other cortical areas, neurons are grouped into distinct layers that are characterized by a principal cell type. In order to match the neocortex notation, six layers are defined of which layers I and IV contain no neurons. The main recipients of incoming information and the major source of EC output to a variety of cortical and subcortical structures are pyramidal cells or stellate cells (in LEC these are often referred to as fan cells; Canto et al., 2008; Moser et al., 2010).

Cortical inputs to the EC mainly target neurons in layers II and III and come from both cortical (Burwell and Amaral, 1998; Agster and Burwell, 2009) and subcortical regions (Tomás Pereira et al., 2016). The lateral and mEC are innervated primarily by perirhinal, insular, piriform, and postrhinal cortices, while the medial EC receives cortical input predominantly from piriform and postrhinal cortices. The EC connects to the hippocampal subregions via the perforant and temporo-ammonic pathways, projecting to all hippocampal subregions, providing them with their major cortical input (see §1.1). Layer II neurons mainly project to the DG and CA3 subregions, while cells in layer III innervate largely the CA1 and the subiculum hippocampal areas. Subcortical inputs, such as cholinergic and monoaminergic inputs from the septum and brainstem as well as afferents from the thalamus, amygdala, and claustrum exhibit an overall diffuse terminal distribution in the EC (Tomás Pereira et al., 2016). Output of the hippocampal formation preferentially targets deeper layers of the EC (i.e., V and VI), which in turn are the origin of widespread reciprocal cortical projections to numerous cortical regions (Agster and Burwell, 2009) and subcortical projections mostly to the amygdala, septum, striatum, and thalamus (Agster et al., 2016). Although this apparent separation between input and output layers provides a simple functional concept, it has recently been challenged by a number of findings indicating that reciprocal interactions between deep and superficial layers are quite substantial, and that major cortical inputs also target the apical dendrites of the neurons located in deeper layers (Canto et al., 2008).

1.3 Morphology of hippocampal principal neurons (GCs, CA1PCs)

1.3.1 Granule Cells of the Dentate Gyrus

GCs are characterized by a strictly bipolar morphology with spiny dendrites originating from the upper pole of the soma and an emerging axon from the base (Claiborne et al., 1990; Schmidt-Hieber et al., 2004). The small, round cell somata have a diameter of approximately 10 μm and are located densely packed in the GC layer. One to four primary dendrites arise from the soma and bifurcate three to six times to form a dendritic tuft in the molecular layer. Terminal branches extend mostly to the hippocampal fissure and the tuft occupies a conical-shaped volume within the molecular layer with a wider transverse and a narrower septo-temporal extent. Dendrites show a gradual reduction in size with diameters, varying from almost 1.5 μm in proximal dendrites to 0.7 μm in distal dendrites (Schmidt-Hieber et al., 2007). The total dendritic length ranges between 2,300 and 4,600 μm, substantially shorter than the respective length in pyramidal cells (Claiborne et al., 1990). While morphological features of these neurons are largely homogeneous, quantitative differences exist between the upper and the lower blades, as well as between superficial (near the molecular layer) and deep cells near the hilus (Claiborne et al., 1990). Superficial neurons in the upper blade have the largest total dendritic length and the widest arbor, whereas deep neurons in the lower blade have the smallest length and the narrowest transverse extent. GC dendrites are densely covered with spines with a total number varying between 3,000 and 7,000 on the basis of a light microscope estimate of spine density of about $2.39 \pm 0.06\ \mu m^{-1}$. Electron microscopic analysis acquired similar density values and pointed out adequate differences between proximal, medial, and distal dendritic parts, with 3.36, 2.88 and 2.02 μm^{-1}, respectively (Hama et al., 1989). The differences in density are largely explained by the decreasing diameter and surface area of proximal to distal dendrites. In fact, the surface density of spines is comparable in the dendritic compartments with values ranging from 0.79 to 0.88 μm^{-2} (Hama et al., 1989). Spine surface contributes by a factor of 0.91–1.05 to the total surface area of the neurons (Hama et al., 1989; Schmidt-Hieber et al., 2007). There are only limited quantitative data

on the synaptic inputs to GCs. The number of excitatory synapses can be estimated on the basis of spine densities. The three main afferent systems, the commissural/associational path, the medial and the lateral perforant path, terminate in a strictly laminated fashion in the inner, middle, and outer molecular layer, respectively. The proportions of the dendrites falling into these layers are approximately 35%, with largest values in distal dendrites (Claiborne et al., 1990; Schmidt-Hieber et al., 2007). The corresponding spine numbers on the surface of GC with a dendritic length of 3,200 μm vary from 3,000 to 2,500 in proximal to distal dendrites, respectively (Vida, 2010). Therefore, the number of excitatory synapses onto a single GC could be as high as 8,500 contacts.

The distribution of inhibitory terminals was analyzed in a combined immunocytochemical and electron microscopy study (Halasy and Somogyi, 1993). Results indicate that in the molecular layer ~7.5% of the synapses are GABAergic and these synapses account for 75% of all inhibitory synapses, with the remaining 25% located in the granular layer. Hence, the number of inhibitory synapses onto a single GC can be estimated around 900, with roughly 650 in the molecular layer and the remaining in the granular layer. The compartmental distribution of the inhibitory input is broken down to almost 70% dendritic shafts and 30% spines in the molecular layer. In the cell body layer the majority, approximately 50%, are on GC somata, 25% on proximal dendrites, 15% on spines, and 10% on axon initial segments (Halasy and Somogyi, 1993).

The axons of GCs, the mossy fibers (MF), provide the major output of the DG to the CA3 and CA2 subregions. The unique features of mossy fibers are the 10–18 sparsely spaced large varicosities, the so-called mossy fiber boutons, which form synapses onto complex spines of CA3 pyramidal cells in the SL and with MCs in the hilus (Hartmann et al., 1994). Furthermore, MFs innervate a large number of inhibitory interneurons in both regions either through small, en passant boutons and or via axonal extensions emerging from the large MF boutons mentioned above (Acsády et al., 1998).

1.3.2 Pyramidal Cells of the CA1

Pyramidal cells of the CA1 are probably the most extensively characterized neurons in the brain. These neurons are characterized by a pyramidal (ovoid) soma, a large-caliber apical dendrite extends to SR and SLM, and a number of small-caliber basal dendrites extend to SO. The cell bodies have a diameter of about 15 μm and a total surface area of almost 465 μm^2 (Megías et al., 2001). Each CA1PC consist of typically one apical dendrite (sometimes two) which extends into the SR giving off nine to thirty oblique side branches in this layer (Bannister and Larkman, 1995a). They terminate with a bifurcation in the SR and form a dendritic tuft in the SLM. Two to eight basal dendrites emerge from the base of the cell body in the SO and bifurcate repeatedly close to the soma, while their long terminal branches expand toward the alveus.

The total dendritic length of CA1PCs is in the range of 11.5 to 17.5 mm (Vida, 2010). Corresponding estimates of the total surface area are 28,860 and 36,000 μm^2, without taking into account dendritic spines (Bannister and Larkman, 1995b). As dendrites of CA1PCs are densely covered with spines, whose number is over 30,000 (Bannister and Larkman, 1995b; Megías et al., 2001), the actual surface area is much larger. Specifically, spines increase the dendritic surface area by a factor of 0.89. Importantly, the distribution of spines is not homogeneous on the dendritic tree. Density is higher within the SO and SR layers and lower in the SLM (Bannister and Larkman, 1995b).

Spines of CA1PCs are postsynaptic targets predominantly for glutamatergic terminals, and therefore their high numbers is a reflection of the massive excitatory synaptic input that these cells receive. In fact, an average of 30,600 terminals are connected with a single CA1PC forming asymmetrical, putative excitatory synapses. More than 99% of these synapses are located on dendritic spines, apart from the SLM where up to 17% of the synapses are located on dendritic shafts. On the contrary, somata of CA1PCs do not generally have excitatory synapses. The number of symmetrical putative inhibitory synapses formed by GABAergic synapses is much lower. A single neuron receives about 1,700 symmetrical synapses, which account for only 5.6% of the total synapses (Megías et al., 2001). In contrast

to excitatory synapses, a significant number of inhibitory synapses are located in the perisomatic domain. Only a small proportion can be found on the soma and the initial axonal segment, while the majority is located at proximal dendrites. In these compartments, inhibitory synapses comprise 50-100% of all synapses. In contrast, on dendrites in the SR and SO, the proportion of these synapses is only 4-5%. Interestingly, on distal apical dendrites in the SLM the proportion increases again to 16%. On the dendrites, almost all inhibitory terminals form contacts with dendritic shafts. However, as an exception to this rule, in the SLM 10-20% of the inhibitory synapses have been found on spines (Megías et al., 2001).

The axon of pyramidal cells typically originates from the base of the soma, but it may also emerge from one of the proximal basal or apical dendrites. The main collaterals run in the alveus and are directed toward the fimbria/fornix, the subiculum, and the deeper layers of the EC. Although the extent of local arborization is limited, axon collaterals are present in the SO and to a lower degree in the SR. These axons provide a major excitatory input to interneurons providing the principal cells with feedback inhibition. Additionally, these collaterals also form synapses onto neighboring CA1 pyramidal cells; however, the recurrent connectivity in the CA1 area is very low, ~1% (Deuchars and Thomson, 1996).

1.4 Memory functions of the hippocampus

The hippocampus is known to be involved in memory formation, storage and consolidation (Squire et al., 2004), yet its specific functionalities remain a mystery. A traditional view entails that the hippocampus forms a unitary memory storage system – along with other Medial Temporal Lobe (MTL) structures (Squire and Zola-Morgan, 1991; Squire and Wixted, 2011). Another widespread interpretation is that the hippocampus mediates recollective memory rather than familiarity-based recognition (Eldridge et al., 2000; Diana et al., 2007; Shimamura, 2010; Yonelinas et al., 2010). Other studies suggest that MTL activity is not exclusive to memory, but is also involved in perceptual processing of complex scenes (Eacott et al., 1994; Buckley et al., 2001; Lee et al., 2005; Lech and Suchan, 2013). The aforementioned views show the many different functions that have been ascribed to the MTL. The main goal of this thesis

is to investigate two of these functions, namely the ability to discriminate similar inputs (pattern separation) and the ability to navigate through space via the formation of place cells.

1.4.1 Pattern separation

Two key functionalities of the hippocampus concern the ability to rapidly store non-overlapping representations of similar inputs and thereafter, retrieve them given a partial or noisy stimulus. Theoretical models refer to these processes as pattern separation and pattern completion, respectively (Marr, 1971; Treves and Rolls, 1994; Yassa and Stark, 2011; Santoro, 2013). The Dentate Gyrus (DG), in particular, has been proposed to implement pattern separation by sparsifying and orthogonalizing its input, coming mainly from the Entorhinal Cortex (EC), and thereafter, projecting this information to the CA3 area via the mossy fibers (Treves and Rolls, 1994), whereas the CA3 subregion is responsible for retrieving an already stored memory given partial or noisy stimuli.

DG has been hypothesized to separate two distinct but overlapping patterns through the activation of different Granule Cells (GCs), through the expression of different firing rates in identical neuronal populations (Deng et al., 2010) or a combination of the two. While several studies have investigated pattern separation both in rodents (Leutgeb et al., 2004, 2005, 2007) and humans (Kirwan and Stark, 2007; Bakker et al., 2008; Lacy et al., 2011; Motley and Kirwan, 2012), the role of dendrites in this phenomenon remains unknown.

Experimental studies have shown that only a small population of GCs, ~5%, are active in a single context (Marrone et al., 2011; Satvat et al., 2011; Danielson et al., 2016a), a phenomenon termed sparse coding (Olshausen and Field, 2004). It has been proposed that sparse coding in GCs enhances pattern separation by recruiting different subgroups of GCs to encode similar incoming stimuli (Treves et al., 2008; Petrantonakis and Poirazi, 2014, 2015). Computational models (Santhakumar et al., 2005; Yim et al., 2015) and experimental studies (Nitz and McNaughton, 2004; Jinde et al., 2012) have proposed that

inhibition controls GC activity which, in turn, mediates pattern separation (Myers and Scharfman, 2009, 2011; Ikrar et al., 2013; Faghihi and Moustafa, 2015).

The ability to perform pattern separation is critical for normal brain functioning and its impairment is associated with cognitive decline. Diseases such as schizophrenia (Das et al., 2014) and Alzheimer's Disease (AD) (Ally et al., 2013), where cognitive decline is evident, are both characterized by pattern separation deficiencies. Interestingly, these conditions are also characterized by alterations in the anatomical properties of GC dendrites, such as a decrease in the total dendritic length (Einstein et al., 1994) and spine loss (Jain et al., 2012). Dendritic growth on the other hand has been associated with pattern separation enhancements. Specifically, voluntary running was recently shown to enhance pattern separation and this enhancement was attributed to an increase in the neurogenesis rate that was accompanied by increased GC dendrite outgrowth in active compared to sedentary animals (Bolz et al., 2015). These findings suggest that the dendrites of GCs are likely to play a key role in pattern separation mediated by the DG.

1.4.2 Spatial navigation

Another functionality of hippocampus is its involvement in spatial navigation (O'Keefe and Nadel, 1978) both in humans (Burgess et al., 2002) and in animals (Clark et al., 2005a; Vorhees and Williams, 2014). Increased hippocampal volume relative to brain and body size has been documented in small mammals and birds involving in behavioral tasks requiring spatial memory, such as food storing and retrieval (Lee et al., 1998). In some species, hippocampal volumes enlarge specifically during periods when demand for high spatial capacity is increased (Smulders et al., 1995; Lee et al., 1998). In healthy humans, structural brain dissimilarities between different groups of subjects have been reported, such as between males and females (Gur et al., 1999) and between musicians and non-musicians (Schlaug et al., 1995). However, the aforementioned studies could not verify whether the reported differences in brain anatomy are predetermined or are existed due to plastic nature of the brain in response to enriched environmental

stimulation (van Praag et al., 2000). Besides, even though lesion works (Maguire et al., 1996; Clark et al., 2005b, 2007) and functional neuroimaging studies (Maguire et al., 1999; Lee et al., 2013; Zeidman and Maguire, 2016) confirm the involvement of the mammalian hippocampus in spatial memory and navigation, its precise role remains mysterious.

"*The process of determining and maintaining a course or trajectory from one place to another*" (Gallistel, 1990) is an accurate definition of navigation. The experimental examination of how spatial representations are encoded in the brain began with the discovery of place cells (O'Keefe and Dostrovsky, 1971). O'Keefe and Dostrovsky reported spatial receptive fields in complex-spiking neurons in the rat hippocampus. These place cells fired whenever the rat passes from a certain place in the local environment, which is called place field of the cell. Place cells were suggested to provide the animal with a dynamic, continuously updated representation of allocentric space and the position of the animal in that space. Nowadays, there is lavish evidence from a number of mammalian species indicating that the hippocampus plays a key role in navigation and spatial memory (Nadel, 1991; Ekstrom et al., 2003; Ulanovsky and Moss, 2007), although new evidence suggests that position is only one of several facets of experience stored in the hippocampal network (Leutgeb et al., 2005; Eichenbaum, 2017).

All subfields of the hippocampal region contain place-modulated neurons, but the most distinct firing fields are found in the hippocampal proper, mainly in CA3 and CA1 regions (Park et al., 2011). On the basis of the apparent amplification of spatial signals from the EC LII to the CA fields (Quirk et al., 1992), many investigators thought, until recently, that place signals depended primarily on inter-hippocampal computations. This view was challenged by the observation that spatially-tuned firing persisted in CA1 neurons after lesion of inputs from the DG (McNaughton et al., 1989) and CA3 (Brun et al., 2002). This raised the possibility that spatial signals were conveyed to CA1 by the direct projections from EC LIII. Projection neurons in layers II and III of the medial EC were then shown to exhibit sharply tuned spatial firing profiles, commonly to place cells in the hippocampus, except that each cell had multiple firing fields (Fyhn et al., 2004). These fields formed a periodic triangular array, or grid, that covered the entire

environment explored by the animal (Hafting et al., 2005). Each grid is characterized the spacing, i.e., distance between the fields, the orientation, i.e., tilt relative to an external reference axis, and phase, i.e., displacement relative to an external reference point. Even though cells in the same part of the medial EC have similar spacing and orientation, the phase of the grid is nontopographic, thus the firing vertices of co-localized grid cells appear to be shifted randomly, just like the fields of neighboring place cells in the hippocampus. Taken all together, there is a spatial map in the brain which is responsible for the accurate navigation through complex spaces. The information is transformed in grid cells, which subsequently pass it to hippocampus and transform the place cells. However, if this map is a cognitive (Eichenbaum, 2015) or predictive (Stachenfeld et al., 2017) is a matter of debate.

Chapter 2 Motivation

Driven by the vast, yet fragmented, studies on hippocampal role in memory formation, consolidation and retrieval, this dissertation aims to shed light on specific mechanisms that are crucial for distinct mnemonic processes. Specifically, the main target is the investigation and exploration of dendritic role in pattern separation task, as well as the inhibitory effect on spatial navigational skills. The methodological approach includes the development and application of large scale neural networks consisting of spiking neuronal models and biophysically detailed microcircuits of dentate gyrus and CA1 hippocampal subregions, respectively. These areas are selected as there is a numerous research implicating dentate gyrus with pattern separation ability and CA1 with spatial navigation.

The following open questions are tangled in this study:

1. *What is the role of granule cell dendrites in pattern separation?*
2. *Are dendrites sufficient and necessary for dentate gyrus to be a key mediator of pattern separation?*
3. *Are other mechanisms that affect pattern separation efficacy through mediating sparsity?*
4. *What is the role of mossy cells in pattern separation?*
5. *What is the role of interneurons in place cell formation?*

Overall this thesis seeks to establish a link between dendritic morphology and pattern separation efficacy inspired observed alterations of granule cell dendrites during neurodegenerative diseases. In addition, the secondary aim of this project is to reveal the mechanisms underlie spatial navigation ability which is another mnemonic process that is crucial for everyday life. We focus here on the role of the different interneurons found in CA1 area and their impact on place cell formation and dynamics.

Chapter 3 Methodology

3.1 The DG network model

The model was developed mainly based on the structure and connectivity features described by Myers and Scharfman (2009), and incorporates the four major dentate cell types. These are the GCs, MCs, BCs and HIPP cells. As the Hilar Commissural-Associational Pathway (HICAP) cells are relatively rare and poorly understood (Sik et al., 1997), they are not included in the model. All simulations were performed using the BRIAN (BRIAN v1.4) network simulator (Goodman and Brette, 2009; Brette and Goodman, 2011) running on a High-Performance Computing Cluster (HPCC) with 312 cores under 64-bit CentOS Linux.

3.1.1 Model neurons

The four types of DG neurons were modeled as simplified phenomenological neurons of the integrate-and-fire (I&F) type (Izhikevich, 2003; Burkitt, 2006), with no internal geometry ("point neurons"). The GCs incorporated dendrites in order to study their role in pattern separation; however the MCs, BCs and HIPP cells were simulated as simple somatic compartments.

3.1.1.1 Modeling BC, MC and HIPP cells

Specifically, an adaptive exponential I&F model (aEIF) (Brette and Gerstner, 2005) was used to model MCs, BCs and HIPP cells. The model is mathematically described by the following differential equations (Equation 1, 2):

$$C_m \frac{dV_m}{dt} = -g_L \cdot (V_m - E_L) + g_L \cdot \Delta_T \cdot e^{\left(\frac{V_m - V_T}{\Delta_T}\right)} + \sum I_{syn} - w$$

$$\tau_w \frac{dw}{dt} = \alpha \cdot (V_m - E_L) - w$$

where C_m is the membrane capacitance, V_m the membrane voltage, g_L the "leak" conductance, E_L the "leak" reversal potential (i.e., the resting potential), I_{syn} the synaptic current flow onto the neuron, w the adaptation variable, Δ_T the slope factor, V_T the effective threshold potential, α the adaptive coupling parameter, and τ_w is the adaptation time constant.

The exponential nonlinearity describes the spike action potential and its upswing. In the mathematical interpretation of the model a spike occurs at time t_{spike} when the membrane voltage reaches a finite limit value, and thereafter the downswing of the action potential is described by a reset fixed value V_{reset}, as follows:

$$at\ t = t_{spike}\ (V_m \geq V_{threshold})$$

$$reset\ V \leftarrow V_{reset}\ and\ w \leftarrow w + b$$

where $V_{threshold}$ is the voltage threshold above which the neuron fires a spike, and b is the spike triggered adaptation parameter. For all neuron types the effective threshold is equal to the voltage threshold (see Table 1 for model parameters).

3.1.1.2 Modeling principal neurons, GC

In order to investigate the role of GC dendrites in pattern separation, an extended point neuron was implemented. The GC model consisted of a leaky Integrate-and-Fire somatic compartment connected to a variable number of dendritic compartments whose morphology relies on anatomical data (see Table 2 for structure characteristics). Furthermore, an adaptation parameter w was used, only in the somatic compartment, to reproduce spike frequency adaptation reported in these neurons. The equation that describes the membrane, somatic and dendritic, potential of GC model cells is as follows:

$$C_m \frac{dV_m}{dt} = -g_L \cdot (V - E_L) + \sum I_{syn} - w$$

The adaptation parameter (w) was set to zero for the dendritic compartments. There is no evidence for dendritic spikes in GCs (Krueppel et al., 2011), thus the spike mechanism was only applied in the somatic equation.

The DG is divided into three distinct layers (Fig. 1A); the molecular, granular, and polymorphic (hilus) (Amaral et al., 2007). The GC dendrites extend in the molecular layer (Amaral et al., 2007), which is further divided into the inner, middle, and outer molecular layers, and therefore dendritic compartments are discretized accordingly. Table 2 lists the morphological characteristics of the GC model. According to anatomical data, (Claiborne et al., 1990) GCs have 10-15 dendrites; thus, the control GC model includes 12 dendrites and its physiological responses are validated against experimental data (see Table 1 for GC model parameters).

Table 1. Morphological properties of GCs

Structure of GC models	**Control**	**Pruning**		**Growth**	
	12 dendrites	**6 dendrites**	**3 dendrites**	**6 dendrites**	**3 dendrites**
# of compartments					
total	21	15	9	9	3
proximal	3	3	3	3	3
medial	6	6	3	6	-
distal	12	6	3	-	-
length per compartment (um)	83	83	83	83	83
total dendritic length (um)	1743	1245	747	747	249
diameter per compartment (um)					
proximal	1.0	1.0	1.0	1.0	1.0
medial	0.9	0.9	0.9	0.9	-
distal	0.8	0.8	0.8	-	-

In order to investigate whether the number of GC dendrites affects pattern separation, we used two different approaches; dendritic pruning and growth. First, two more GC models were implemented which differ only in their number of dendrites (6 and 3), but the path length remained the same across these models. Secondly, two GC models were implemented which differ both in their dendritic number and

their total path length. The morphological differences among the three models are shown in Table 2. The membrane capacitance of the dendritic compartments was increased compared to the somatic one in order to account for spines reported in GC dendrites (Aradi and Holmes, 1999).

3.1.2 Validation

The intrinsic model properties that were validated against experimental data are the input resistance (R_{in}), the sag ratio, defined as the ratio between the exponentially extrapolated voltage to the steady-state voltage, and the membrane time constant (τ_m). In line with experimental procedures (Lübke et al., 1998), we used 1-second somatic current injection to calculate the intrinsic properties. The input resistance is calculated by the equation $R_{in} = \Delta V_m / I_{injected}$, where ΔV_m is the membrane response to current stimulation. Finally, the membrane time-constant is approximated by the formula $\tau_m = R_{in} C_m$, which is a valid approximation for passive compartments (Table 2). As experimental data were obtained in the presence of synaptic activity blockers, a somatic current injection at the model cell was used to replicate those conditions.

Table 2. Model parameters for all neuronal types

Model Parameter	Granule cells		Mossy cells	Basket cells	HIPP cells
	Soma	dendrites			
E_L (mV) Resting potential	-87	-82	-64	-52	-59
g_L (nS) "Leak" conductance	0.00003[a]	0.00001[a]	4.53	18.054	1.930
C_m (nF) Membrane capacitance	1.0[b]	2.5[b]	0.621	0.1793	0.0584
V_{reset} (mV) Reset voltage	-74		-49	-45	-56
$V_T = V_{thr}$ (mV) Threshold voltage	-56		-42	-39	-50
Δ_T (mV) Slope factor	-		2	2	2
α (nS) Adaptation coupling parameter	2.0		2	0.1	0.82
τ_w (ms) Adaptation time constant	45		180	100	93
b (nS) Spike triggered adaptation	0.0450		0.0829	0.0205	0.015

[a]For the GC model the "leak" conductance is given in Siemens/cm^2
[b]For the GC model the membrane capacitance is given in μF/cm^2

Using the parameters listed above we validated each one neuronal model against experimental evidence. The passive properties of the neurons are shown in Table 3.

Table 3. Passive properties of neuronal models

Cell	R_{in} (MΩ)		τ_m (ms)		Sag ratio		f_{max} (Hz)	
	Model	Biological	Model	Biological	Model	Biological	Model	Biological
GCs	360	292 ± 34	41.2	31 ± 2	0.91	0.96 ± .1	60	70 ± 10
MCs	105	199 ± 19	33.7	35 ± 5	0.98	0.81 ± .3	45	50 ± 6
BCs	55	56 ± 9	9.67	10 ± 1	0.99	0.97 ± .02	247	230 ± 15
HIPPs	363	371 ± 47	21.4	15 ± 0	0.84	0.82 ± .04	113	101 ± 24
Sources	Lubke et al., 1998, Krueppel et al., 2009		Lubke et al., 1997, Ratzliff et al., 2004		Lubke et al., 1998, Bartos et al., 2001		Lubke et al., 1997	

Then we validated each individual neuronal model against experimental evidence using the current-voltage curve (Figure 2) as well as using the frequency as a function of current amplitude (Figure 3).

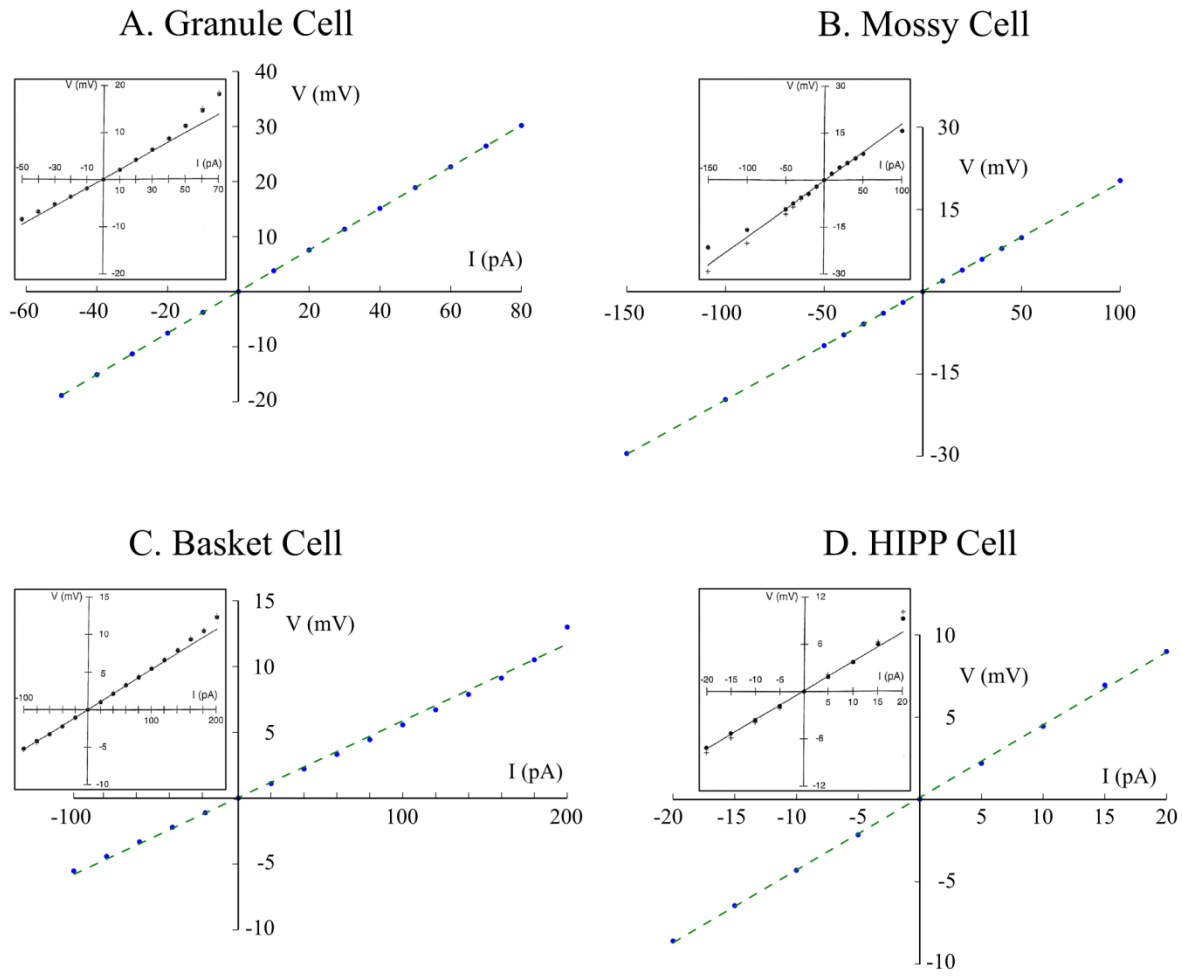

Figure 2. Current-Voltage (I-V) curves for the Granule cell, Mossy cell, Basket cell, and HIPP cell models.

Blue dots indicate the steady state points, while the dashed green line represents the linear regression through the steady state points. The current injection duration is 1 second. A. I-V curve for the granule cell. Voltage responses to current injections of -50 to +80 pA with 10-pA stepsize. B. I-V curve for the mossy cell. Voltage responses to current injections of -150 to +150 pA with 50-pA stepsize and -40 to 40 pA with 10 pA stepsize. C. I-V curve for the basket cell. Voltage responses to current injections of -100 to +200 pA with 20-pA stepsize. D. I-V curve for the HIPP cell. Voltage responses to current injections of -20 to +25 pA with 5-pA stepsize. Insets: The corresponding experiments adopted from (Lübke et al., 1998).

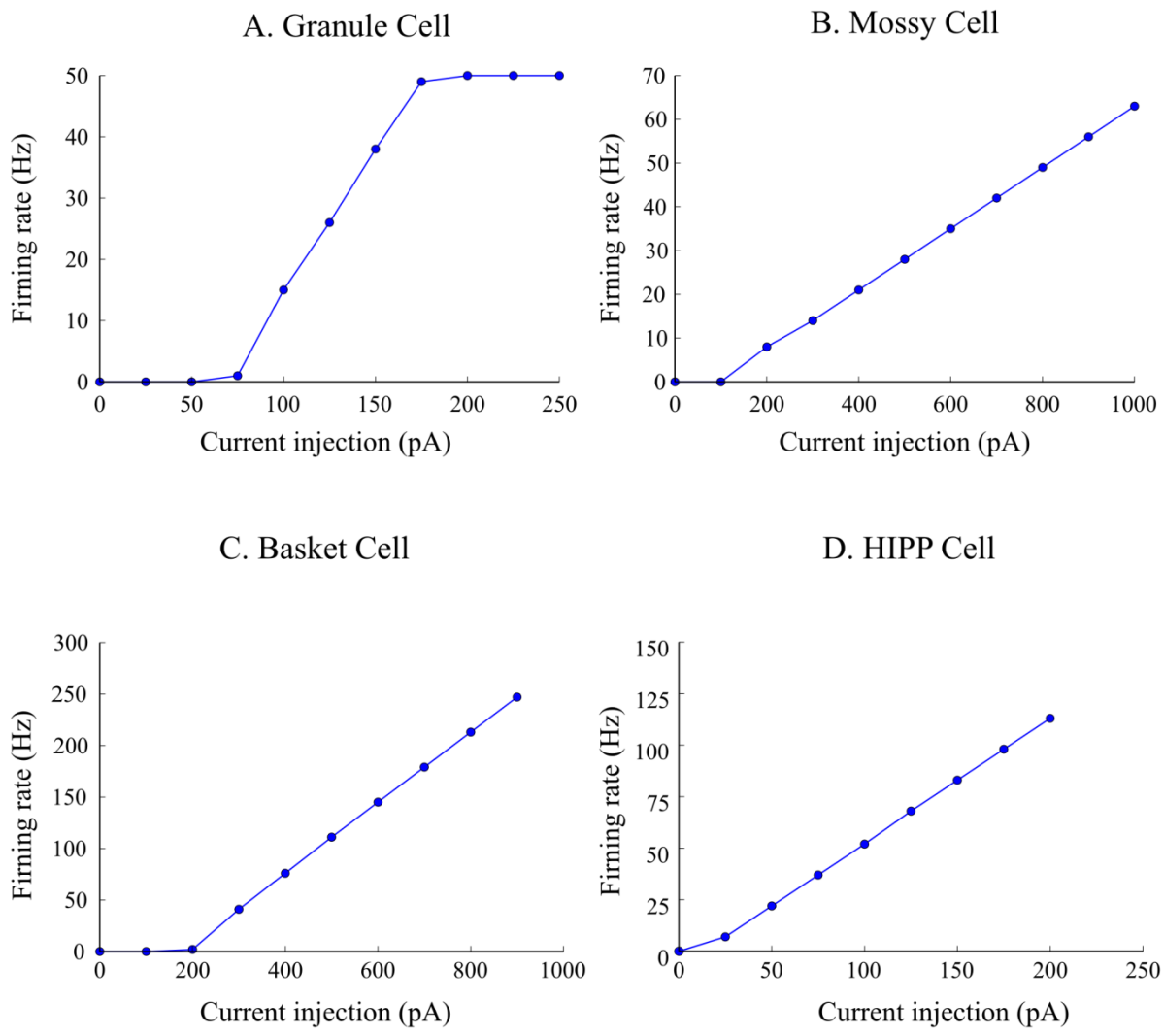

Figure 3. Current-frequency (I-f) relationship of Granule, Mossy, Basket and HIPP cells.

The y-axis represents the firing rate of each neuron in Hz, while x-axis shows the somatic current injections in pA. **A.** I-f curve of granule cell. Corresponding frequency (Hz) to current injections of 0 to +250 pA with 25-pA stepsize. **B.** I-f curve of mossy cell. Corresponding frequency (Hz) to current injections of 0 to +1000 pA with 50-pA stepsize. **C.** I-f curve of Basket cell. Corresponding frequency (Hz) to current injections of 0 to +900 pA with 50-pA stepsize. **D.** I-f curve of HIPP cell. Corresponding frequency (Hz) to current injections of 0 to +200 pA with 25-pA stepsize.

3.1.3 Modeling Synapses

Since the DG network consists of both glutamatergic cells (GCs and MCs) and GABAergic interneurons, AMPA, NMDA and GABA synapses were included in the network model. Therefore, the total synaptic

current (Equations 1 and 4) consisted of two components; the excitatory current through AMPA receptors (I_{AMPA}) and NMDA receptors (I_{NMDA}), and the inhibitory current via $GABA_{\alpha}$ receptors (I_{GABA}). The majority of ligand-gated ion channels mediating synaptic transmission, such as AMPA and GABA receptors, display an approximately linear current-voltage relationship when they open. We modeled these channels as an ohmic conductance (g_{syn}) multiplied by the driving force:

$$I_{syn} = g_{syn}(t) \cdot (V - E_{syn})$$

where E_{syn} is the AMPA and GABA reversal potential, respectively.

The NMDA receptor-mediated conductance depends on the postsynaptic voltage due to the gate blockage by a positively charged magnesium ion (Mg^{2+}). The fraction of NMDA channels that are not blocked by Mg^{2+} can be fitted by a sigmoidal function (Jahr and Stevens, 1990):

$$s(V) = \frac{1}{1 + \eta[Mg^{2+}]_o \, exp(-\gamma V_m)}$$

where η is the sensitivity of Mg unblock, γ the steepness of Mg unblock, and $[Mg^{2+}]_o$ is the outer magnesium (Mg) concentration. For NMDA receptors in MCs, BCs and HIPP cells we used $\eta = 0.28\ \mathrm{mM}^{-1}$, $[Mg^{2+}] = 1\mathrm{mM}$, and $\gamma = 0.072\ \mathrm{mV}^{-1}$. Instead, for GCs we tuned these parameters in to match the latest experimental data found in literature (Krueppel et al., 2011) with the corresponding values equal to $\eta = 0.2\ \mathrm{mM}^{-1}$, $[Mg^{2+}] = 2\mathrm{mM}$, and $\gamma = 0.04\ \mathrm{mV}^{-1}$. Consequently, the NMDA synaptic current is calculated by the following equation:

$$I_{syn} = g_{syn}(t) \cdot s(V) \cdot (V_m(t) - E_{syn})$$

The ohmic conductance is simulated as a sum of two exponentials (Bartos et al., 2001), one term based on rising and the other on the decay phase of the postsynaptic potential. This function allows time constants to be set independently. We simulated such a function as a system of linear differential equations (Roth and Van Rossum, 2009):

$$g_{syn}(t) = g_{max} \cdot u(t)$$

$$\frac{du}{dt} = -\frac{u}{\tau_{decay}} + h_0 \cdot v \cdot (1-u)$$

$$\frac{dv}{dt} = -\frac{v}{\tau_{rise}}$$

where τ_{rise} and τ_{decay} are the rise and decay constants respectively, h_0 a scaling factor and $u(t)$ is the function of two exponentials $u(t) = \exp(-t/\tau_{\mathrm{decay}}) - \exp(-t/\tau_{\mathrm{rise}})$, which is divided by its maximum amplitude in order for the maximum conductance to be equal to one. The scaling factor is set to $1\ \mathrm{ms}^{-1}$ for all AMPA and GABA receptors and all neuronal types. The NMDA scaling factor is set to $0.5\ \mathrm{ms}^{-1}$ apart from the synapses form on GCs where it is set to $2\ \mathrm{ms}^{-1}$. Because axons of neurons are not included in the model, a delay is used between pre- and postsynaptic transmission. The role of the delay is to account for both the synaptic transmission and the axonal conduction delay, and its value depends on the presynaptic and postsynaptic neuronal types. The peak conductance (g_{max}), rise and decay time constants, and the delay of various network connections were estimated from experimental data (Kneisler and Dingledine, 1995; Geiger et al., 1997; Bartos et al., 2001; Schmidt-Hieber et al., 2007; Larimer and Strowbridge, 2008; Schmidt-Hieber and Bischofberger, 2010; Krueppel et al., 2011; Chiang et al., 2012) and are given in Table 4. Specifically, the GC peak conductance both for AMPA and NMDA, was validated against experimental data (Krueppel et al., 2011), where it is evidenced that a single synapse provokes a $0.6\ \mathrm{mV}$ somatic EPSP, and also the NMDA and AMPA peak current ratio is equal to 1.08. These values were reproduced in the GC model cells. The models also incorporate background activity, in order to simulate the experimental findings of spontaneous activity in DG. Accordingly, we used Poisson independent spike trains in order to reproduce the experimental data for MCs (2-4 Hz spontaneous activity) (Henze and Buzsáki, 2007) and for BCs (1-2 Hz spontaneous activity) (Kneisler and Dingledine, 1995). GCs infrequently generate spontaneously activity, even if inhibition is blocked (Lynch et al., 2000). Thus, we implemented noisy inputs in order to only evoke spontaneous EPSPs (0.05 Hz spontaneous activity).

Table 4. Connectivity and synaptic properties

From (column) / To (row)	Granule cells	Mossy cells	Basket cells	HIPP cells
AMPA				
Perforant Path				
g_{max} (nS)	0.8066			0.240
τ_{rise} (ms)	0.1			2.0
τ_{decay} (ms)	2.5			11.0
delay (ms)	3.0			3.0
Granule cells				
g_{max} (nS)		0.500	0.210	
τ_{rise} (ms)		0.5	2.5	
τ_{decay} (ms)		6.2	3.5	
delay (ms)		1.5	0.8	
Mossy cells				
g_{max} (nS)	0.1066		0.350	
τ_{rise} (ms)	0.1		2.5	
τ_{decay} (ms)	2.5		3.5	
delay (ms)	3.0		3.0	
NMDA				
Perforant Path				
g_{max} (nS)	0.8711			0.276
τ_{rise} (ms)	0.33			4.8
τ_{decay} (ms)	50.0			110.0
delay (ms)	3.0			3.0
Granule Cells				
g_{max} (nS)		0.525	0.231	
τ_{rise} (ms)		4.0	10.0	
τ_{decay} (ms)		100.0	130.0	
delay (ms)		1.5	0.8	
Mossy Cells				
g_{max} (nS)	0.1151		0.385	
τ_{rise} (ms)	0.33		10.0	
τ_{decay} (ms)	50.0		130.0	
delay (ms)	3.0		3.0	
$GABA_A$				
Basket cells				
g_{max} (nS)	14.0			
τ_{rise} (ms)	0.9			
τ_{decay} (ms)	6.8			
delay (ms)	0.85			
HIPP cells				
g_{max} (nS)	0.12			
τ_{rise} (ms)	0.9			
τ_{decay} (ms)	6.8			
delay (ms)	1.6			

3.1.4 Connectivity

The DG network model consists of 2000 simulated GCs, a scale that represents 1/500 of the one million GCs found in rat brains (West et al., 1991). The chosen number of GCs provides enough power to explore pattern separation, while maintaining computational efficiency. The population of GCs is organized in non-overlapping clusters, with each cluster containing 20 GCs, respectively. This kind of organization roughly corresponds to the lamellar organization along the septotemporal extent of DG (Sloviter and Lømo, 2012).

Apart from the principal excitatory dentate cells (GCs), the model comprises two kind of inhibitory interneurons, the perisomatic (BCs), which form synapses at the soma of the GCs, and dendritic (HIPP) inhibitory cells, which contact the GCs at their distal dendritic compartments. There is one BC per cluster of GCs, which in turn corresponds to 100 simulated BCs in the model. This is a form of "winner-take-all" competition (Coultrip et al., 1992) in which all, but the most strongly activated GCs in a cluster, are silenced. Given 100 clusters in the model, and with one winner within each cluster, approximately 5% of GCs are active for a given stimulus; this is in agreement with the theoretically and experimentally estimation of 2-5% granular activity in the substrate (Treves et al., 2008; Danielson et al., 2016a). Moreover, the model includes simulated hilar MCs and HIPP cells. Estimated numbers for these neuronal types vary from 30,000 to 50,000 MCs in rats (West et al., 1991; Buckmaster and Jongen-Rêlo, 1999), which in turn corresponds to 3-5 MCs per 100 GCs. Accordingly, the model includes 80 MCs per 2,000 GCs. Experimental counts for HIPP cells vary significantly, but the latest estimates suggest about 12,000 HIPP cells in rats (Buckmaster and Jongen-Rêlo, 1999) meaning less than 2 HIPP cells per 100 GCs. To reflect this empirical data, we simulated 40 HIPP cells in the network model (Fig. 1A).

External input to the network model is provided by 400 afferents representing the major input that DG receives from Entorhinal Cortex (EC) Layer II cells, via the Perforant Path (PP). The ratio of GCs to PP afferents is aligned with estimations of about 200,000 EC Layer II cells in the rat (Amaral et al., 1990), suggesting a ratio of 20 EC cells per 100 GCs. Therefore, the model incorporates synaptic input that

corresponds to 400 EC Layer II cells. For simplicity, the input cells are simulated as independent Poisson spike trains, with frequency of 40 Hz, which is in line with experimental data (Hafting et al., 2005). Previous experimental studies have shown that dentate GCs receive input from 10% of the 4,000 afferents that contact a given GC in the rat during a task (McNaughton et al., 1991), which in turn suggests that an approximate 10% of EC Layer II cells are active. The simulations reported here assume that 10% is the active PP afferents representing a given stimulus. According to McNaughton et al., 1991, 10% of the total entorhinal input is necessary to discharge one GC. However, the EC-GC connection is sparse, with each GC receiving input from about 2% of EC Layer II neurons. Assuming only 400 input cells; one GC could have only 8 afferents from EC, which in turn would make it impossible for the GC to become active. As a compromise, we used a randomly determined 20% of EC Layer II cells as input to each GC and additionally, 20% randomly determined EC Layer II cells as input to each HIPP cell; GCs contact each MC with 20% probability; GCs and HIPP cells each feedback to contact a randomly determined 20% of GCs and finally, each MC connects with every BC in the network. Connections are initialized randomly (uniform random distribution) before the start of the simulations and remain fixed across all simulations (no rewiring). The connectivity matrix was the same for all experiments and across all using GC models, apart from the PP to GCs, and HIPP to GCs synapses due to the difference in GC number of dendrites.

3.2 CA1 network model

The model was developed mainly based on the structure and connectivity features described by (Cutsuridis et al., 2010; Bezaire et al., 2016), and incorporates the major CA1 cell types. These are the CA1PCs, AACs, BCs, BSCs, OLMs and VIP^+/CCK^+ and VIP^+/CR^+ cells. Additionally, the external input to the network was provided by EC LIII, CA3 Schaffer Collaterals and Septum. The principal neurons receive excitatory background activity on their dendrites. All simulations were performed using the NEURON (NEURON v7.3) network simulator (Hines and Carnevale, 1997) running on a High-Performance Computing Cluster (HPCC) with 312 cores under 64-bit CentOS Linux operating system.

3.2.1 Model neurons

All neurons were modeled as simplified biophysical neurons with various numbers of active dendrites using the Hodgkin-Huxley formalism. Specifically, the CA1PCs incorporated various dendrites in order to capture their complex structure; however the interneurons were simulated with a simplistic morphological structure. The morphological structures of neuronal models are shown in Figure 4, while their morphological features are given in Table 5, Table 6 and Table 11. In addition to neuronal models found in (Cutsuridis et al., 2010), we added two more interneurons in the network. Mathematical details for their specific simulated ionic channels are in Appendix B.

Table 5. Morphological properties of Axoaxonic, Basket, Bistratified, VIP^+/CCK^+, VIP^+/CR^+ interneurons

Name of compartment	**Axoaxonic cell**		**Basket cell**		**Bistratified cell**		**VIP^+/CCK^+ cell**		**VIP^+/CR^+ cell**	
	Length x diameter (μm^2) / # compartments		**Length x diameter (μm^2) / # compartments**		**Length x diameter (μm^2) / # compartments**		**Length x diameter (μm^2) / # compartments**		**Length x diameter (μm^2) / # compartments**	
soma	10 x 20	1	10 x 20	1	10 x 20	1	10 x 20	1	10 x 20	1
radProx	4.0 x 100	2	4.0 x 100	2	4.0 x 100	2	4.0 x 100	2	4.0 x 100	2
radMed	3.0 x 100	2	3.0 x 100	2	3.0 x 100	2	3.0 x 100	2	3.0 x 100	2
radDist	2.0 x 200	2	2.0 x 200	2	2.0 x 200	2	2.0 x 200	2	2.0 x 200	2
lmM	1.5 x 100	2	1.5 x 100	2	-	-	1.5 x 100	2	1.5 x 100	2
lmt	1.0 x 100	2	1.0 x 100	2	-	-	1.0 x 100	2	1.0 x 100	2
oriProx	2.0 x 100	2	2.0 x 100	2	2.0 x 100	2	2.0 x 100	2	2.0 x 100	2
oriMed	1.5 x 100	2	1.5 x 100	2	1.5 x 100	2	1.5 x 100	2	1.5 x 100	2
oriDist	1.0 x 100	2	1.0 x 100	2	1.0 x 100	2	1.0 x 100	2	1.0 x 100	2
Total		17		17		13		17		17

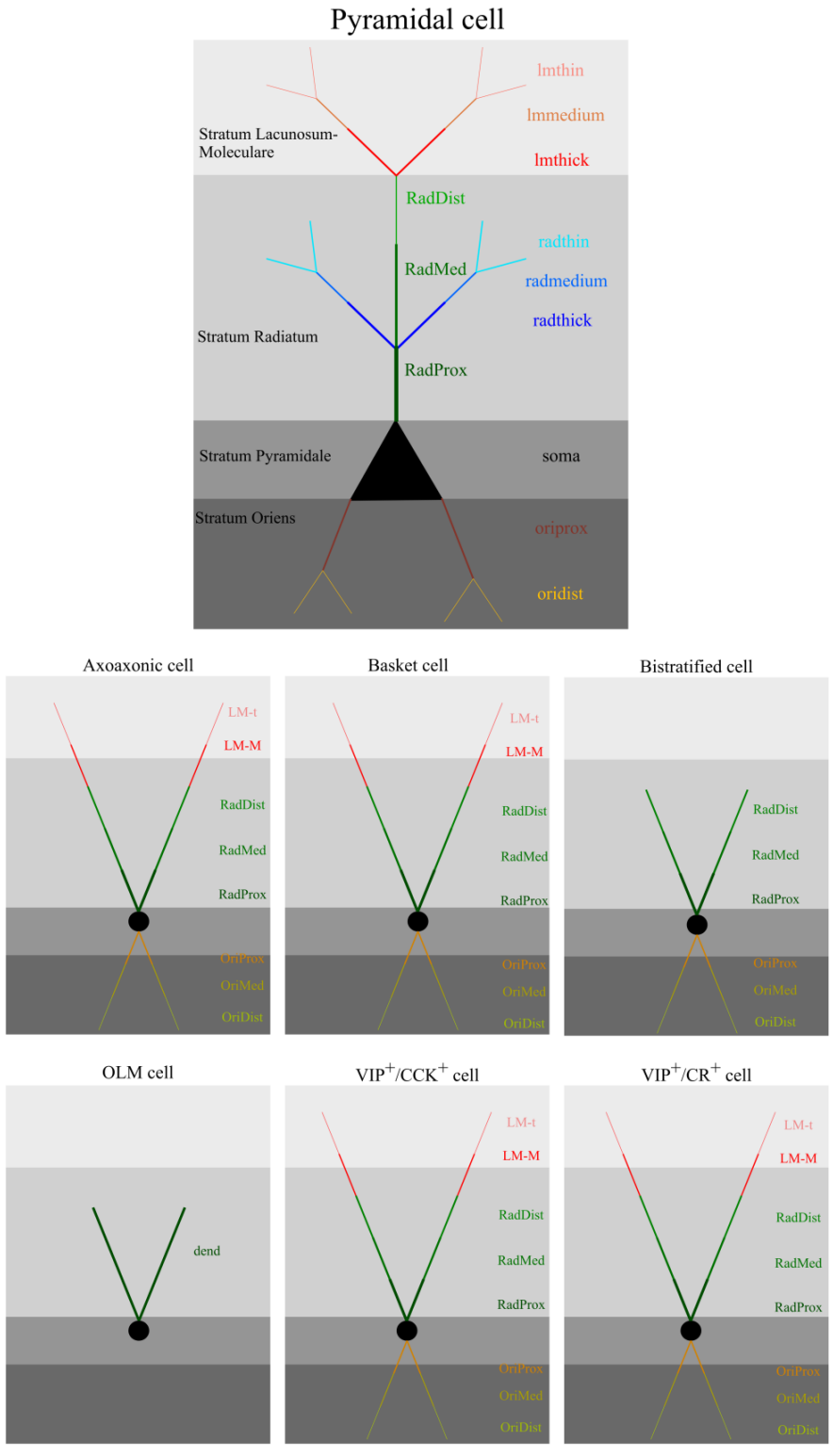

Figure 4. Morphological structure of neuronal models.

A. Schematic diagram of the pyramidal cell. The different colors represent the different compartments. The model includes also an axon (not shown here for consistency). The grey-scale shaded area denotes the different layers found in CA1 subregion. B. As

in A, but here the schematic diagrams of the Axoaxonic, Basket, Bistratified, OLM, VIP/CCK and VIP/C models are shown. Yet again, the shaded area represents the different layers. Note that the thickness and the length of each compartment is not represent the values we used, rather they used for clarity.

3.2.1.1 Simplified Pyramidal cell

The pyramidal cell (CA1PC) was implemented as per Cutsuridis et al, 2010 and modified accordingly in order to be more complex. Each CA1PC had 27 compartments, each containing a calcium pump and buffering mechanism, calcium activated slow AHP and medium AHP potassium (K^+) currents, an HVA L-type Ca^{2+} current, an HVA R-type Ca^{2+} current, an LVA T-type Ca^{2+} current, an h current, a fast sodium and a delayed rectifier K^+ current, a slowly inactivating K^+ M-type current and a fast inactivating K^+ A-type current (Poirazi et al., 2003a, 2003b). Each PC soma rested in the SP, while its dendrites extended across the strata from SO (basal dendrites) to SR and SLM (proximal and distal apical dendrites). Each pyramidal cell received somatic synaptic inhibition from the basket cells, mid-dendritic excitation from CA3, distal apical excitation from the entorhinal cortex (EC), and proximal excitation from around 1% of other pyramidal cells in the network, somatic inhibition from the BC and VIPCCK, axonic inhibition from the AAC, mid-dendritic synaptic inhibition from the BSC population, and distal synaptic inhibition on each from the OLM cell. Thus, we added more compartments (sister branches) at distal, medial and basal dendrites. In addition, we used a series of dendritic channels as described in Appendix B. The maximum conductance of each channel is given in Table 7.

Table 6. Morphological properties of the Pyramidal Cell

Name	**Dimensions (diameter x length) μm^2**	**Number of compartments**
Soma	10 x 10	1
Axon	1.0 x 150	1
RadProx	4.0 x 100	1
RadMed	3.0 x 100	1
RadDist	2.0 x 200	1
radthick	2.0 x 100	2
radmedium	1.5 x 100	2
radthin	1.0 x 50	4
lmthick	2.0 x 100	2
lmmedium	1.5 x 100	2

lmthin	1.0 x 50	4
oriprox	2.0 x 100	2
oridist	1.5 x 100	4
Total		27

Table 7. Passive parameters and active ionic conductances of channels for all compartments of pyramidal model cells

	Compartment							
Mechanism	**Soma**	**Axon**	**RadProx**	**RadMed**	**RadDist**	**LM/R**	**OriProx**	**OriDist**
Leak conductance [S/cm^2]	0.0002	0.0002	0.0002	0.0002	0.0002	0.0002	0.0002	0.0002
Na^+ conductance [S/cm^2]	0.007	0.007	0.007	0.007	0.007	0.007	0.007	0.007
Delayed rectifier K^+ conductance [S/cm^2]	0.0014	0.0014	0.0014	0.0014	0.0014	0.0014	0.0014	0.0014
Proximal A-type K^+ conductance [S/cm^2]	0.0075	0.0075	0.0075	0.0075	0.0075	0.0075	0.0075	0.0075
Distal A-type K^+ conductance [S/cm^2]	-	-	-	-	-	-	-	-
M-type K^+ conductance [S/cm^2]	0.06	0.06	0.06	0.06	0.06	0.06	0.06	0.06
I_h conductance [S/cm^2]	0.00005	0.00005	0.00005	0.00005	0.00005	0.00005	0.00005	0.00005
L-type Ca^{2+} conductance [S/cm^2]	0.0007	0.0007	0.0007	0.0007	0.0007	0.0007	0.0007	0.0007
R-type Ca^{2+} conductance [S/cm^2]	0.0003	0.0003	0.0003	0.0003	0.0003	0.0003	0.0003	0.0003
T-type Ca^{2+} conductance [S/cm^2]	0.00005	0.00005	0.00005	0.00005	0.00005	0.00005	0.00005	0.00005
$Ca2^+$-dependent mAHP K^+ conductance [S/cm^2]	0.0005	0.0005	0.0005	0.0005	0.0005	0.0005	0.0005	0.0005
$Ca2^+$-dependent sAHP K^+ conductance [S/cm^2]	0.09075	0.09075	0.09075	0.09075	0.09075	0.09075	0.09075	0.09075
Membrane capacitance C_m [μF/cm^2]	1	1	1	1	1	1	1	1
Membrane resistance R_m [Ohm cm^2]	20,000	20,000	20,000	20,000	20,000	20,000	20,000	20,000
Axial resistance R_a [Ohm cm]	150	150	150	150	150	150	150	150
$V_{half,h}$ [mV]	-73	-73	-73	-73	-73	-73	-73	-73
E_L [mV]	-70	-70	-70	-70	-70	-70	-70	-70
E_{Na} [mV]	50	50	50	50	50	50	50	50
E_K [mV]	-80	-80	-80	-80	-80	-80	-80	-80
E_h [mV]	-10	-10	-10	-10	-10	-10	-10	-10
E_{Ca} [mV]	140	140	140	140	140	140	140	140

3.2.1.2 Axoaxonic Cell (AAC)

Each AAC consisted of 17 compartments, which included a leak conductance, a sodium (Na^+) current, a fast delayed rectifier potassium (K^+) current, an A-type K^+ current, L- and N-type calcium (Ca^{2+}) currents, a Ca^{2+}-dependent K^+ current and a Ca^{2+}-dependent and voltage-dependent K^+ current (Table 8). AACs received excitatory inputs from the EC LIII to their SLM dendrites and excitatory inputs from the CA3 Schaffer collateral to their SR dendrites. In addition, the AACs received inputs from the CA1PCs in their

SR medium and thick dendritic compartments as well as inhibitory input from the septum in their SO thick dendritic compartments. Moreover, they received inhibitory input from BCs, BSCs and OLMs to their soma and dendrites, respectively.

Table 8. Passive parameters and active ionic conductance of channels of Axoaxonic cell

Mechanism	**All compartments**
Leak conductance [S/cm^2]	0.00018
Na^+ conductance [S/cm^2]	0.15
Delayed rectifier K^+ conductance [S/cm^2]	0.013
A-type K^+ conductance [S/cm^2]	0.00015
L-type Ca^{2+} conductance [S/cm^2]	0.005
N-type Ca^{2+} conductance [S/cm^2]	0.0008
Ca^{2+}-dependent K^+ conductance [S/cm^2]	0.000002
Ca^{2+}- and voltage dependent K^+ conductance [S/cm^2]	0.0002
Membrane capacitance C_m [µF/cm^2]	1.4
Axial resistance R_a [Ohm cm]	100
E_L [mV]	-60
E_{Na} [mV]	55
E_K [mV]	-90
E_{Ca} [mV]	130
$[Ca^{2+}]$ steady state [mM]	0.000005
$[Ca^{2+}]_o$	2
τ_{Ca} [ms]	10

3.2.1.3 Basket Cell (BC)

Each BC consisted of 17 compartments, containing a leak conductance, a Na^+ current, a fast and slow delayed rectifier K^+ current, an A-type K^+ current, L- and N-type Ca^{2+} currents, a Ca^{2+}- dependent K^+ current, and a Ca^{2+}- and voltage-dependent K^+ current (Table 9). All BCs received excitatory connections from the EC LIII to their distal SLM dendrites, from the CA3 Schaffer collaterals to their medium SR dendrites and from active pyramidal cells to their medium and thick SR dendritic compartments and inhibitory connections from neighboring BCs, BSCs, OLMs and VIPCRs in their soma and dendrites (Freund and Buzsáki, 1996; Bezaire and Soltész, 2013) and from the medial septum in their SO thick dendritic compartments.

Table 9. Passive parameters and active ionic conductance of channels of Basket cell

Mechanism	All compartments
Leak conductance [S/cm^2]	0.00018
Na^+ conductance [S/cm^2]	0.2
Delayed rectifier K^+ conductance [S/cm^2]	0.013
A-type K^+ conductance [S/cm^2]	0.00015
L-type Ca^{2+} conductance [S/cm^2]	0.005
N-type Ca^{2+} conductance [S/cm^2]	0.0008
Ca^{2+}-dependent K^+ conductance [S/cm^2]	0.000002
Ca^{2+}- and voltage dependent K^+ conductance [S/cm^2]	0.0002
Membrane capacitance C_m [µF/cm^2]	1.4
Axial resistance R_a [Ohm cm]	100
E_L [mV]	-60
E_{Na} [mV]	55
E_K [mV]	-90
E_{Ca} [mV]	130
$[Ca^{2+}]$ steady state [mM]	0.000005
$[Ca^{2+}]_o$	2
τ_{Ca} [ms]	10

3.2.1.4 Bistratified Cell (BSC)

Each BSC consisted of 13 compartments, which included the same ionic currents as the BC and AAC cells (Table 10). All BSCs received excitatory connections from the CA3 Schaffer collaterals in their medium SR dendritic compartments and from the active pyramidal cells in their thick SO dendritic compartments and inhibitory connections from the medial septum in their thick SO dendritic compartments and from neighboring BC, BSC, OLM and VIPCCK cells in both their somata and dendrites.

Table 10. Passive parameters and active ionic conductance of channels of Basket cell

Mechanism	All compartments
Leak conductance [S/cm^2]	0.00018
Na^+ conductance [S/cm^2]	0.3
Delayed rectifier K^+ conductance [S/cm^2]	0.013
A-type K^+ conductance [S/cm^2]	0.00015
L-type Ca^{2+} conductance [S/cm^2]	0.005
N-type Ca^{2+} conductance [S/cm^2]	0.0008
Ca^{2+}-dependent K^+ conductance [S/cm^2]	0.000002
Ca^{2+}- and voltage dependent K^+ conductance [S/cm^2]	0.0002
Membrane capacitance C_m [µF/cm^2]	1.4
Axial resistance R_a [Ohm cm]	100

E_L [mV]	-60
E_{Na} [mV]	55
E_K [mV]	-90
E_{Ca} [mV]	130
$[Ca^{2+}]$ steady state [mM]	0.000005
$[Ca^{2+}]_o$	2
τ_{Ca} [ms]	10

3.2.1.5 O-LM Cell (OLM)

Each OLM cell had four compartments, which included a Na^+ current, a delayed rectifier K^+ current, an A-type K^+ current, and an h-current (Table 12). Each OLM cell received excitatory connections from the CA1PCs in their basal dendrites as well as inhibitory connections from the BCs, BSCs, OLMs, and VIPCRs and form medial septum in their soma.

Table 11. Morphological properties of OLM cells.

Name	**Dimensions (diameter x length) µm^2**	**Number of compartments**
Soma	10 x 20	1
Axon	3.0 x 250	1
dend	1.5 x 150	2
Total		4

Table 12. Passive properties and active ionic conductance of OLM cell

	Compartment		
Mechanism	**Soma**	**Axon**	**Dendrite**
Leak conductance [S/cm^2]	0.00005	0.00005	0.00005
Na^+ conductance [S/cm^2]	0.0107	0.01712	0.0234
Delayed rectifier K^+ conductance [S/cm^2]	0.0319	0.05104	0.0460
A-type K^+ conductance [S/cm^2]	0.0165	0.00015	0.004
Membrane capacitance C_m [µF/cm^2]	1.3	1.3	1.3
Axial resistance R_a [Ohm cm]	150	150	150
E_L [mV]	-65	-65	-65
E_{Na} [mV]	90	90	90
E_K [mV]	-100	-100	-100

3.2.1.6 VIP$^+$/CCK$^+$ Cell (VIPCCK)

Each VIPCCK cell had 17 compartments, containing a leak conductance, a sodium current, a fast delayed rectifier K^+ current, an A-type K^+ current, L- and N-type Ca^{2+} currents, a Ca^{2+}- dependent K^+ current, and

a Ca^{2+}- and voltage-dependent K^+ current (Table 13). All VIPCCKs received excitatory connections from the EC LIII to their distal SLM dendrites, from the CA3 Schaffer collaterals to their medium SR dendrites and from active pyramidal cells to their medium and thick SR dendritic compartments and inhibitory connections from neighboring BCs, BSCs and OLMs in their soma (Bezaire and Soltész, 2013) and from the medial septum in their SO thick dendritic compartments.

Table 13. Passive properties and active ionic conductance of VIP^+/CCK^+ cell

Mechanism	**All compartments**
Leak conductance [S/cm^2]	0.00018
Na^+ conductance [S/cm^2]	0.3
Delayed rectifier K^+ conductance [S/cm^2]	0.013
A-type K^+ conductance [S/cm^2]	0.00015
L-type Ca^{2+} conductance [S/cm^2]	0.005
N-type Ca^{2+} conductance [S/cm^2]	0.0008
Ca^{2+}-dependent K^+ conductance [S/cm^2]	0.000002
Ca^{2+}- and voltage dependent K^+ conductance [S/cm^2]	0.0002
Membrane capacitance C_m [$\mu F/cm^2$]	1.4
Axial resistance R_a [Ohm cm]	100
E_L [mV]	-60
E_{Na} [mV]	55
E_K [mV]	-90
E_{Ca} [mV]	130
$[Ca^{2+}]$ steady state [mM]	0.000005
$[Ca^{2+}]_o$	2
τ_{Ca} [ms]	10

3.2.1.7 VIP^+/CR^+

The CR interneuron model consisted of 17 compartments including mechanisms for slow K^+ current, fast Ca^{2+}-activated K^+ current and N-type Ca^{2+} current (Table 14). Each VIPCR cell received excitatory input from EC LIII, CA3 Schaffer collateral and CA1PCs. Also, it received inhibitory input from medial septum at the somatic compartment. This cell was then validated against experimental evidence (Tyan et al., 2014; Francavilla et al., 2015).

Table 14. Passive properties and active ionic conductance of VIP^+/CR^+ cell

Mechanism	**All compartments**	
	Soma	**Dendrites**
Leak conductance [S/cm^2]	0.00005	0.00005
Na^+ conductance [S/cm^2]	0.015	0.075
Delayed rectifier K^+ conductance [S/cm^2]	0.018	0.009

D-type K^+ conductance [S/cm^2]	0.000725	-
N-type Ca^{2+} conductance [S/cm^2]	0.001	-
Ca^{2+}-dependent K^+ conductance [S/cm^2]	0.00003	-
Membrane capacitance C_m [µF/cm^2]	1.2	1.2
Axial resistance R_a [Ohm cm]	150	150
E_L [mV]	-65	-65
E_{Na} [mV]	55	55
E_K [mV]	-90	-90
E_{Ca} [mV]	130	130

3.2.2 Validation

The first step was to validate the passive (intrinsic) properties of every individual neuronal type against experimental evidence. In this line, we used the input resistance, the rheobase current, and the membrane time constant. The passive membrane properties are given in Table 15 and in Figure 5.

Table 15. Passive properties of neuronal models in CA1

Cell	**R_{in} (MΩ)**		**τ_m (ms)**		**V_{rest} (mV)**		**rheobase (pA)**	
	Model	Biological	Model	Biological	Model	Biological	Model	Biological
PCs	85.9	139.5 ± 38	9.4	21.5 ± 8.6	-64.9	-70.7 ± 1.2	110	182.4 ± 55
AACs	70.0	122 ± 57	11.1	11.9 ± 2.2	-64.4	-64.4 ± 4.5	270	283 ± 152
BCs	98.4	56 ± 9	16.4	13.3 ± 5.4	-64.3	-61.4 ± 2.0	150	307 ± 109
BSCs	98.7	109 ± 30	14.8	12.2 ± 0.6	-67.0	-63.6 ± 4.7	260	101 ± 24
OLMs	507.1	592.3 ± 97	21.3	30.0 ± 12	-65.9	-65.2 ± 1.3	30	20 ± 0
VIPCCKs	228.8	281.7 ± 78	22.2	25.5 ± 5	-61.4	-61.4 ± 3.2	50	60 ± 0
VIPCRs	318.3	320	26.0	25.0	-63.2	-63.0	20	-
Sources	Bezaire et al, 2016, Tyan et al, 2014							

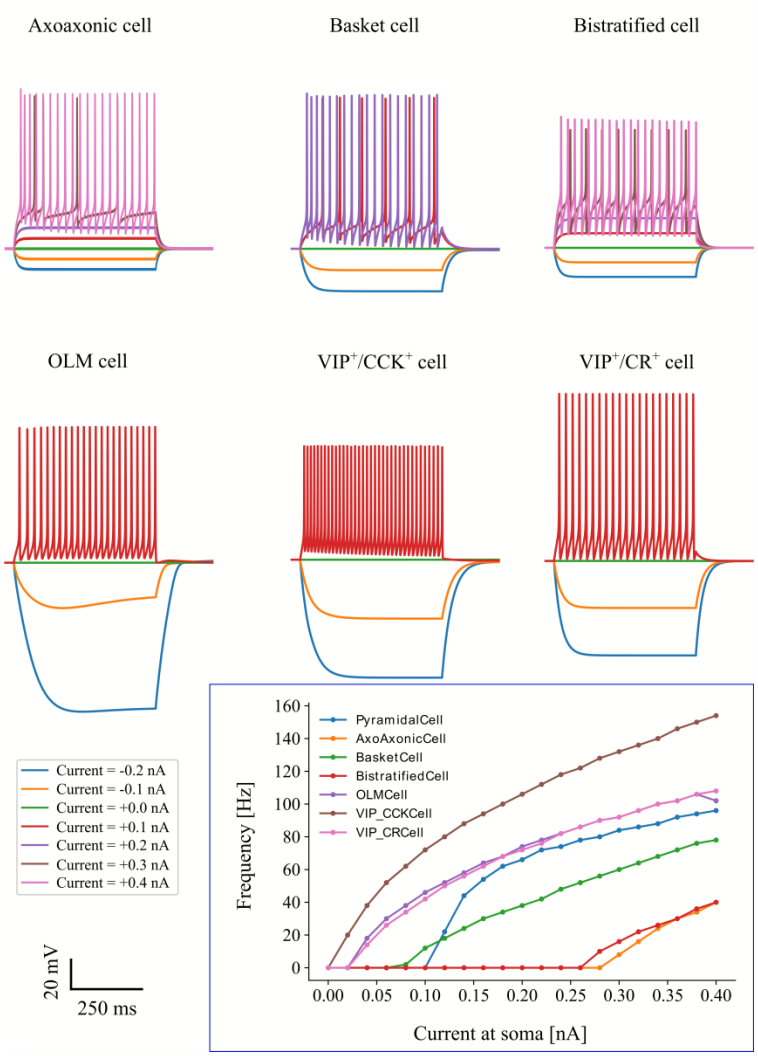

Figure 5. Validation of neuronal models.

3.2.3 Modeling Synapses

Since the CA1 network consists of both glutamatergic cells (CA1PCs) and GABAergic interneurons, AMPA, NMDA and $GABA_A$ and $GABA_B$ synapses were included in the network model. More specific, we used NMDA synapses on pyramidal neurons only. The interneurons receive excitatory afferents via AMPA only, as NMDA on those neurons is not well studied yet. Yet again, the AMPA, NMDA, $GABA_A$ and $GABA_B$ synapses are simulated as a sum of two exponentials (§ 3.1.3 for more details). All synaptic properties (i.e., conductance g, rise time τ_r, and decay time τ_d) are the same as in Bezaire et al, 2016 (Table 17). For simplicity, all conduction delays are set to 1.0 ms.

AMPA, GABA synapses

The AMPA, $GABA_A$ and $GABA_B$ synapses were simulated as a two state kinetic scheme and is described as a rise phase and a decay phase. The synaptic current through these synapses is calculated by the following equations:

$$I_{syn} = g_{syn}(t) \cdot (V - E_{syn}), syn \, \epsilon \, \{ampa, gaba_A, gaba_B\}$$

$$g_{syn}(t) = B(t) - A(t), \;\; A(t) = e^{\left(-\frac{t}{\tau_{rise}}\right)}, B(t) = -\left(\frac{\tau_{decay}}{\tau_{decay} - \tau_{rise}}\right) \cdot A(t) + e^{\left(-\frac{t}{\tau_{decay}}\right)}$$

NMDA synapse

The NMDA synapse was simulated as a two state kinetic scheme as well, but it involved also a factor with represented the voltage dependency. The corresponding equations were:

$$I_{nmda} = g_{nmda}(t) \cdot s(V) \cdot (V - E_{nmda})$$

$$g_{nmda}(t) = B(t) - A(t), \;\; A(t) = e^{\left(-\frac{t}{\tau_{rise}}\right)}, B(t) = -\left(\frac{\tau_{decay}}{\tau_{decay} - \tau_{rise}}\right) \cdot A(t) + e^{\left(-\frac{t}{\tau_{decay}}\right)}$$

$$s(V) = \frac{1.50265}{1 + 0.33 \cdot e^{-0.0625 \cdot V}}$$

where V is the membrane voltage (more details in §3.1.3).

3.2.4 Connectivity

The CA1 network model consists of 98 simulated neurons, with 80 pyramidal neurons and 18 interneurons. Although the chosen number of CA1PCs represents only a small portion of neurons found in adult rat brain, which are 320,000 – 380,000 (West et al., 1991), yet provides enough power to explore place cell dynamics, while upholding computational complexity at significantly convenient levels.

Apart from the principal neurons, which were the majority in our network, the model consists of various types of interneurons. The majority of this sub-population was the PV^+ expressing cells consisting of

BCs, AACs and BSCs. We simulated eight BCs, two AACs and two BSCs providing the principal neurons with perisomatic, axonal and dendritic inhibition, respectively. These neurons are the majority of total interneurons found in CA1, with BCs to outnumber rest of other inhibitory neuronal types (Baude et al., 2007). Furthermore, we included SOM^+ interneurons in the network, OLM, which contacted principal neurons at distal dendrites providing the network with dendritic inhibition. Finally, we added two more types in the network, two CCK^+/VIP^+ which innervate the soma of principal neurons and two CR^+/VIP^+ which inhibit both BCs and OLMs by contacting them at their somatic compartment. Interestingly, an immense number of interconnections within interneurons were presented in the network (Figure 6).

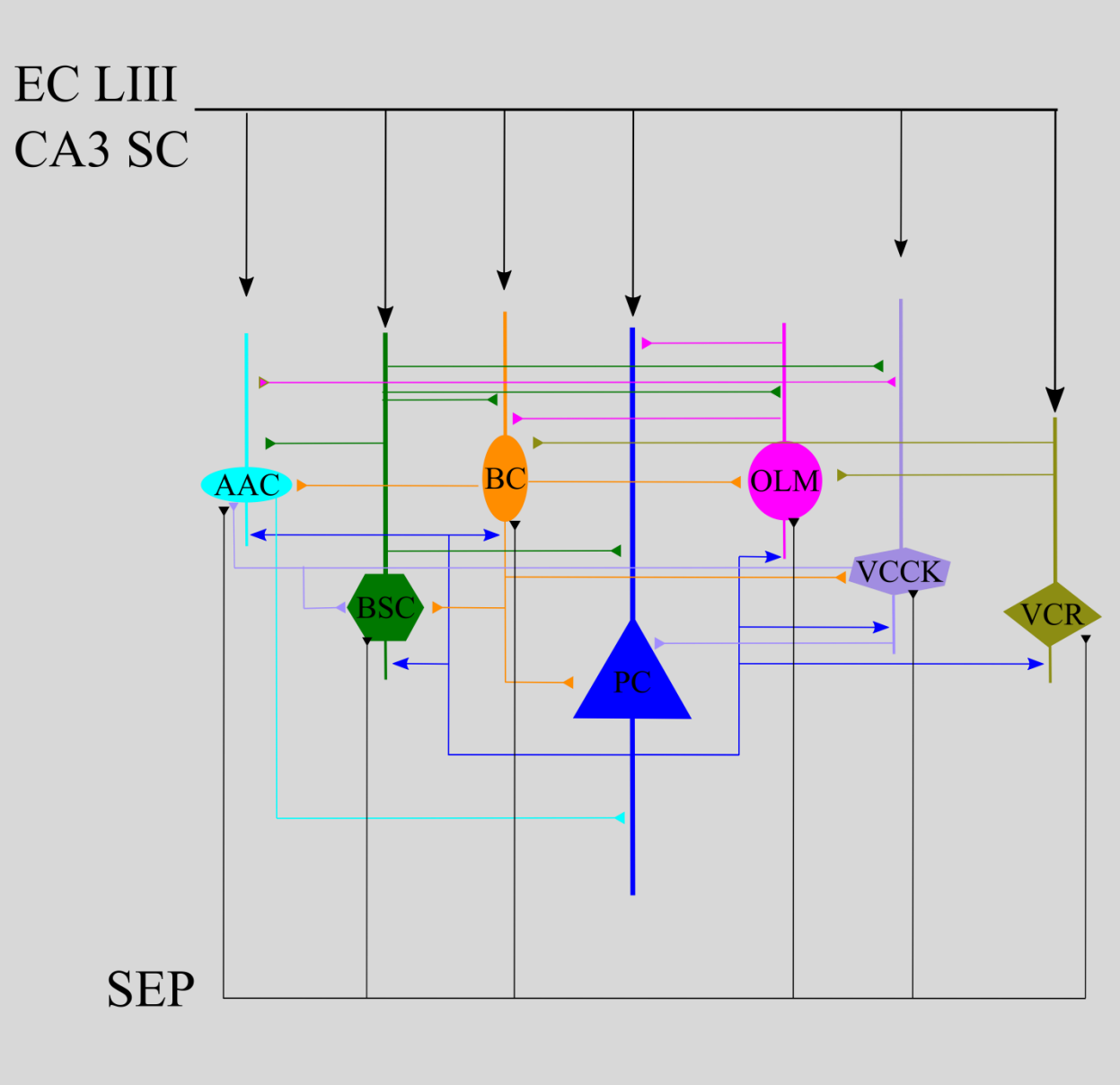

Figure 6. The CA1 network model.

The input is provided from CA3 SC, EC LIII and SEP (only to interneurons). There is a high complexity to the network as interneurons form local circuitries with other internueronal populations. AAC: Axo-axonic cell, BC: Basket cell, BSC: Bistratified cell, OLM: O-LM cell, VIPCCK: VIP^+/CCK^+ basket cell, VIP^+/CR^+ cell. Notice that VIP^+ cells provided the network with perisomatic inhibition and disinhibition. The SEP innervates all interneurons with GABAergic synapses.

The number of connections receives each pyramidal neuron from the EC LIII and the CA3 pyramidal cells were equal to eight as any CA1PC receives an octal of grid-like inputs. The connections from and on

interneurons were approximated as per (Bezaire and Soltész, 2013; Bezaire et al., 2016). All connections were scaled down 36 times in order to be in line with the decrease in neuronal numbers. The connectivity features are given in detail in Table 16. Finally, all interneurons receive $GABA_A$ and $GABA_B$ inhibitory connections from septum in order to maintain the theta cycle observed in hippocampus.

Table 16. Connectivity properties of CA1 network

From/to	CA1PCs	AACs	BCs	BSCs	OLMs	VIPCCKs	VIPCRs
EC LIII	8	27	3	24	x	10	30
CA3	8	231	336	321	55	111	139
SEP	x	10	10	10	10	10	10
CA1PC	3	14	35	31	198	115	115
AAC	1	1	x	x	x	x	x
BC	3	5	1	1	x	1	x
BSC	2	3	4	4	11	4	x
OLM	2	3	3	3	2	11	x
VIPCCK	2	3	x	3	x	8	x
VIPCR	x	x	3	x	11	x	x

Table 17. Synaptic properties of CA1 network connections

From/to		CA1PCs		AACs		BCs		BSCs		OLMs		VIPCCKs		VIPCRs	
EC LIII		AMPA	NMDA	AMPA		AMPA		AMPA		AMPA		AMPA		AMPA	
	g (nS)	2.0e-4	2.0e-4	1.2e-4		0.1e-4		1.5e-4		x		3.0e-4		3.0e-4	
	τ_r (ms)	0.5	2.3	2.0		2.0		2.0		x		2.0		2.0	
	τ_d (ms)	3.0	100	6.3		6.3		6.3		x		6.3		6.3	
CA3 SC		AMPA	NMDA	AMPA		AMPA		AMPA		AMPA		AMPA		AMPA	
	g (nS)	1.5e-4	1.5e-4	1.2e-4		2.2e-4		1.5e-4		1.05e-4		1.05e-4		1.05e-4	
	τ_r (ms)	0.5	2.3	2.0		2.0		2.0		2.0		2.0		2.0	
	τ_d (ms)	3.0	100	6.3		6.3		6.3		6.3		6.3		6.3	
SEP		$GABA_A$	$GABA_B$	$GABA_A$	$GABA_B$	$GABA_A$	$GABA_B$	$GABA_A$	$GABA_B$	$GABA_A$	$GABA_B$	$GABA_A$	$GABA_B$	$GABA_A$	$GABA_B$
	g (nS)	x	x	2.0e-4	2.0e-4	8.0e-4	8.0e-4	8.0e-4	8.0e-4	0.1e-5	0.1e-5	2.0e-4	2.0e-4	2.0e-4	2.0e-4
	τ_r (ms)	x	x	1	35	1	35	1	35	1	35	1	35	1	35
	τ_d (ms)	x	x	8	100	8	100	8	100	8	100	8	100	8	100
CA1PCs		AMPA		AMPA		AMPA		AMPA		AMPA		AMPA		AMPA	
	g (nS)	7.0e-3		4.0e-5		7.0e-4		1.9e-3		2.0e-4		5.0e-4		5.0e-4	
	τ_r (ms)	0.1		0.3		0.07		0.11		0.3		0.5		0.5	
	τ_d (ms)	9.5		0.6		0.20		0.25		0.6		3.0		3.0	
AACs		$GABA_A$		$GABA_A$		$GABA_A$		$GABA_A$		$GABA_A$		$GABA_A$		$GABA_A$	
	g (nS)	1.15e-3		x		x		x		x		x		x	
	τ_r (ms)	0.28		x		x		x		x		x		x	
	τ_d (ms)	8.40		x		x		x		x		x		x	
BCs		$GABA_A$		$GABA_A$		$GABA_A$		$GABA_A$		$GABA_A$		$GABA_A$		$GABA_A$	
	g (nS)	2.0e-4		1.2e-4		1.6e-3		2.9e-3		x		1.2e-3		x	
	τ_r (ms)	0.3		0.29		0.08		0.29		x		0.29		x	
	τ_d (ms)	6.2		2.67		4.80		2.67		x		2.67		x	
BSCs		$GABA_A$	$GABA_B$	$GABA_A$		$GABA_A$		$GABA_A$		$GABA_A$		$GABA_A$		$GABA_A$	
	g (nS)	5.1e-4	1.1e-4	6.0e-4		9.0e-3		5.1e-4		2.0e-5		8.0e-4		x	
	τ_{rise} (ms)	0.11	35	0.29		0.29		0.29		1.0		0.29		x	
	τ_{decay}(ms)	9.70	100	2.67		2.67		2.67		8.0		2.67		x	
OLMs		$GABA_A$	$GABA_B$	$GABA_A$		$GABA_A$		$GABA_A$		$GABA_A$		$GABA_A$		$GABA_A$	
	g (nS)	3.0e-4	3.0e-4	1.2e-4		1.1e-3		1.1e-4		1.2e-3		1.2e-3		x	
	τ_r (ms)	0.13	35	0.73		0.25		0.6		0.25		0.73		x	
	τ_d (ms)	11.0	100	10.0		7.50		15		7.50		20.20		x	
VIPCCKs		$GABA_A$		$GABA_A$		$GABA_A$		$GABA_A$		$GABA_A$		$GABA_A$		$GABA_A$	
	g (nS)	5.2e-4		7.0e-4		x		7.0e-4		x		4.5e-4		x	
	τ_r (ms)	0.3		0.43		x		0.43		x		0.43		x	
	τ_d (ms)	4.2		4.49		x		4.49		x		4.49		x	
VIPCRs		$GABA_A$		$GABA_A$		$GABA_A$		$GABA_A$		$GABA_A$		$GABA_A$		$GABA_A$	
	g (nS)	x		x		9.0e-3		x		7.0e-4		x		x	
	τ_r (ms)	x		x		0.43		x		1.0		x		x	
	τ_d (ms)	x		x		4.49		x		8.0		x		x	

Chapter 4 GC dendrites mediate pattern separation via controlling sparsity

4.1 Preamble

It is widely hypothesized that hippocampus plays a critical role in pattern separation, the process of converting similar incoming information to highly dissimilar, non-overlapping representations. Sparse firing granule cells (GCs), which are the principal neurons in the Dentate Gyrus (DG), have been proposed to undertake this computation, but which of their specific properties mediate pattern separation remains highly elusive. Dendritic atrophy has been reported in diseases associated with pattern separation deficits and adult neurogenesis has been shown that affects pattern separation, suggesting a possible role for dendrites during this computational task. To examine whether and how the dendrites of GCs contribute to pattern separation, we have implemented a simplified, biologically relevant, computational model of the DG. Our model suggests that the presence of GC dendrites is associated with high pattern separation efficiency while their atrophy leads to increased excitability and performance deficits. Additionally, these deficits can be rescued by restoring GC sparsity to control levels through various manipulations. Thus, we have predicted that dendrites contribute to pattern separation as a mechanism for controlling GC sparsity.

4.2 Materials & Methods

To investigate this possibility, we implemented a morphologically simple, yet biologically relevant, scaled-down spiking neural network model of the DG. The model consists of four types of cells (MCs, BCs, HIPP and GCs) modeled as simplified integrate-and-fire neurons. The GC model alone was extended to incorporate dendrites. The electrophysiological properties of all cell types were calibrated according to a range of experimental data. An advantage of using such a simplified approach lies in the small number of parameters that make it possible to characterize their role in the behavior of the model.

Despite its simplicity, the model exhibits realistic pattern separation under several conditions and explains how inhibition to GCs provided directly from BCs and indirectly via the inhibitory circuitry through MCs impact this task, as suggested by a number of recent studies (Myers and Scharfman, 2011; Jinde et al., 2012), thus, supporting its biological relevance. We use the model to investigate whether and how GC dendrites may contribute to pattern separation. Specifically, these neurons are the granule cells, the mossy cells, the basket cells and the HIPP cells. The network and its neuronal models and their synaptic properties are extensively described in Chapter 3 and its schematic representation is shown in Figure 7. Below, we describe the stimulus and the protocol we have used to study pattern separation.

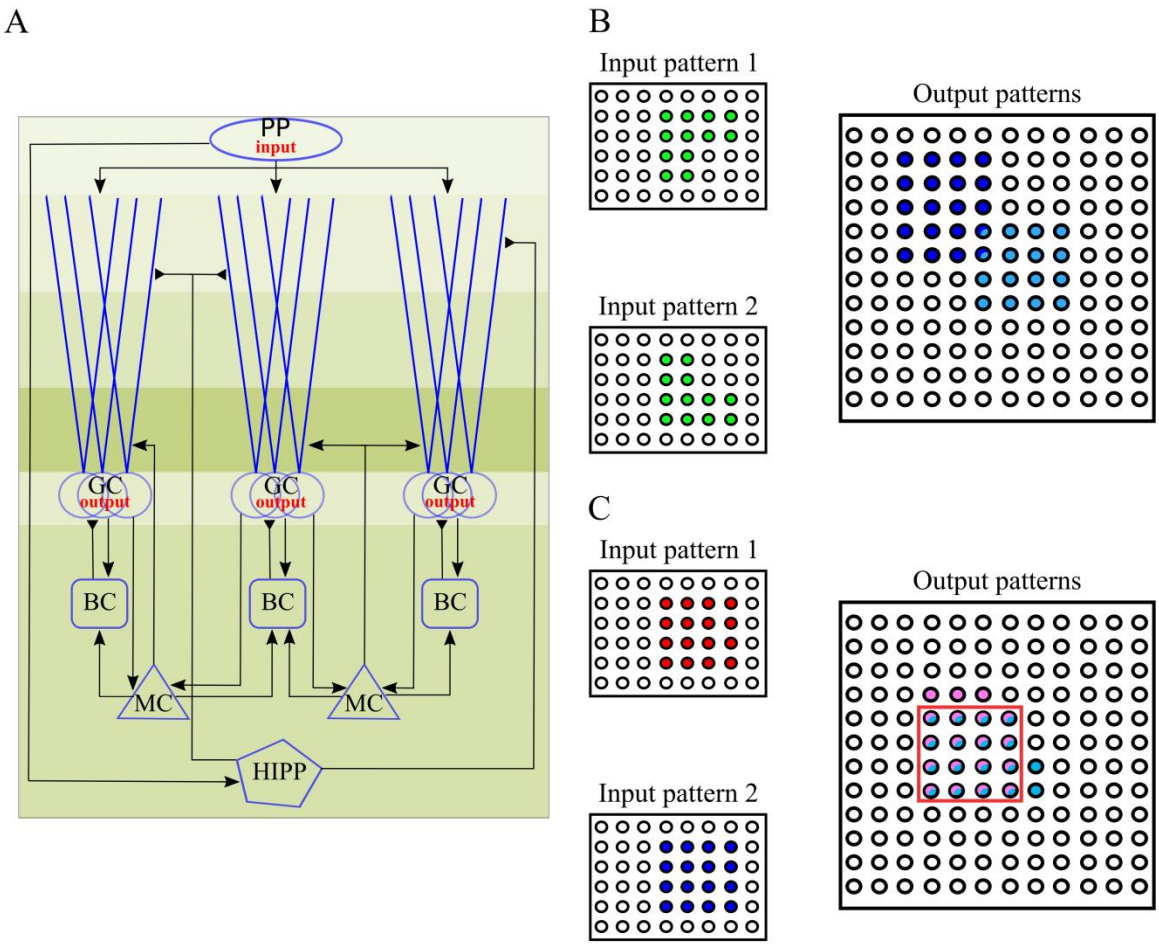

Figure 7. Schematic diagram of DG network and pattern separation task.

A. Schematic representation of the implemented DG network model. Different shades of green illustrate the layer division. PP: perforant path, GC: granule cells, BC: basket cells, MC: Mossy cells, HIPP: hilar perforant path-associated cells. Perforant path afferents curry the input to the network, and project on both the GCs and the HIPP cells. MCs and GCs are connected in a recurrent manner. GCs provide the output of the DG network. **B.** Schematic representation of pattern separation using population-based approach. When two highly overlapping EC inputs (input patterns 1 and 2, with equal mean firing rates) arrive in DG, the corresponding outputs are highly dissimilar. Note that the output pattern is sparse because of the low number of GCs that encode any given pattern. **C.** Schematic representation of pattern separation using rate-based approach. When two highly overlapping EC inputs (input patterns 1 and 2, with different mean firing rates but equal input populations) arrive in DG, the corresponding outputs are highly dissimilar in their firing rates but also likely to differ in the populations they activate. Rate distances are estimated over the set of common neurons (red box).

4.2.1 Model manipulations

4.2.1.1 GC dendritic models

In order to study the effect of dendrites in pattern separation, we have used two different approaches. First, we have used two additional GC neuronal models with fewer dendrites. Starting from the control model consists of 12 dendrites, we have reduced to half (6-dendrite model) and to quarter (3-dendrites model) by removing various number of compartments, respectively. Note that the total path length remains the same across models and only the dendritic complexity has been changed. Subsequently, we examined the dendritic integration profile for all models (Figure 8A and B).

The second approach was to perform the opposite experiment and therefore, we have started from a model with three, short and thick dendrites. Thereafter, we have added various numbers of compartments and hence, the path length as well as the complexity has been increased in order to have the 6- and 12-dendrite models (Figure 8C). It is important to mention that the 12-dendnrite model is exactly the same as the one used before.

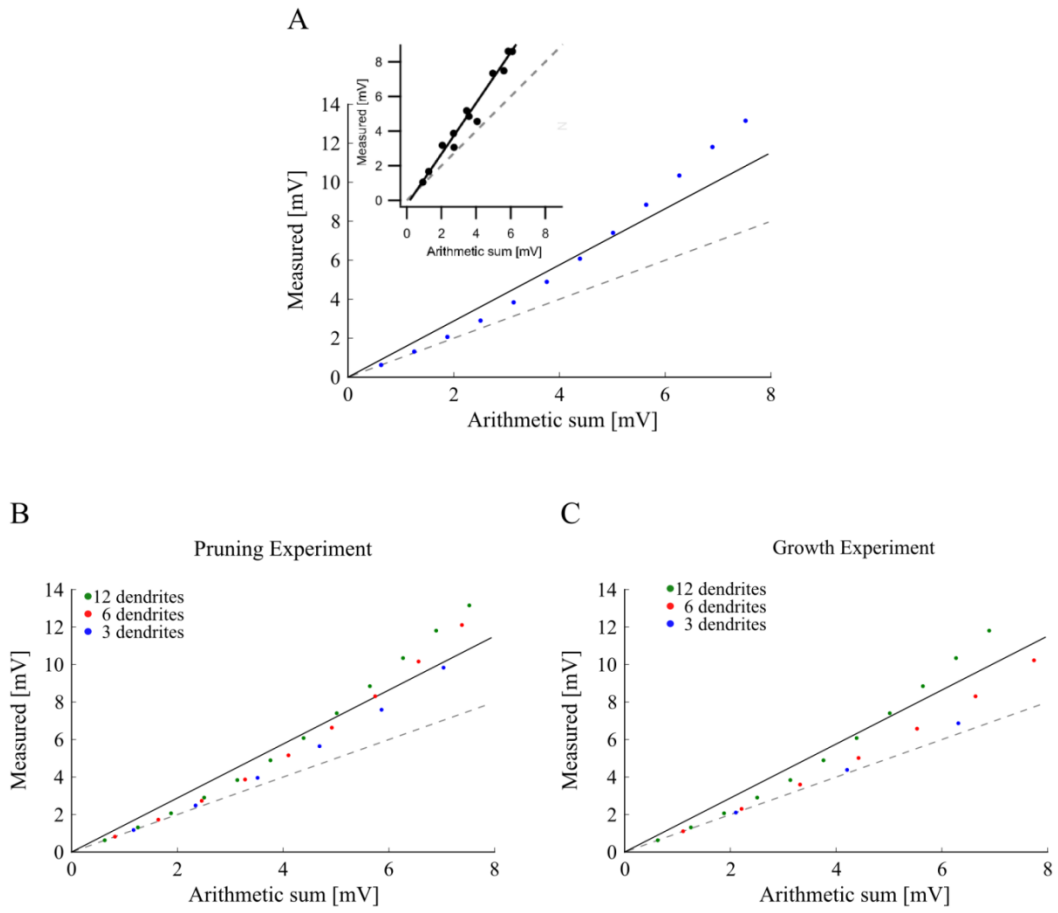

Figure 8. Measured EPSP - Arithmetic sum of somatic voltage relationship for GCs in the control, pruning and growth conditions.

The y-axis represents the measured somatic EPSP of each neuron in mV, while the x-axis shows the linear summation of somatic voltage in mV. The dashed gray line represents the linear summation ($y = x$), while the solid black line the gain ($y = 1.44x$) according to (Krueppel et al., 2011). **A.** The 12-dendrite GC control model. The curve is in line with experimental data as shown in the inset adopted from (Krueppel et al., 2011). **B.** Curves for 12-(green), 6-(red) and 3-dendrite (blue) GC models in the pruning experiment. **C.** Curves for 12-(green), 6-(red) and 3-dendrite (blue) GC models in the growth experiment.

4.2.1.2 Leakage channel density, Somatic dimensions, Synaptic weights

To study the effect of various parameters on pattern separation, we have chosen to modify the leakage channel conductance and the size of the GC soma in order to match the input resistance across the different GC models. As a result, we have modified the g_{leak} parameter of the GC model and the soma dimensions (length, diameter). Finally, to tune the models by their sparsity level, we have further changed

the aforementioned parameters, as well as the synaptic strength from the input afferents to the GC dendrites. In the model, this change is translated in a reduction in the corresponding synaptic weights. The corresponding input-output curves of the aforementioned models are shown in Figure 9.

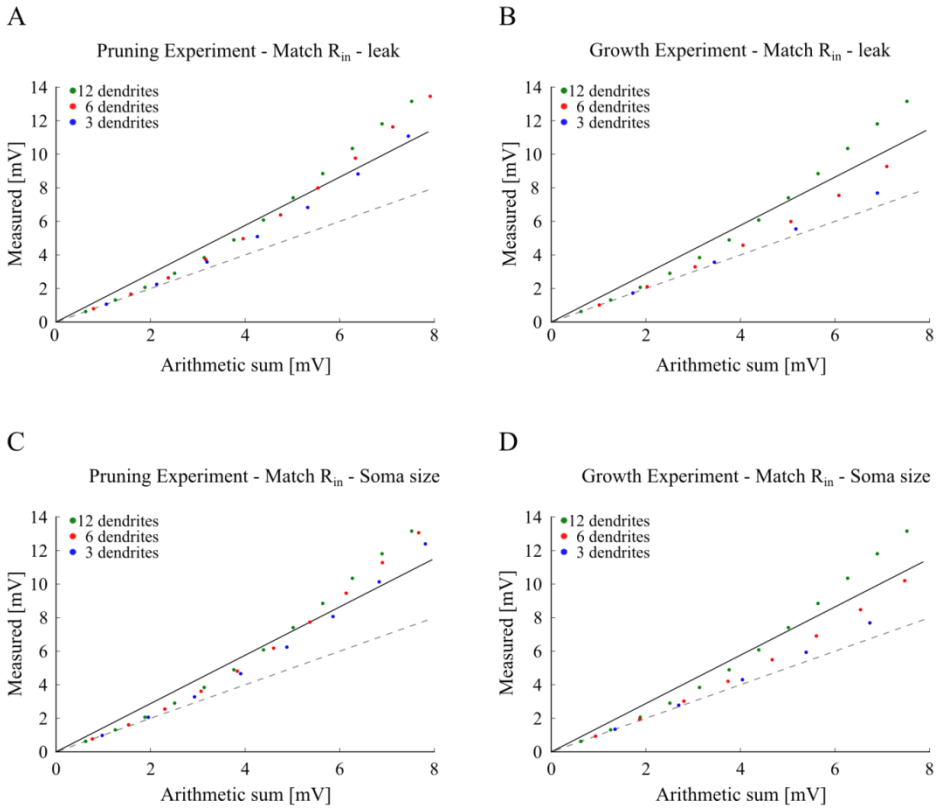

Figure 9. Measured EPSP-Arithmetic sum of somatic voltage relationship of GCs after correcting for the Input Resistance.
The y-axis represents the measured somatic EPSP of each neuron in mV, while x-axis shows the linear summation of somatic voltage in mV. The dashed gray line represents the linear summation (y = x), while the solid black line the linear summation with gain (y = 1.44x) according to (Krueppel et al., 2011). **A.** Curves for 12-(green), 6-(red) and 3-dendrite (blue) GC models used in the pruning experiment after matching R_{in} by modifying the "leak" conductance. **B.** Curves for 12-(green), 6-(red) and 3-dendrite (blue) GC models used in the growth experiment after matching R_{in} by modifying the "leak" conductance. **C.** Curves for 12- (green), 6- (red) and 3-dendrite (blue) GC models used in the pruning experiment after matching R_{in} by modifying the soma size. **D.** Curves for 12-(green), 6-(red) and 3-dendrite (blue) GC models used in the growth experiment after matching R_{in} by modifying the soma size.

4.2.2 Pattern separation metrics

Generally, a network performs pattern separation whenever the distance between two input patterns is lower that the distance between the corresponding output patterns. In this project, the input patterns are presented as the activity along the 400 PP afferents. Each input pattern has 40 active PP afferents (10% input density), an amount of which are common between two patterns; hence the two patterns are overlapping. In order to quantify the pattern separation efficiency we used two custom metrics denoted by f_1 ('population distance') and f_2 ('rate distance'), respectively.

4.2.2.1 Population-distance metric

The population-distance metric calculates the distance between two patterns based on differences among neurons that are active (Figure 7B). Active cell is considered every GC that fires at least one spike during stimulus presentation (Myers and Scharfman, 2009), thus the output patterns correspond to the GC activity. The population-distance metric is given from the equation below:

$$f_{1(i,o)} = \frac{HD_{i,o}}{2\left(1 - s_{i,o}\right)N_{i,o}}$$

where the *i* and *o* subscripts denote the calculation in the input and output patterns, respectively, *HD* the Hamming Distance between two patterns, defined as the number of neurons found in different states (active/inactive) between patterns, *s* the sparsity (i.e., the ratio of inactive-silent neurons to all neurons), and *N* denotes the number of neurons. The factor of 2 in the denominator is in order to limit the metric value to zero. The network is said to perform pattern separation whenever the input distance is lower than that in the output, i.e., $f_{1,i} < f_{1,o}$. Thus far, the metrics used to quantify pattern separation take into account only the hamming distance between two patterns. However, as the active number within each pattern is different (1-5% GCs active), we disengage the dependency on sparsity by dividing the HD with the number of neurons that are active.

4.2.2.2 Rate-distance metric

Whereas the f_1 metric quantifies the distance between two binary vectors containing active and non-active neurons ('population distance'), we have defined an additional metric, denoted by f_2, which quantifies the distance in the firing rates of common neurons that encode two patterns by using their firing rates ('rate distance'). The f_2 metric is calculated by dividing, for each neuron that is active in both patterns, its mean firing rate given one stimulus (control stimulus, A) by its mean firing rate given a stronger stimulus (B), and averaging these ratios across the population of input and output neurons, respectively (Leutgeb et al., 2004), taken into account only the neurons that are active in both patterns. We subtract this ratio from one in order to convert the 'rate similarity' into a 'rate distance'. The corresponding equation is given below:

$$f_2 = 1 - \frac{1}{N_c}\sum_{j=1}^{N_c}\frac{r_{B,j} - \min_B r_B}{r_{A,j} - \min_A r_A}$$

where N_c denotes the number of common neurons that are active for both inputs (A and B), and r denotes the firing rate of j_{th} neuron using input A and B, respectively. Here, B represents the low firing frequency input, while A the high frequency input (Figure 7C). We subtract the global minimum firing rate of GCs found in all trials in order to normalize the dynamic range of firing rates. For this experiment, the population of active EC neurons in each pair of inputs was identical. The network performs pattern separation if the input 'rate distance' is smaller than the corresponding distance in the output, i.e., $f_{2(input)} < f_{2(output)}$.

4.2.3 Stimulus and Input protocol

For simplicity, we have implemented the input to the DG coming from EC LII via performant pathway as independent Poisson spike trains. The input consists of 400 of those spike trains with mean firing rate of 40 Hz, which is in line with experimental evidence (Hafting et al). In line with experimental evidence, for every given stimulus only a 10% of input neurons are active. To study pattern separation we have constructed a variety of different input patterns and the active neurons are uniformly random chosen.

First, we have constructed four groups of input pattern pairs, with different degrees of similarity and calculated the input and the corresponding output population distances for each group independently. We have constructed a variety of input patterns with input density 10% (i.e., 40 active neurons) and consequently, four additional input patterns were built with 40 active neurons, 8, 16, 24, and 32 of which are common between patterns, respectively, which, in turn, corresponds to $f_{1(input)}$ = 0.4, 0.3, 0.2, and 0.1. The reasoning behind this approach is to examine highly overlapping patterns, as well as less similar ones. Thus, each trial was composed of two simulations using two input patterns within each group.

For the rate-based metric, instead of using the four additional patterns with different degrees of similarity, we have used the same input patterns with mean firing rate of 40 Hz (input B), and a second set of stronger input patterns with mean firing rate of 50 Hz (input A) consists of the same active neurons. Specifically, we have built pairs of input patterns with the same active neurons but with different firing rate.

4.2.4 Simulations and Statistical Analysis

For each trial, the network was simulated for 850 milliseconds (ms). The first 300 ms were simulated in order for the network to reach its stable state, so they were excluded from the analysis. The input onset was at 300 ms and the stimulus was applied for 500 ms. The last 50 ms were simulated in order for the network to reach again its steady state and they were excluded from the analysis as well. The time step for all simulations was set to 0.1 ms. We have used 50 trials per pattern separation protocol and then, the results were then averaged across all trials. Unless otherwise mention, the error bars are given as the standard error of the mean.

The data analysis and the figures describing the results were made using custom made programs in python 2.7.10™ (www.python.org) while the statistical analysis was made using the R3.3.1 programming language (https://www.r-project.org). We used the two-sided, two-sample Wilcoxon signed-rank test for the pattern separation efficiency comparisons and the two-sided, two-sample Kolmogorov–Smirnov test

(K–S test) to compare the GC activity probability density functions (Neuhauser, 2011). The model is available for download in Model DB (accession number: 206372) at http://dendrites.gr/en/publications-8/software-23.

4.3 Results

4.3.1 Understanding the role of inhibition in pattern separation

The GCs receive inhibition directly, via basket and HIPP cells, and indirectly via the MC to BC connection. The first step was to validate our network against experimental evidence, and to match the most critical parameter which is the sparsity of GCs activity. Therefore, we tune model parameters in order to have 5% of active GCs under control conditions. It is known that inhibition mediates sparsity and that the net effect of MCs is in inhibition. Thus, after removal of BCs the model has lost its ability to perform pattern separation as an almost 30% of GCs responded strongly to any stimulus. These findings are also in line with experimental evidence reporting increased memory interference under conditions of reduced BC activity in hippocampus (Engin et al., 2015).

Since MCs have also been suggested to control the excitability of DG granule cells (Jinde et al., 2013), we simulated a complete MC-loss lesion (Figure 10A) as per (Ratzliff et al., 2004). This manipulation led to an increase in the proportion of active GCs for all input patterns tested (Figure 10B and D), and a decrease in pattern separation efficiency, measured both with the population-based ($p < 0.001$) and rate-based metric ($p < 0.01$) (Figure 10C and E). Importantly, for the population coding experiment, the mean GC firing frequency increased from 3.5 to 4.82 Hz, while for the rate-based coding experiment from 3.75 to 4.94 Hz and from 5.24 to 8.07 Hz for 40 and 50 Hz inputs, respectively. These findings are in line with the experimental data of (Ratzliff et al., 2004) where MC-loss did not lead to an over-excitation of GCs.

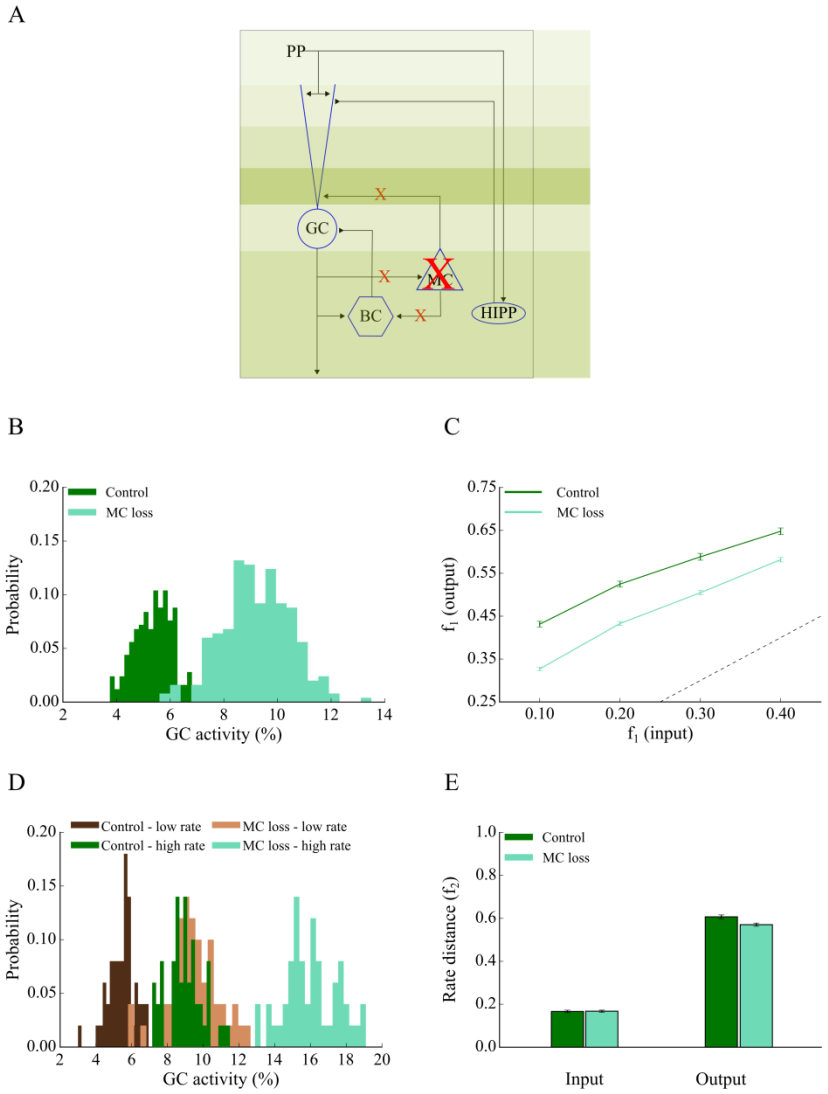

Figure 10. Complete mossy cell removal reduces pattern separation efficiency in the DG network.

A. Schematic representation of the 12-dendrite DG network with MC loss denoted by the red crosses. **B.** The corresponding probability density functions of GC activity in response to 40 Hz input for the control (dark green) and MC-loss conditions (light green). The mean activity percentage is 5 and 9% for the control and MC-loss networks, respectively. **C.** Input/output population distances (f_1) for the control (dark green) and MC-loss (light green) networks estimated using input patterns with increasing similarity. The dashed line denotes the limit above which the model performs pattern separation. MC removal decreases pattern separation efficiency for all input patterns tested. **D.** Probability density functions of GC activity using control and MC-loss models presented with two input patterns that differ only in their firing rates. Shades of green represent the high frequency input (50 Hz), while shades of brown represent the low frequency input (40 Hz). Dark and light shades represent the control and MC-loss condition, respectively. **E.** Input/output rate distances (f_2) for the control (dark green) and MC-loss (light green) networks estimated using two input patterns with different firing frequencies, 40 and 50 Hz, respectively. MC deletion slightly reduces the efficiency of pattern separation.

Taken together, the proposed DG network model exhibits single-neuron response properties that are in line with experimental data, implements a connectivity profile that relies on experimental observations, exhibits robust pattern separation, and finally, replicates experimental data about the role of BCs and MCs in the examined computational task. The aforementioned features support the biological plausibility of the network which is next used to investigate the role of GC dendrites to pattern separation.

4.3.2 Dendrites of granule cells and pattern separation

4.3.2.1 Dendritic pruning

The crucial question in this project is whether and how dendrites may affect the pattern separation. To address this question we have started by studying whether the number of dendrites correlates with pattern separation performance as we prune the GC (sister) branches from 12 (control) to six and three (Figure 11A). Thus, we have used three different GC models as described in Chapter 3. To assess the effect of dendritic number, we kept all other parameters (such as the path length, the dendritic diameter in the IML, MML, and OML layers, membrane capacitance, "leak" conductance, number of activated synapses, and input firing rates) of the two additional GC models identical to those of the control. While the absolute number of activated synapses remained the same (both excitatory and inhibitory), their spatial distribution on terminal dendrites (afferents from EC and HIPP cells) was different in the three GC models. Interestingly, pattern separation of pairs of inputs with increasing similarity (measured either by population distances, Figure 11C, or by rate distances, Figure 11E) was successfully performed in the control as well as both pruned models for all pairs of inputs tested. Nonetheless, the efficiency of pattern separation correlated with the number of dendrites in GCs (Figure 11C and E), with the 12-dendrite GC model achieving the best performance for both population ($p < 0.001$) and rate based ($p < 0.001$) coding schemes.

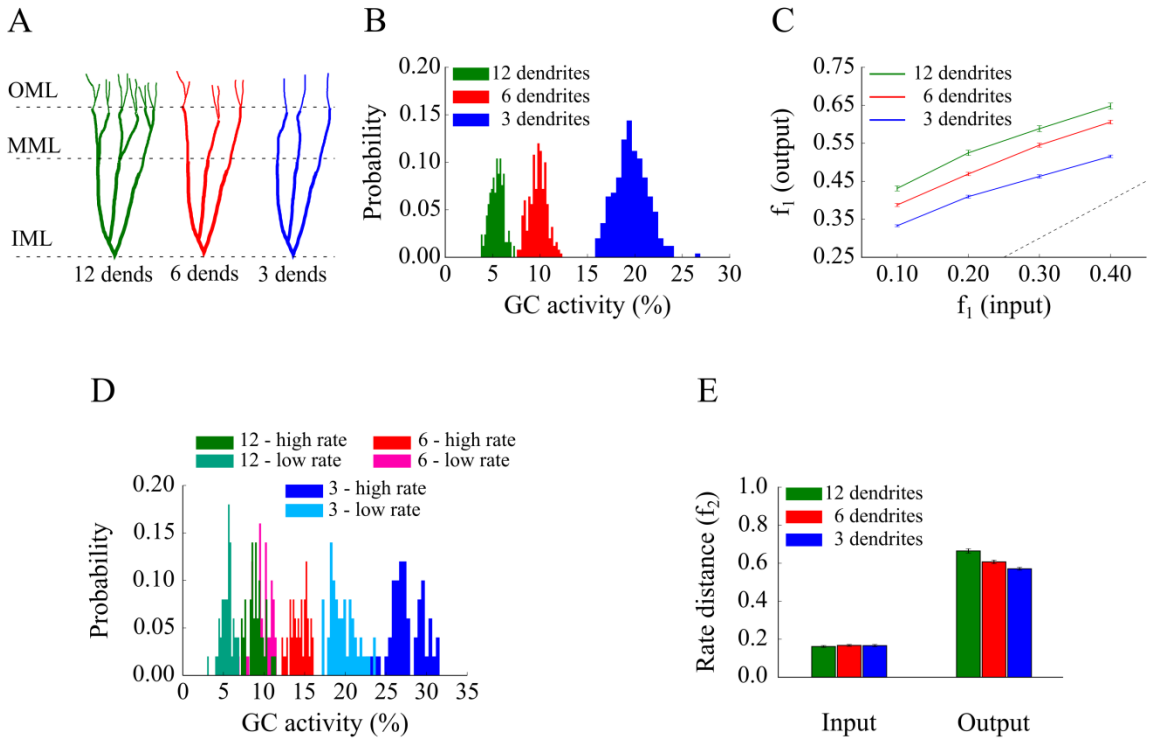

Figure 11**.** Effect of GC dendrite pruning on pattern separation.

A. A schematic drawing of the three GC models with three, six and 12 dendrites. **B.** Corresponding probability density functions of GC activity for the three GC models in response to a single input pattern at 40 Hz. The mean activity is inversely analogous to the number/length of dendrites: as dendrites pruned, the GC population becomes less sparse, i.e., more GCs are active. **C.** Input/output population distances (f_1), for the 12-dendrite (green), 6-dendrite (red), and 3-dendrite (red) GC models in response to the presentation of two overlapping input patterns at 40 Hz, with different degrees of overlap, as depicted in Figure 7B. The dashed line denotes the limit above which the model performs pattern separation. Performance drops with the pruning of dendrites. **D.** Probability density functions of GC activity for the three GC models in response to presentation of two input patters with different firing rates (low rate 40 Hz, high rate 50 Hz), as depicted in Figure 7C. GC activity decreases with the number of dendrites and increases with the input firing rate. **E.** Input/output rate distances (i.e., f_2) for the three models. The number of GC dendrites is analogous to the pattern separation performance.

These findings are better understood by looking at the sparsity levels exhibited by the three GC network models. As shown in Figure 11B, the percentage of active GCs for the population-based experiment increased substantially when the number of dendrites was reduced. It rose from ~5%, to ~10 and ~20%, for GC model cells with 12, 6 and 3 dendrites, respectively. These differences in activity distributions

were statistically significant ($p < 0.001$). The same differences are found using the rate code approach. Input patterns with high firing rates induced lower sparsity levels in the 12-dendrite GC model, followed by the 6- dendrite model and then the 3-dendrite model ($p < 0.001$). These data suggest that high levels of sparsity (namely low levels of GC activity) and thus, pattern separation efficiency in the network model are a direct consequence of having multiple and more complex dendrites and therefore, propose that dendrites may contribute to pattern separation in a positive manner through their mediation of sparsity; as the number of dendrites is reduced the pattern separation efficiency significantly drops.

4.3.2.2 Dendritic growth

To further test whether the presence of dendrites helps pattern separation by increasing sparsity, we also simulated the opposite process, namely the dendritic dendrites. We have built two additional GC models containing three, six and 12 dendrites with shapes that roughly mimic the stages of dendritic growth (Figure 12A): starting with a GC model consisting of three short and thick dendritic compartments and adding a branch point with two thinner sister branches at each terminal dendrite we end up with a 12-dendrite model which is identical with our control one. Notably, the number, length, and mean diameter of dendrites differ between the three models during this experiment.

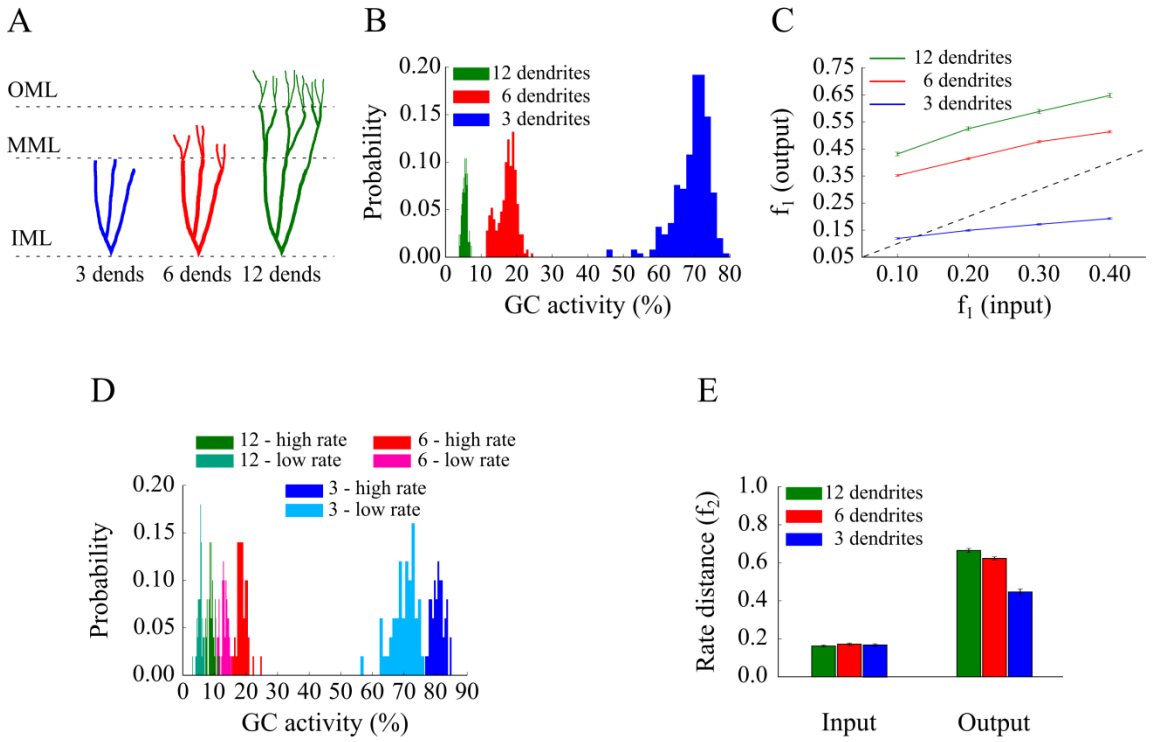

Figure 12. Effect of GC dendrite growth on pattern separation.

A. A schematic drawing of the three GC models with three, six and 12 dendrites. B. Corresponding probability density functions of GC activity for the three GC models in response to a single input pattern at 40 Hz. The mean activity is inversely analogous to the number/length of dendrites: as dendrites grow, the GC population becomes sparser, i.e., fewer GCs are active. C. Input/output population distances (f1), for the 3-dendrite (blue), 6-dendrite (red), and 12-dendrite (green) GC models in response to the presentation of two overlapping input patterns at 40 Hz, with different degrees of overlap, as depicted in Figure 7B. The dashed line denotes the limit above which the model performs pattern separation. Performance improves with the growth of dendrites. D. Probability density functions of GC activity for the three GC models in response to presentation of two input patters with different firing rates (low rate 40 Hz, high rate 50 Hz), as depicted in Figure 7C. GC activity decreases with the number of dendrites and increases with the input firing rate. E. Input/output rate distances (i.e., f2) for the three models. The number of GC dendrites is again analogs to the pattern separation performance.

In line with the findings of the pruning experiment, the percentage of active GCs declined as the number of dendrites increased (Figure 12B and D). The average GC activity for the population-coding experiment started at ~70% when 3-dendrite model used, dropped to ~28% for the network with 6-dendrite GC model and to ~5% for the 12-dendrite GC model. Similar differences in GC sparsity were seen in the rate-based

experiment (Fig. 5D). In both cases, the 3-dendrite model exhibited much higher activity levels than the ones seen in the pruning experiment (Figure 11B and D), primarily because of additional alterations in dendritic length and diameter. Moreover, pattern separation measured by the population metric was completely impaired in the 3-dendrite model (Figure 12C, blue line falls below the diagonal) while performance based on rate coding remained above the limit (Figure 12E, blue bar). Pattern separation was successfully performed in the 6-dendrite model albeit with lower efficiency compared to the 12-dendrite model, as evaluated both with the population and rate coding schemes. Yet again, the network containing the 12-dendrite model performs better comparing with 6- and 3-dendnrite models ($p < 0.001$). Taken together, the "pruning" and "growth" simulations suggest a strong link between pattern separation efficiency and GC population sparsity (Deng et al., 2010; Aimone et al., 2011) and predict that dendrites may serve as a mechanism for increasing the sparsity of the GC population (reducing number of active GCs) which in turn enhances pattern separation.

4.3.3 Controlling sparsity with non-dendritic mechanisms

The above simulations predict that dendrites can be sufficient for mediating sparsity, which in turn enhances pattern separation. We next ask whether they are necessary for this task, as it is possible that a GC neuron can counteract the decrease in sparsity induced by having fewer and/or shorter dendrites through alternative mechanisms. First, we evaluated the effect of input resistance differences among the various GC models on sparsity and pattern separation efficiency. A possible explanation of the above findings is that a GC model with a small dendritic tree has increased input resistance which in turn leads to higher excitability and thus, to decreased sparsity. We thus corrected the input resistance in the 6- and 3-dendrite models to match the one in the 12-dendrite model (at the soma) by modifying (a) the "leak" channel conductance (g_{leak}) or (b) the size of the somatic compartments (see Chapter 3).

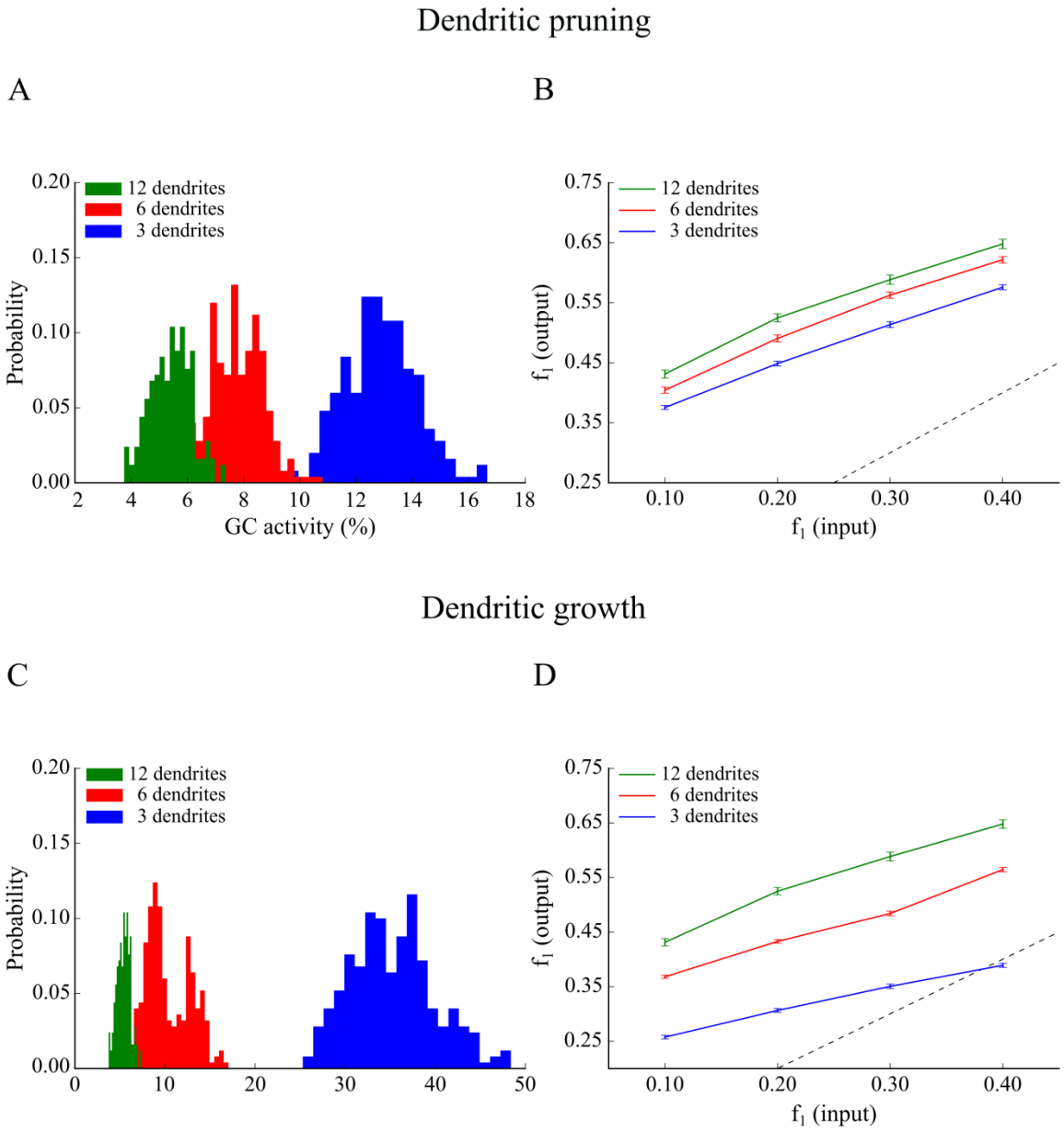

Figure 13. Effect of GC dendritic pruning (top panel) and growth (bottom panel) on pattern separation when the input resistance (R_{in}) is the same across models.

To match R_{in}, the leak conductance (g_{leak}) was increased by a factor of 1.695 and 1.230, in the 3- and 6-dendrite models, respectively. A. Corresponding probability density functions of GC activity for the three GC models in response to a single input pattern at 40 Hz. B. Input/output population distances (f1), for the 3-dendrite (blue), 6-dendrite (red), and 12-dendrite (green) GC models in response to the presentation of two overlapping input patterns at 40 Hz as depicted in Figure 7B. The dashed line denotes the limit above which the model performs pattern separation. Performance improves with the number of dendrites. C. The same as in A for the growth experiment. While distributions move closer to one another, the inverse relationship between dendritic number and mean sparsity is preserved. D. Same as in B for the growth experiment. Pattern separation efficiency still

correlates with the number of dendrites. Figure 14 depicts the corresponding pattern separation efficiency based on 'rate distance'.

Specifically, for the pruning models, g_{leak} increased by 1.230 and 1.635 times for the 6- and 3-dendrite models while for the growth models, these numbers were 1.596 and 2.438, respectively. Figure 13 shows the outcome of this correction for both pruning (Figure 13A and B) and growth (Figure 13C and D) cases. As evident from the figure, correcting the input resistance by increasing the "leak" conductance in the pruning case, reduced but did not eliminate differences in sparsity (Figure 13A). Similar findings were seen in the growth case; both for the sparsity (Figure 13C) and pattern separation efficiency (Figure 13D) ($p < 0.001$). Both sparsity and pattern separation efficiency were highest in the 12-dendrite, followed by the 6-dendrite and the 3-dendrite models. The same was seen when using the rate-based distance metric to evaluate sparsity and pattern separation (Figure 14). In all cases, differences were more pronounced in the growth compared to the pruning case, in line with the findings of Figure 11 and Figure 12.

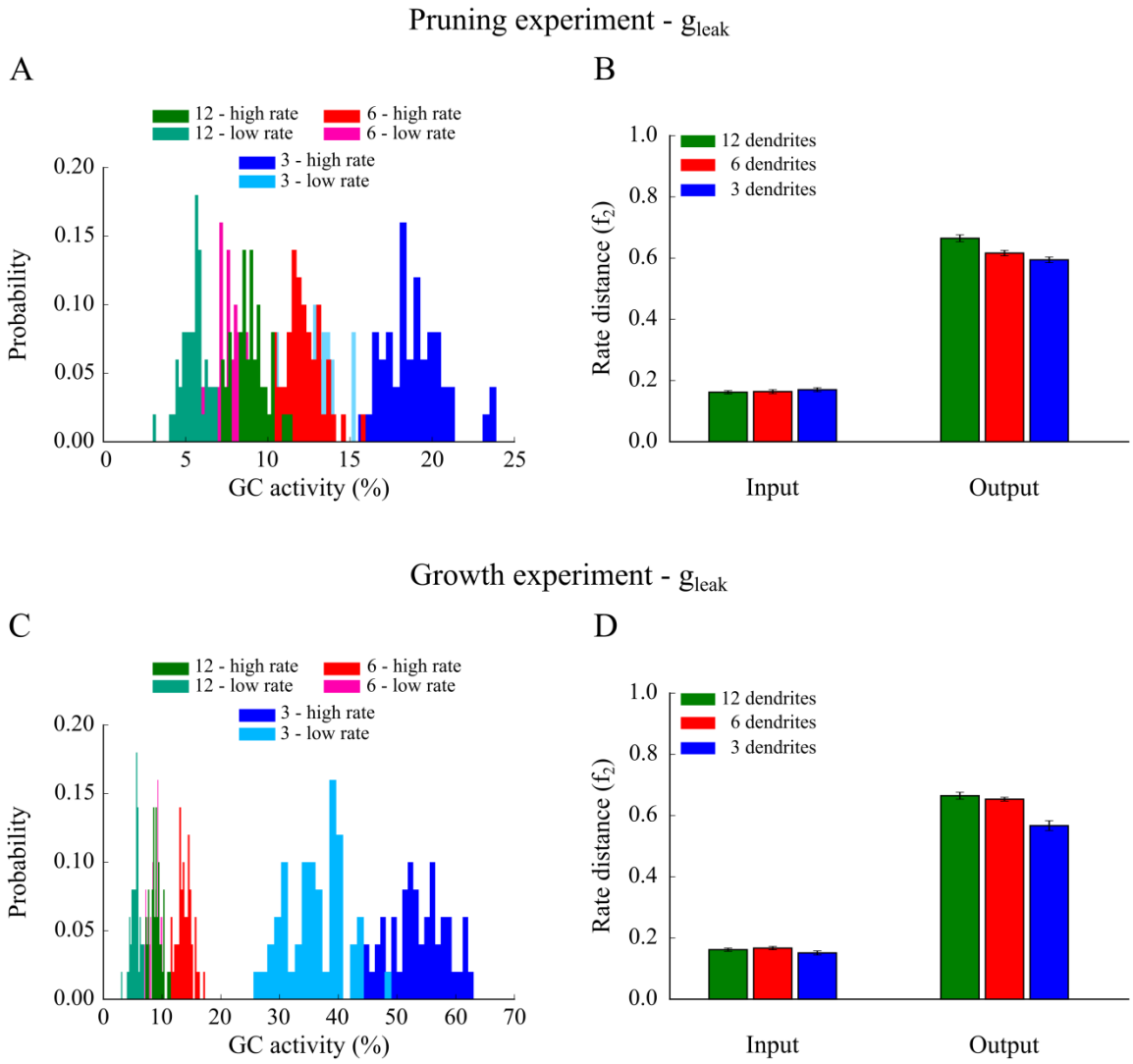

Figure 14. Effect of GC dendritic pruning and growth after matching (modification) on pattern separation estimated using the 'rate distance'.

A. Probability density functions of GC activity for the three GC models (pruning experiment) in response to presentation of two input patterns with different firing rates (low rate 40 Hz, high rate 50 Hz), as depicted in Figure 7C. GC activity increases with the number of dendrites and the input firing rate. B. Input / Output rate distances (i.e., f_2) for the three models. The number of GC dendrites is again analogous to the pattern separation efficiency. C. Probability density functions of GC activity for the three GC models (growth experiment) in response to presentation of two input patterns with different firing rates (low rate = 40 Hz, high rate = 50 Hz), as depicted in Figure 7C. GC activity decreases with the number of dendrites and the input firing rate. D. Input / Output rate distances (i.e., f_2) for the three models. Pattern separation efficiency is significantly worst only for the 3-dendrite model.

Similar results were obtained when correcting the input resistance by increasing the dimensions of the somatic compartment. For the pruning models, the soma increased by a factor of 1.278 and 1.527 in the 6- and 3-dendrite models, respectively while for the growth models, these factors were 1.513 and 1.746, respectively. As shown in Figure 15 (A, B), for the pruning case, differences in sparsity and pattern separation efficiency among corrected models decreased significantly but were not eliminated. Similar findings were seen in the growth case Figure 15 (C, D), both for the sparsity and pattern separation efficiency ($p < 0.001$). Both sparsity and pattern separation efficiency remained highest in the 12-dendrite, followed by the 6-dendrite and the 3-dendrite models.

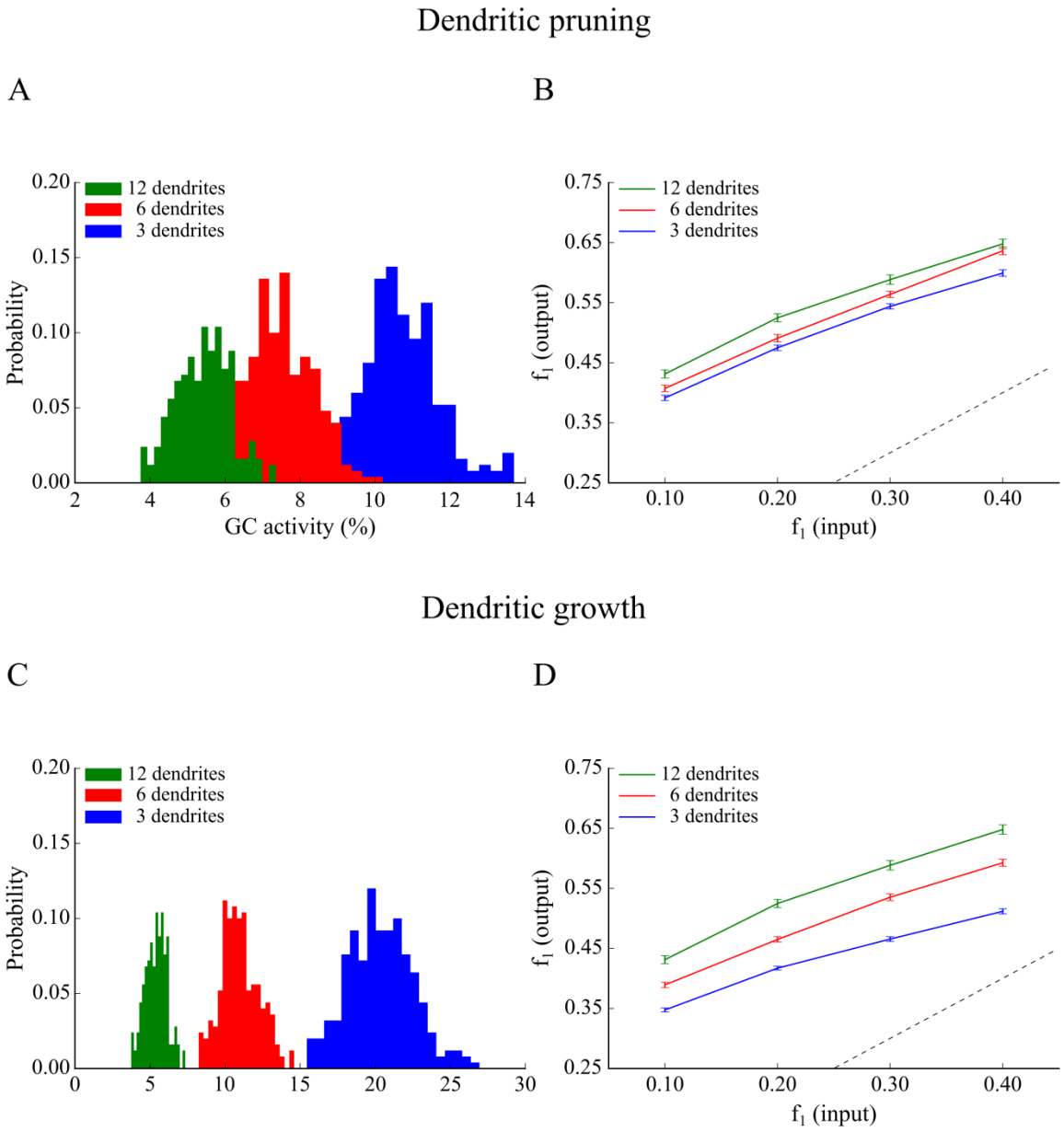

Figure 15. Effect of GC dendritic pruning (top panel) and growth (bottom panel) on pattern separation when matching the input resistance (R_{in}) via increasing the somatic size.

The neuronal soma of the 3- and 6-dendrite models was increased by a factor of 1.527 and 1.278, respectively. **A.** Corresponding probability density functions in response to a single input pattern at 40 Hz. **B.** Input/output population distances (f_1), for the 3-dendrite (blue), 6-dendrite (red), and 12- dendrite (green) GC models in response to the presentation of two overlapping input patterns at 40 Hz as depicted in Figure 7B. The dashed line denotes the limit above which the model performs pattern separation. Performance becomes similar yet statistically different among the three corrected models and remains analogous to the number of dendrites. **C.** Same as in A, for the growth experiment. The inverse relationship between dendritic number and mean sparsity is

preserved. **D.** Same as in B, for the growth experiment. Pattern separation efficiency remains different and analogs to the number of dendrites.

Similar findings were obtained when using the rate-based distance metric to assess pattern separation (Figure 16). Note that correcting the input resistance via increasing the somatic compartment is more effective than increasing the leak conductance, as both C_m and g_{leak} increase proportionally, keeping the membrane time constant identical across model cells.

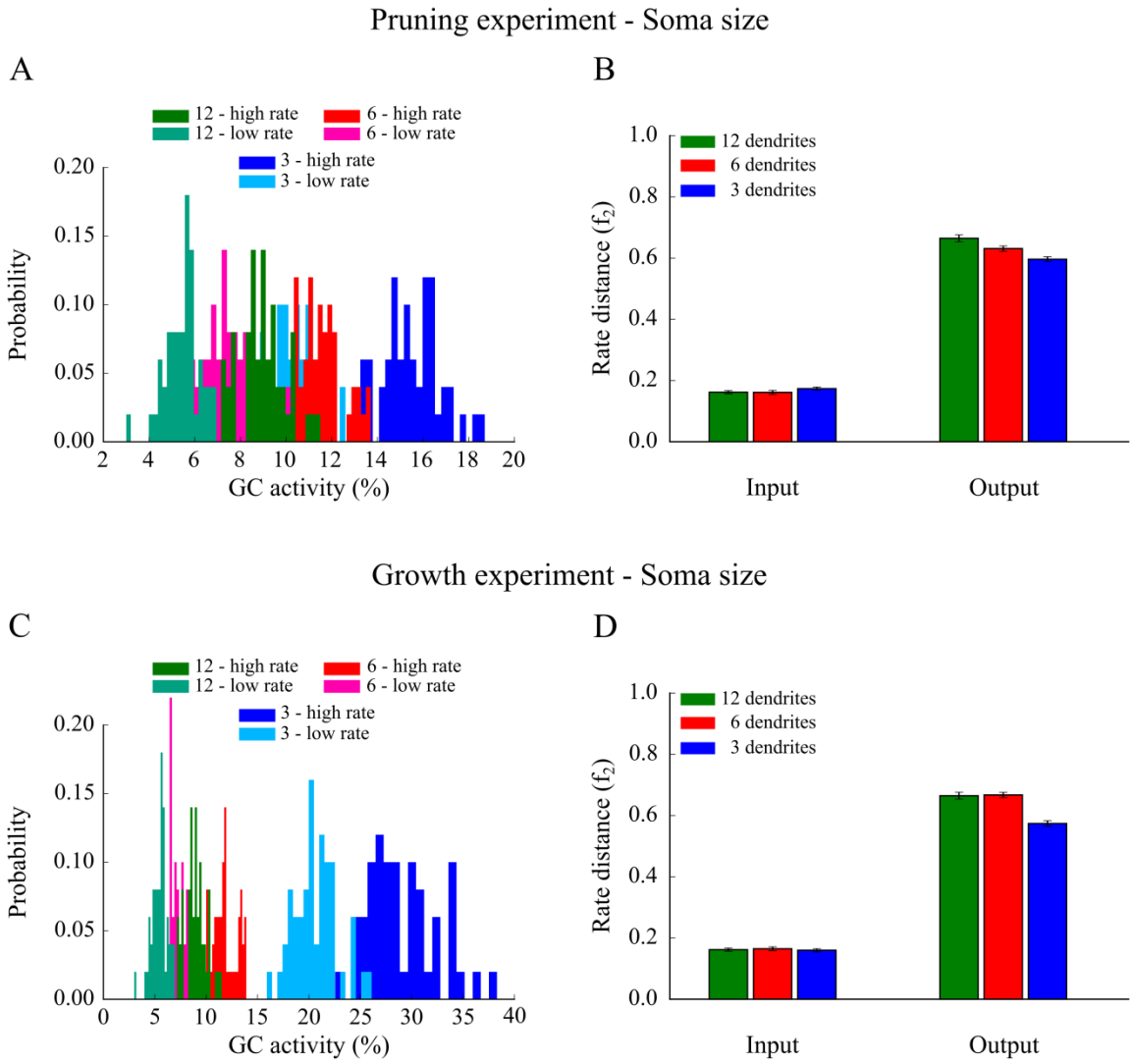

Figure 16. Effect of GC dendritic pruning and growth after matching (soma size modification) on pattern separation estimated using the 'rate distance'.

A. Probability density functions of GC sparsity for the three GC models (pruning experiment) in response to presentation of two input patterns with different firing rates (low rate 40 Hz, high rate 50 Hz), as depicted in Figure 7C. GC activity increases with the number of dendrites and the input firing rate. B. Input / Output rate distances (i.e., f_2) for the three models. The number of GC dendrites is again analogous to the pattern separation performance. C. Probability density functions of GC activity for the three GC models (growth experiment) in response to presentation of two input patterns with different firing rates (low rate = 40 Hz, high rate = 50 Hz), as depicted in Figure 7C. D. Input / Output rate distances (i.e., f_2) for the three models. Here, the 6- and 12-dendrite GC models have approximately the same output 'rate distance'; however the 3-dendrite model performs worst.

Overall, these simulations suggest that while the input resistance is a key determinant of GC neuron activity, it does not fully explain the differences in sparsity and pattern separation efficiency among models with three, six or 12 GC dendrites.

4.3.4 Sparsity is the key determinant of pattern separation

The question that arises naturally from the above findings is whether further manipulations of the leak conductance and/or somatic dimensions could match sparsity across all models. Moreover, would matching sparsity result in identical pattern separation efficiency, thus making sparsity the key determinant of pattern separation (O'Reilly and McClelland, 1994; Johnston et al., 2015)? To answer these questions we explored the effects of manipulating intrinsic (g_{leak} and somatic dimensions) as well as extrinsic (synaptic weight) mechanisms in the 3-, 6-, and 12-dendrite GC models. Due to the consistent nature of the previous results, the remaining simulations were performed using the pruning experiment configuration to generate the 3- and 6-dendrite GC models and the population-based metric to assess pattern separation. As shown in Figure 17Ai, increasing g_{leak} by a factor of 1.58 and 2.48, in the 6- and 3-dendrite GC models respectively, eliminated the differences in sparsity distributions compared to the control ($p>0.1$). The same was observed with respect to pattern separation efficiency (Figure 17Aii). All three models exhibited identical performance across all difficulty levels ($p>0.1$). Similarly, increasing the diameter and length of the somatic compartment in the 6- and 3-dendrite models by 1.480 and 1.870, respectively (Figure 17Bi) resulted in similar sparsity ($p>0.1$). Similarly, pattern separation efficiency was identical across all models and difficulty levels (Figure 17Bii) ($p>0.1$). It should be noted that the abovementioned sizes are not realistic for the soma of a GC neuron. Nevertheless, these findings highlight the key role of sparsity in controlling pattern separation efficiency, irrespectively of the number of GC dendrites. Moreover, these simulations predict that intrinsic mechanisms of GC neurons could potentially be used to correct for morphological alterations in order to control sparsity levels.

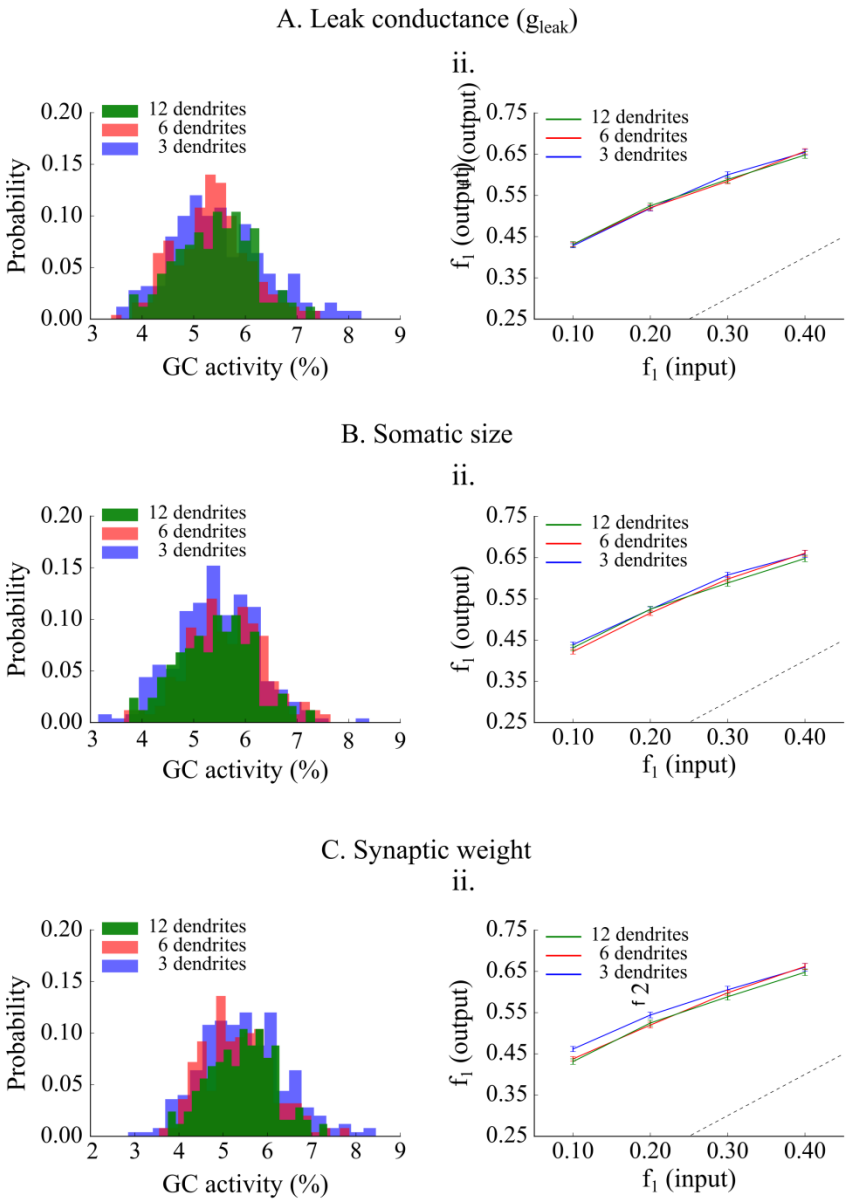

Figure 17. Effect of matching sparsity on pattern separation efficiency.

A. The "leak" conductance, g_{leak}, of the 6- and 3- dendrite GC models increases by a factor of 1.58 and 2.48, respectively. *Left panel:* Resulting GC activity distributions are not statistically different. *Right panel:* Networks with corrected GC models have identical performance. Differences in pattern separation using the population metric are not statistically significant. **B.** *Left panel:* GC activity distributions are matched by increasing the soma diameter and length of the 6- and 3-dendrite GC models by 1.48 and 1.87, respectively. *Right panel:* The network with corrected 3-dendrite GC models has a slightly smaller pattern separation efficiency compared to the other two probably because its activity distribution is wider. Generally the three models have very similar pattern separation performance. **C.** *Left panel:* GC activity distributions are matched decreasing the EC to GC synaptic weight from 1.00, to 0.75 and 0.56 in the 6-, and 3- dendrite models, respectively. *Right panel:* Pattern separation efficiency is statistically the same across all corrected GC models.

In sum, these simulations predict that sparsity is the key determinant of pattern separation efficiency. Sparsity of the GC neuronal population can be controlled via multiple mechanisms, including the growth of dendrites. Pruning of dendrites can be compensated by the growth of very large somata, a large increase in the leak channel conductance or a significant decrease in the strength of the EC input via synaptic weight changes (Figure 17C).

4.4 Discussion

4.4.1 What we have learnt from the model?

The goal of this study was to reveal whether and how dendrites of dentate principal cells can intervene in pattern separation via using a computational network. Towards this goal, we implemented a novel network model of the DG consisting of the four major neuronal types found in this subregion, namely Granule Cells, Mossy Cells, Basket Cells, and HIPP cells. GCs were modeled as two stage integrators by adding dendritic branches whose properties are loosely constrained by experimental data, both electrophysiological and anatomical ones. The rest of the neuronal types were simulated as exponential leaky integrate-and-fire neurons with adaptation. The proposed hybrid model of GC serves as a bridge between simplified point neuron models (Myers and Scharfman, 2009) and more detailed biophysical models (Santhakumar et al., 2005) of the DG. As such, it provides a biologically relevant and computationally efficient tool for the in depth exploration of different factors that possible have an important role during pattern separation task. The selective use of dendritic compartments only in GCs keeps the model complexity low while at the same time allowing the dissection of some basic GC dendritic mechanisms in pattern separation. To our knowledge this is the first DG network model of its kind.

Inhibition is known to control neuronal activity by increasing sparsity, as the number of active neurons is decreased for a given stimulus (Jung and McNaughton, 1993) therefore, enhancing pattern separation

(Aimone et al., 2011). In the presented model, inhibition is provided to the network both directly via BCs (somatic inhibition) and HIPP cells (dendritic inhibition) and indirectly through the MC circuitry. We find that MC loss, while increasing GC cell activity in line with the experimental data of (Ratzliff et al., 2002), does not lead to hyper-excitability yet we do predict a measurable and statistically significant drop on pattern separation efficiency.

To the extent of our knowledge, our model is the first to highlight a role of GC dendrites in pattern separation. This role is an indirect one and consequents from the inherent increase in sparsity of the GCs that is endowed by the presence of dendrites. Specifically, we show that the number of GC dendrites correlates positively with pattern separation efficiency due to the higher sparsity levels provided by having multiple and more complex dendrites. In our control model, higher sparsity arises from the requirement of having at least two dendrites simultaneously active in order to fire a GC model neuron. This emerged from the calibration of GC properties against experimental data, thus is considered biologically relevant. Consequently, GCs with large numbers of dendrites have a lower probability of activation given a fixed number of afferents, therefore increased network sparsity. We also predict that under conditions of dendritic pruning and/or early in the growth stages of GCs, high sparsity can be achieved with alternative mechanisms, both intrinsic (e.g., leak conductance, somatic dimensions) and extrinsic (e.g., synaptic weights) making dendrites a sufficient but not necessary condition for high pattern separation efficiency. These results support the hypothesis that sparsity in GC activity improves pattern separation (O'Reilly and McClelland, 1994) and provide a list of alternative mechanisms for controlling sparsity in the DG. It is likely that there exist other mechanisms that mediate and control sparsity, such as specific membrane channels and the geometry of the dendritic tree. However, the modifications of these mechanisms could not been explored by using the presented simplified computational network.

4.4.2 Implications to pathology

As part of the hippocampus, the DG is long hypothesized to play a key role in associative memories, and especially when those are related with events (Morris, 2006). Moreover, the hippocampal DG has been implicated as the subregion most sensitive to the effects of ageing (Small et al., 2004). While the CA1 subregion is directly associated with Alzheimer's Disease (AD) due to cell loss of pyramidal neurons, as demonstrated in humans (West et al., 2006), DG alterations have also been reported in patients with this disease (Scheff and Price, 2003), including changes in granular dendrites (Einstein et al., 1994). Specifically, the dendrites of GCs in AD patients appear shorter, with fewer branches and fewer spines than those of matched controls. Moreover, in AD patients the dendrites of GCs were reported to lose approximately 50% of their spines (Einstein et al., 1994). Our simulations show that the most important of the above-listed observations with respect to pattern separation would be the shortening of dendritic branches via the loss of branch points rather than the loss of side branches while maintaining the same dendritic path length. Total dendritic length of GCs was previously linked to AD, which in turn is aligned with the indication that patients with AD, who have extensive hippocampal and parahippocampal damage, lost their ability to encode information in distinct, orthogonal representations (Ally et al., 2013).

The DG is also associated with epileptogenesis in temporal lobe epilepsy (TLE) and hence, many computational models are used to investigate the effect of GC alterations in epilepsy (Tejada and Roque, 2014; Faghihi and Moustafa, 2015). Additionally, hilar cell loss has been reported in animal models after concussive head injury and also under TLE (Mathern et al., 1995). It remains unknown however, which specific hilar neurons are missing in animal models of TLE. As a result, there are currently three theories for TLE: i) the "dormant basket cell" hypothesis according to which the hyper-excitability in GC population is due to the loss of MCs which normally excite BCs providing with inhibition the GCs, ii) the "irritable mossy cell" hypothesis according to which surviving MCs hyper-excite GCs by sending uncontrolled excitation to granular proximal dendrites, and iii) the "MC loss-induced" sprouting hypothesis (mossy fiber sprouting) (Ratzliff et al., 2002). We showed that when MCs are completely

removed from the network, GCs exhibit increased activity (but not hyper-excitability) which should lead to pattern separation discrepancies. While our results are in agreement with the findings of (Ratzliff et al., 2002), more experiments need to be done to revolve this debatable issue.

4.4.3 Simplifications and future directions

Several simplifications were made in modeling the individual cells as well as in designing and building the DG network. First, we used simple point neurons in order to simulate the neuronal cells of DG. While these models could capture the average spiking properties of a given neuron, it remains vague how the geometrical characteristics of those neurons could affect their behavior. Another simplification concerns the effects of synaptic failure rates and receptor desensitization (Harney and Jones, 2002) in the DG, which were not included in the model.

An important aspect of DG function is the long-term synaptic plasticity, by which the connections from PP to GCs are adjusted. Previous DG models used a form of Hebbian learning that incorporates features of long-term potentiation and depression (Rolls, 2007). However, such a function is most likely to be relevant when stimuli are presented repetitively. Conversely, the current model is used to distinguish patterns presented in single instances and hence, plasticity is not presented in this model. Future work may address such issues along with including other types of interneurons such as the Molecular layer Perforant Path-associated (MOPP) and the Hilar Commissural-Associational pathway related (HICAP) cells, especially when more data on their intrinsic and connectivity properties become available.

Furthermore, GCs are among few cells that undergo adult neurogenesis (Eriksson, 2003; Aimone et al., 2010). In a recent study by (Nakashiba et al., 2012), the role of young GCs in pattern separation was investigated and it was concluded that new neurons are required for distinguishing similar incoming information. Since the presented model is used to study specific alterations of GCs and their effect on pattern separation, neurogenesis is not combined but would be taken into account in the future. Overall,

the aforementioned simplifications are unlikely to have a major effect on the basic conclusions about the contribution of morphological alterations of GC dendrites to pattern separation.

Chapter 5 Role of mossy cells in pattern separation

5.1 Preamble

Mossy cells in the hilus of the dentate gyrus constitute a major excitatory principal cell type in the mammalian hippocampus; however, it remains unknown how these cells behave in vivo and which is their role in specific memory processes. In this collaborative project the goal was to examine mossy cells in vivo, and to explain their contribution in context discrimination using a computational model. The project was done in collaboration with Losonczy lab (http://www.losonczylab.org/). Specifically, two-photon Ca^{2+} imaging has been used to monitor the activity of mossy cells in awake, behaving mice. We have found that mossy cells are significantly more active than dentate GCs in vivo, exhibit spatial tuning during head-fixed spatial navigation, and undergo robust remapping of their spatial representations in response to contextual manipulations. Our results provide a functional characterization of mossy cells in the behaving animal and demonstrate their active participation in spatial coding and contextual discrimination.

5.2 Materials & Methods

5.2.1 Overview of the experiments

The first part of this project was held in Losonczy lab, under supervision of Dr. Attila Losonczy. Here we describe briefly the experimental procedures with retrogradely-labeled MCs. Two-photon (2p) Ca^{2+} imaging has recently become available for optical recordings of the DG in vivo, comprising its

polymorphic layer (i.e., the hilus), during head-fixed behavioral experiments in mice (Danielson et al., 2016a).

We first sought to selectively label MCs with the genetically encoded Ca^{2+} indicator GCaMP6f by taking advantage of two characteristic anatomical features: MCs are immunoreactive for glutamate receptor type 2 or 3 (GluR2/3) (Ratzliff et al., 2004); and MCs comprise the predominant hilar cell population projecting to the contralateral DG (Frotscher et al., 1991; Ribak et al., 1985) (Figure 18). Therefore, we used a retrograde variant of recombinant adeno-associated virus (rAAV2-retro) (Tervo et al., 2016) expressing Cre-recombinase injected into the contralateral DG, in combination with a Cre-dependent rAAV expressing GCaMP6f injected ipsilaterally into the hilar imaging site, to label contralaterally projecting hilar neurons (Figure 18 A and B). This strategy labeled hilar but not CA3 neurons (Figure 18B), and in agreement with previous reports (Ratzliff et al., 2004), the vast majority of retrogradely labeled hilar neurons were immunopositive for GluR2/3; we therefore identified these cells as GluR2/3+, contralaterally projecting MCs (identified MCs – iMCs) (Figure 18B).

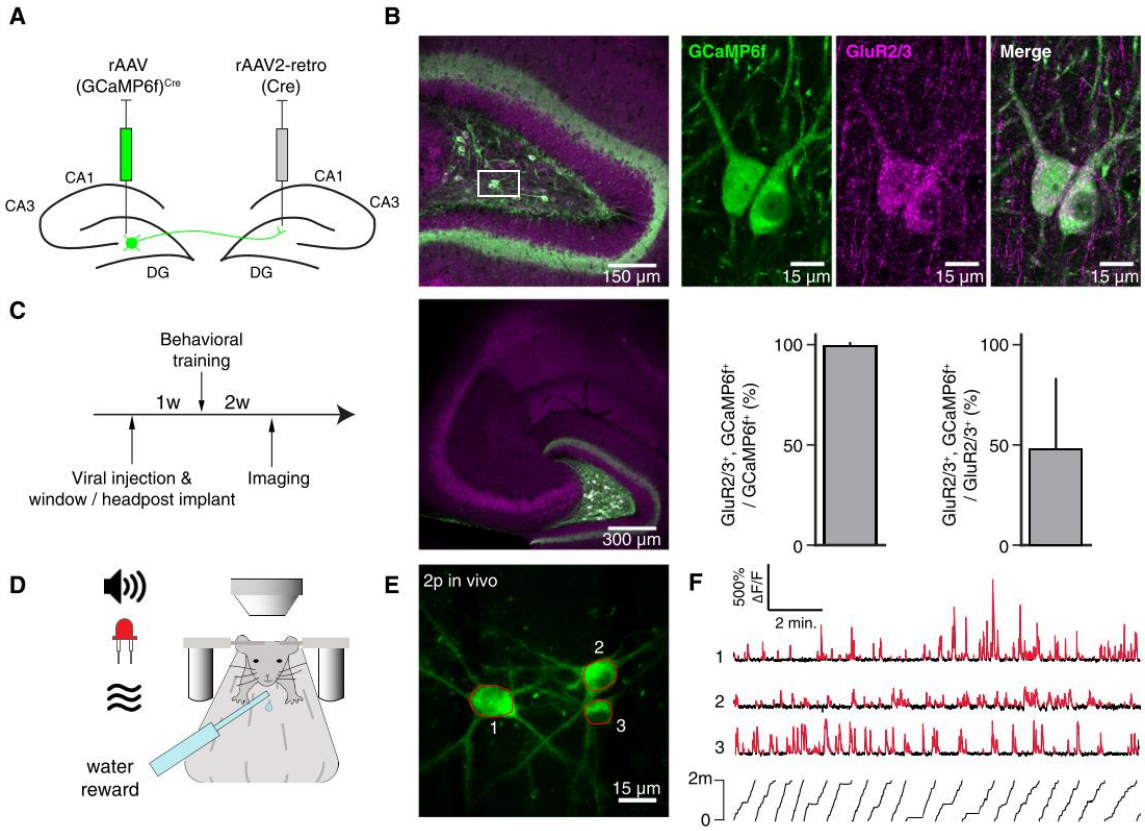

Figure 18. Imaging of identified Mossy Cells.

A. Viral labeling of mossy cells. **B.** Top: confocal image of a horizontal section through the hilus of the dorsal DG. GCaMP6f-expressing and GluR2/3-expressing cells are labeled green and magenta, respectively. The area indicated is shown at high resolution at right. Bottom left: low-magnification image through the hilus shows the lack of CA3 pyramidal cell labeling. Bottom right: nearly all GCaMP6f+ cells were also GluR2/3+, and approximately half of MCs were labeled with GCaMP6f. **C.** Experimental timeline. **D.** Schematic of the experimental apparatus. Head-fixed mice explored multisensory contexts comprised of the treadmill belt and other sensory stimuli (light, odor, sound). **E.** Max Z-projection image of a volume acquired in vivo of three GCaMP6f-expressing MCs. Example regions of interest in red. **F.** ΔF/F traces of three simultaneously recorded MCs. Significant transients in red ($p < 0.05$). The mouse's position on the treadmill is indicated below.

Following viral injection, mice were implanted with a chronic imaging window above the dorsal DG to provide the optical access necessary for visualizing the hilus (Figure 18C). To record Ca^{2+} activity from iMCs, we performed head-fixed 2p imaging as the animals (n = 6) performed a random foraging task by running for water reward on a treadmill across three sessions in different linear environments (Figure 18D–F) (Danielson et al., 2016a, 2016b). In total, we recorded from 57 iMCs in 6 animals. Signals were

extracted from the resulting binary masks, and significant Ca^{2+} transients were identified as in (Danielson et al, 2017).

5.2.2 Modification of the DG network (no dendrites)

Here we have modified the DG network (Chavlis et al., 2017) in order to make it simpler. Thus, we have replaced the hybrid GC model with a simple, point neuron with adaptation. The rest DG network is the same as the one presented before. For the purpose of the presented project, we have used the population-base coding scheme and hence, we have used the corresponding f_1 distance metric. For simplicity, two input patterns have been used with a medium overlap between them. Specifically, two patterns with distance equals to 0.20 have been built. Yet again, the results have been averaged across 100 trials. We used non-parametric Mann-Whitney U test for the pattern separation efficiency comparisons and the two-sided, two-sample Kolmogorov–Smirnov test (K–S test) to compare the GC activity probability density functions (Neuhäuser, 2011). The model is available for download from Model DB (accession number: 206397) and from Poirazi lab web page: http://dendrites.gr/.

5.3 Results

5.3.1 Activity of mossy cells in vivo

We first quantified the activity of iMCs during head-fixed navigation by measuring the rate of area under significant Ca^{2+} transients (AUC rate, Figure 19). In each session, nearly every cell fired at least one transient (and most fired many more), resulting in a high non-silent fraction (Figure 19B) across both recordings and behavioral states (running and non-running). Within this active population, the frequency of transients across all frames was 1.6 ± 1.2 transients/min, (mean ± std, n = 57 cells) and of large amplitude (79% ± 46% ΔF/F, mean ± std, n = 57 cells), resulting in a high AUC[1] rate within the non-silent population (Figure 19C). This finding was in stark contrast to the activity levels we previously

[1] AUC: area under the curve. Quantification of Ca^{2+} in a cell, which is extracted from a transient.

reported for GCs in our recent study (identical behavioral paradigm, Danielson et al., 2016a), and we therefore directly compared the activity of iMCs and GCs (pooling our adult-born and mature recordings). GCs fired transients at a very low frequency (0.08 ± 0.14 transients/min, mean ± std, n = 8,396 cells), and iMCs were thus considerably more active than GCs (Figure 19B and C).

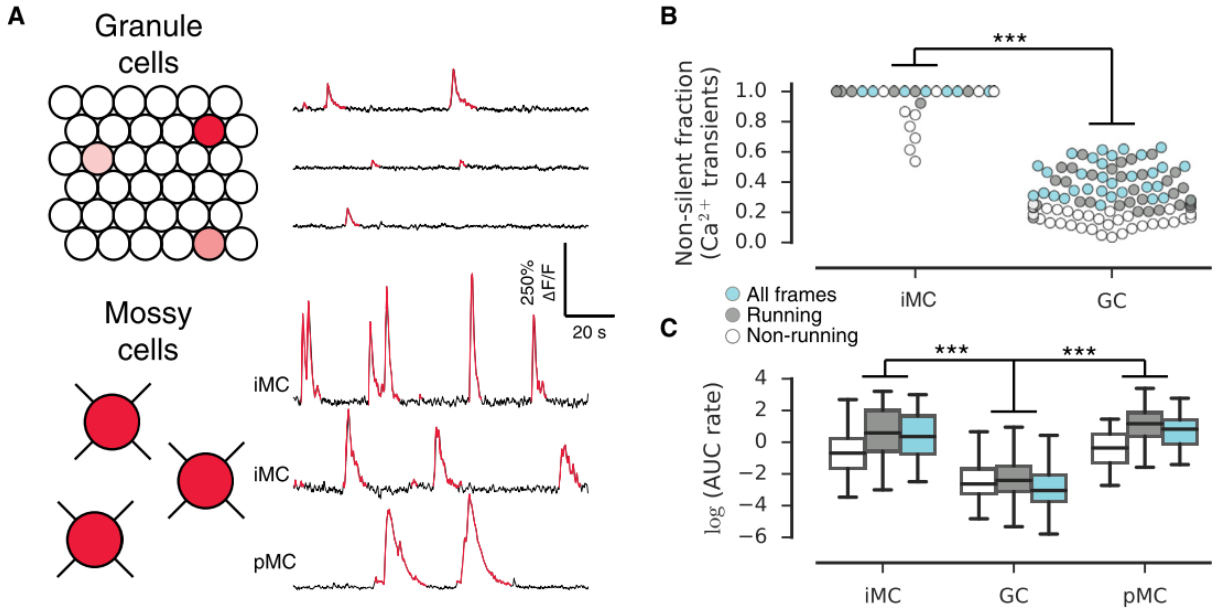

Figure 19. Activity of Mossy and Granule Cells.

A. Schematic of GC and MC activity. Only a small fraction of GCs are active (red shading) relative to MCs, and active MCs exhibit a significantly higher rate of Ca^{2+} activity than active GCs. Ca^{2+} traces from three example active GCs (right) and three example MCs (top). Significant Ca^{2+} transients ($p < 0.05$) are red. **B.** Activity was assessed by the rate of area under significant transients. The fraction of cells exhibiting non-zero activity is shown. Each circle represents a single recording session (with a minimum of three recorded cells) and is colored by the frames included in the analysis (non-running, running, and all frames). iMCs were significantly more active than GCs. pMCs were not included in this analysis. **C.** The activity of non-silent cells within each condition (non-running, running, all) is shown. Non-silent iMCs were significantly more active than non-silent GCs. Similarly, the activity of pMCs was significantly higher than GCs.

Because our GC and iMC recordings were acquired in different animals, we attempted to control for any possible differences between preparations by retrospectively analyzing our previous DG imaging dataset (Danielson et al., 2016a) to look for the presence of putative MCs (pMCs) in those recordings. The high spatial resolution of 2p imaging allows for the unambiguous separation of GCs from other cells lying in

hilus based on their location and distinct morphology. In our previous imaging study, GCaMP6f imaging was performed with broad labeling of all neuron types in the DG. In four of our fields of views (n = 4 animals), we could identify large, multipolar cells in the hilus, which were excluded from the original GC imaging dataset. In a subset of these hilar cells (n = 11 out of 20), we were able to detect large-amplitude transients with fast onset and exponential decay similar to the pattern observed in iMCs (Figure 19A, bottom). When we compared the activity rates between these simultaneously recorded hilar pMCs and non-silent GCs, we again found a highly significant difference in activity between these populations (Figure 19B and C).

5.3.2 Spatial tuning profiles of mossy cells

Because principal cells throughout the hippocampus are known to exhibit spatially selective, ‘‘place cell’’ firing (Hartley et al., 2014), we next sought to determine whether this feature extends to MCs. Thus, for each MC we calculated a spatial firing rate map and identified those cells whose distribution of Ca^{2+} transients contained statistically significant spatial information (Skaggs et al., 1993) (Figure 20A). In contrast to the very low place cell fraction among GCs (1.4% ± 1.0%, mean ± std, n = 32 recording sessions), we found a significant spatial coding population among MCs: 16% ± 20% (mean ± std, n = 18 recording sessions, Figure 20B) of our iMCs were classified as spatially tuned. Previous extracellular electrophysiological recordings suggested that GCs (Leutgeb et al., 2007), perhaps with preference toward adult-born GCs located closer to the hilus border (Neunuebel and Knierim, 2012), exhibit multiple firing fields. While the sparse activity in our imaging dataset precluded precise quantification of the number of place fields, we attempt ted to address this question by comparing the tuning specificity (Danielson et al., 2016a, 2016b) between the subpopulations of spatially tuned GCs and combined MCs (cMCs), in which the spatially tuned iMCs and pMCs were pooled to increase the statistical power. Finding both significant spatial information and low tuning specificity would indicate the presence of multiple firing fields. We found that the tuning specificity for spatially tuned cMCs was significantly

lower than for spatially tuned GCs (Figure 20C). These results indicate that although MCs are more likely to unveil spatially tuned firing than GCs, MCs exhibit more distributed spatial firing patterns than GCs.

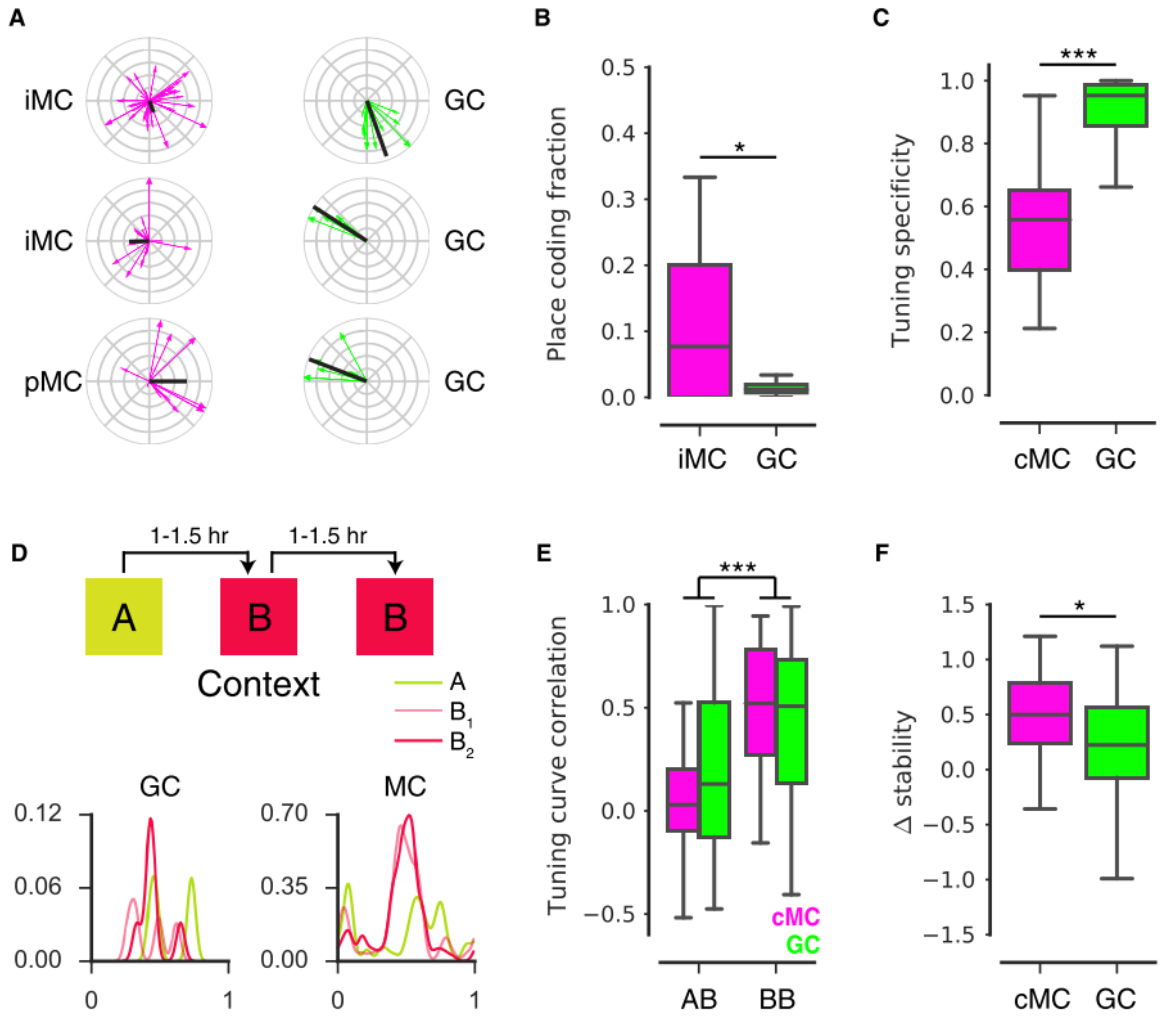

Figure 20. Tuning profiles of Mossy and Granule Cells during a discrimination experiment.

A. Spatial tuning plots for three example GCs and MCs identified as spatially tuned. Each running-related transient is represented as a vector (direction, position at onset; magnitude, inverse of occupancy), and the complex sum of these vectors forms the tuning vector (black). **B.** The fraction of cells identified as spatially tuned (≥ 4 Ca^{2+} transients, spatial information $p < 0.05$) within GC and iMC recording sessions. A higher fraction of MCs were spatially tuned than of GCs across recording sessions. **C.** Among cells identified as spatially tuned, cMCs exhibited a significantly lower tuning specificity than GCs. **D.** Top: experimental schematic. Mice ran on a treadmill for randomly administered water reward during three 12 min sessions in multisensory contexts A and B. Contexts differed in auditory, visual, olfactory, and tactile cues, and sessions were separated by 60–90 min. Bottom: spatial tuning curves are shown for an example GC and MC. **E.** The 1D correlation in spatial rate maps for GCs and cMCs were correlated in the A-B and B-B conditions. For a cell to be included, it was required to be active and spatially tuned in at least one of the two sessions being compared. Both populations exhibited a higher correlation in B-B than A-B. **F.** To calculate

the $\Delta_{stability}$, we examined the subset of cells satisfying the inclusion criterion for both conditions. The $\Delta_{stability}$ was significantly higher for cMCs than GCs.

5.3.3 Mossy cells robustly discriminate contexts

GCs in the hippocampus are thought to implement a pattern separation computation by remapping their firing fields in response to a contextual manipulation (Leutgeb et al., 2007; Knierim and Neunuebel, 2016). We asked whether this feature is unique to GCs or whether we could find evidence for pattern separation within MC population as well. Towards this goal, we compared the similarity of single cell spatial tuning profiles between two sequential exposures to either different (A-B, sessions 1 and 2) or identical (B-B, sessions 2 and 3) multisensory contexts (Figure 20D). To quantify remapping in each of the two conditions (A-B and B-B), we required that cells were spatially tuned in at least one of the two sessions being compared. This was the same paradigm used in Danielson et al. (2016a), and therefore we could directly compare the remapping of cMCs with that of GCs. For both cMCs and GCs, we found that place maps were more stable in the B-B than in the A-B conditions, as was indicated by the tuning curve correlation (Figure 20E). By considering the subset of cells incorporated in both comparisons, we calculated $\Delta_{stability}$ as the difference in stability between the B-B and A-B conditions (Figure 20F) and consequently, we found that cMCs had a significantly higher $\Delta_{stability}$ than GCs. These data suggest that MCs have the ability to robustly discriminate contexts and additionally this is accomplished based on their spatial tuning profiles.

The efficiency of pattern separation is thought to depend on the sparsity of the GC representation (Treves and Rolls, 1994; Alme et al., 2010; Chavlis and Poirazi, 2017; Chavlis et al., 2017). To investigate whether and how MCs might affect sparsity, and thus pattern separation efficiency of GCs, we implemented a simple, yet biologically relevant, computational network model of the DG (Figure 21A) as per (Chavlis et al., 2017) albeit with GCs modeled as point neurons without dendrites. The model was adjusted to reproduce an approximate sparsity of 5% (Figure 21B-D, top, green) under control conditions,

replicating the portion of GCs we found to reliably code for an environment by regularly firing transients. We then simulated the effect on GC sparsity resulting from the complete removal of MCs (Figure 21B). Removal of MCs resulted in the recruitment of significantly more GCs in response to simulated entorhinal input (Figure 21B, top, purple), and this in turn led to a decrease in the pattern separation efficiency of GCs (Figure 21B, bottom), as measured by the distance between GC populations responding to two overlapping input patterns. To investigate whether this effect was primarily mediated through the direct excitatory or indirect inhibitory pathways between MCs and GCs, we deleted each of these connections separately. While deletion of the direct excitatory connection had little effect on GC excitability and pattern separation efficiency (Figure 21C), we found that deletion of the MC to BC connection significantly increased GC excitability at the expense of pattern separation performance (Figure 21D).

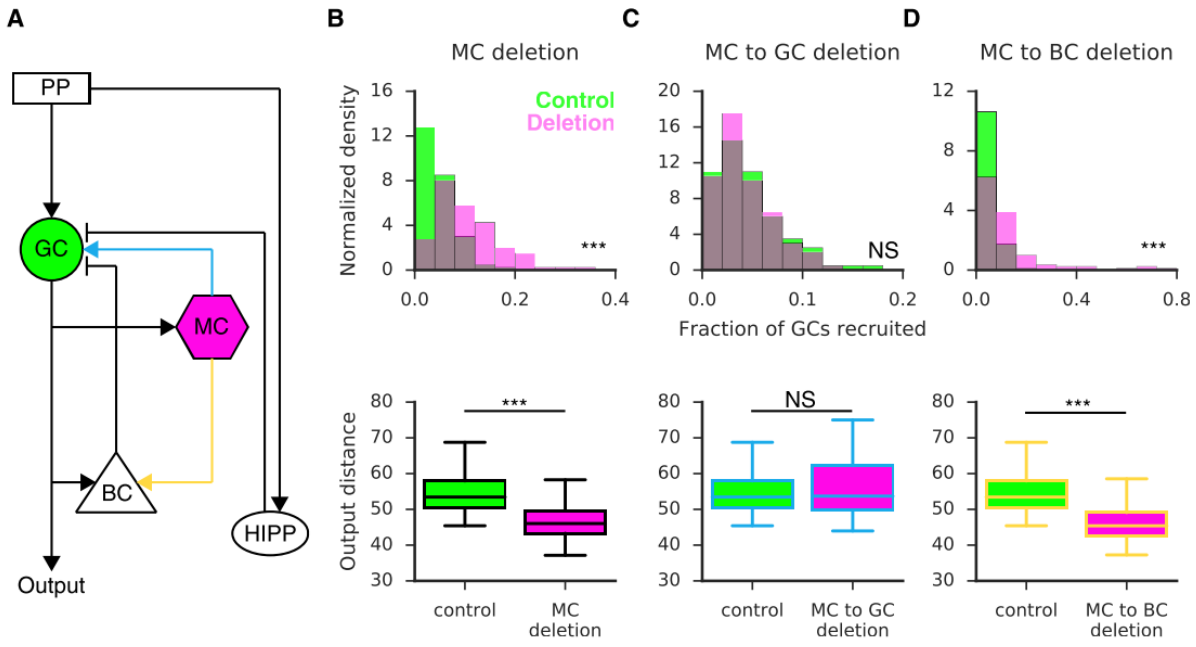

Figure 21. The Role of Mossy Cells in Pattern Separation: A Computational Approach.

A. Schematic of the DG computational model. Granule cells (GC, green) receive excitatory input from the perforant path (PP) and mossy cells (MC) in addition to feedforward inhibition from hilar perforant path-associated (HIPP) cells and feedback inhibition from basket cells (BC). MCs also provide excitation to BCs. **B-D.** *Top:* the fraction of recruited GCs in response to PP input. Green denotes the model under control conditions, while purple reflects the fraction of active GCs under various deletion conditions: complete MC deletion (B), deletion of the direct excitatory (C), or deletion of the disynaptic inhibition (D). Deletion

of MCs (B) increased the fraction of GCs recruited (KS Stat = 0.49, n = 100 control, 100 deletion simulations, $p < 0.001$, two-sample KS Test). This effect was mediated by disynaptic inhibition (D; KS Stat = 0.45, n = 100 control, 100 deletion simulations, $p < 0.001$, two-sample KS Test). *Bottom:* pattern separation efficiency is measured as the output distance between the GC populations responding to two highly overlapping PP inputs for the three aforementioned cases. MC deletion (B) results in a reduction in pattern separation efficiency ($U_{(98)} = 395$, $p < 0.001$, Mann Whitney U), and this effect again was mediated by the disynaptic inhibitory pathway (D; $U_{(98)} = 349$, $p < 0.001$, Mann Whitney U).

5.4 Discussion

In summary, we performed cellular-resolution 2p Ca^{2+} imaging of MCs during head-fixed navigation in addition to computational modeling of the local DG network. We characterized the in vivo activity levels, spatial coding fractions, context specificity, and remapping dynamics of MCs, and we identified prominent differences in these properties between MCs and GCs. We found that MCs were more active and more likely to have detected place fields than GCs, and therefore, MCs represent an active population of spatially tuned hippocampal principal neurons during behavior. In addition to exhibiting a higher place coding fraction, our results also suggest that these cells are more likely to exhibit multiple firing fields than GCs. While we cannot exclude the possibility that in vivo GCaMP Ca^{2+} imaging is biased toward the detection of burst events over single spikes in GCs, burst spiking is thought to be the most efficient mode of transmission from granule cells to their downstream targets (Bischofberger et al., 2006; Henze et al., 2002), and our most active GCs fired transients at a rate of 1–2 per minute, comparable to the burst rate reported in a previous in vivo intracellular recording study of GCs (Pernía-Andrade and Jonas, 2014). Moreover, although we cannot completely exclude the possibility that differences in intracellular Ca^{2+} buffering contributed to the observed differences in activity between GCs and MCs, the highly significant differences in activity, as reflected by both the transient AUC rate and the frequency of sharply peaked transients, suggest that differences in Ca^{2+} buffer protein expression are unlikely to fully explain our results.

Because the primary excitatory inputs onto MCs originate from large, ‘‘detonator’’ mossy terminal synapses from the mossy fibers of GCs (Scharfman, 2016), it is possible that the spatially tuned firing

pattern of MCs we observed is conveyed to MCs by GCs. However, given both the very sparse firing of GCs (Danielson et al., 2016a) and the low convergence of GCs to MCs (Scharfman, 2016), our results suggest that GC activity alone is unlikely to fully account for the high activity level and distributed spatially tuning of MCs we observed. Relatedly, it is possible that MCs are preferentially innervated by young adult-born GCs, which exhibit higher activity and more diffuse firing compared to their mature counterparts (Danielson et al., 2016a). Excitation from EC inputs (Scharfman, 1991), backprojecting CA3 pyramidal cells into hilar layer (Ishizuka et al., 1990; Myers and Scharfman, 2011) or various subcortical neuromodulatory inputs (Scharfman, 2016) might also contribute to the activity and tuning profiles of MCs.

We also found that MCs exhibit strong remapping of their firing fields during random foraging in distinct contexts, suggesting that MCs may contribute to pattern separation on the behavioral level. Our computational model also suggests that MCs contribute to the sparseness of GC representations and may thus support pattern separation in this manner as well. Furthermore, we found that this effect is primarily mediated through disynaptic inhibition, in agreement with previously published experimental data (Scharfman, 1995, 2016; Jinde et al., 2012). Indeed, an active role for MCs in pattern separation and a disinhibitory influence of MCs on GCs are supported by previous experiments in which MC loss caused transient GC hyperexcitability and impaired contextual fear learning (Jinde et al., 2012, 2013). The enhanced remapping of firing field in MCs compared to GCs we observed also suggests that context-specific inputs by sources other than GCs are conveyed to MCs. Taken together, our results support a view of hippocampal DG function in which pattern separation is implemented by the joint action of both MCs and GCs. Future in vivo studies combining recording with cell-type-specific manipulations will help to unravel the exact mechanisms by which GCs, MCs, and other excitatory and inhibitory neurons of the DG (Williams et al., 2007; Hosp et al., 2014) interact to accomplish hippocampal-dependent tasks.

Chapter 6 Role of dendritic and somatic inhibition in place cell dynamics

6.1 Preamble

Decades of accruing evidence have landed strong credence to the idea of the hippocampus being an indispensable part of the episodic memory formation, storage and retrieval processes. Specifically, in the CA1 subregion a substantial percentage of the pyramidal neurons, now called place cells, exhibit a firing pattern strongly modulated by environment location, thus acting as neural anchors of spatial memories. However, in the brain, no player is acting alone, and it is no surprise that pyramidal cells are tuned by a wide variety of local-network interneurons. Among those, interneuron-targeting, disinhibitory interneurons, expressing Vasoactive Intestinal Polypeptide (VIP) have recently been proposed to play an important role in spatial learning behavior during a goal oriented task in mice (Zaremba et al., 2017). It is hypothesized that one mechanism by which VIP^+ cells affect spatial learning is the alterations they induce in place field properties.

To examine this hypothesis we developed a biophysically constrained network model of the CA1 region that consists of 100 cells. More specifically, the network includes 80 pyramidal cells and 18 interneurons of which eight basket, two bistratified, two axoaxonic, two OLM and four VIP^+ cells. All neuron models were validated against experimental data regarding basic electrophysiological, connectivity and input properties (Lee et al., 2011; Schneider et al., 2012; Bezaire and Soltész, 2013; Sun et al., 2014; Turi et al., 2016). To simulate place cell formation in the network model, we generated grid cell input from the Entorhinal Cortex (EC) and the CA3 regions, activated in a realistic manner as observed when an animal transverses a linear track (Dombeck et al., 2010). Some of the data used to simulate the grid-like inputs are taken from in vivo experiments, such as the animal's speed and the path it follows. Realistic place fields emerged in a subpopulation of pyramidal model neurons (50-60%), in which similar EC and CA3 grid cell inputs converged onto distal/proximal apical and basal dendrites.

Ongoing work aims to assess the role of VIP^+ interneurons in the formation and/or tuning properties of place fields. Towards this goal, we will selectively remove connections for VIP^+ cells onto basket cells and VIP^+ cells onto OLM cells, and will lesion the whole VIP^+ population. Given the lack of experimental data on the precise role of VIP^+ cells in spatial memory, our modeling manipulations will provide new predictions as to the mechanistic effects of these neurons at the cellular level. These predictions can in turn guide experimental testing that will ultimately reveal whether VIP^+ cells contribute to the formation and learning related reorganization of place cells via their disinhibitory effects on somatic and/or dendritic inhibition.

6.2 Materials & Methods

6.2.1 Network construction

The network was implemented based on prior models (Cutsuridis et al., 2010; Bezaire et al., 2016). Specifically, the neuronal models and their ionic channels were implemented as per Cutsuridis et al. (2010), while the connectivity and synaptic properties were adopted from Bezaire et al. (2016). Moreover, the new single cell models for VIP-CCK and VIP-CR interneurons were simulated based on (Cutsuridis et al., 2010; Konstantoudaki et al., 2014) and adapted to experimental data. Every model cell type was heavily validated against experimental evidence with respect to both active and passive membrane properties, such as input resistance, membrane time constant, resting potential, rheobase current etc.

6.2.2 Grid-like input

The grid-like inputs were simulated as simple summation of three sinusoidal waves (Trygve Solstad et al., 2007). Specifically, a single place field was generated from the convergence of eight grid cells differing in their size and phase (see Figure 22A and APPENDIX A). The superposition of these eight grid-like inputs produced a strong input around the predefined location, while areas outside of this location received less or no input, thus creating a place cell (Figure 22B). To cover a linear track of 100

centimeters (Zerembra et al, 2017), we used 21 subsequent locations where each place cell received a perfect octal of inputs, like the ones shown below. In this example the pre-allocation of position was in the middle of the linear track.

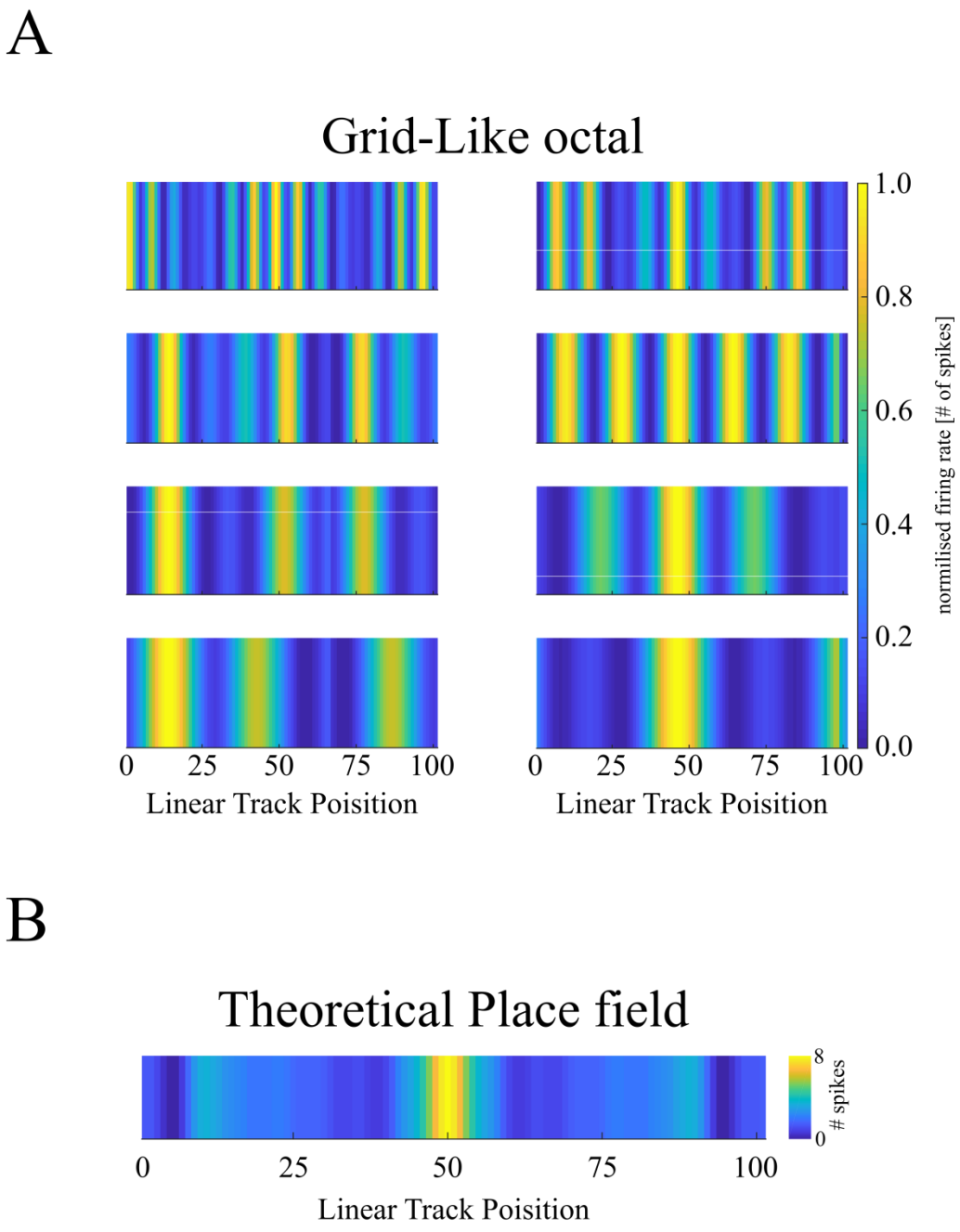

Figure 22. Grid like inputs from EC LIII and CA3 Schaffer collateral.

A. The eight different grid cells. The size of grid cells is incrementally increased from the first to the last cell of the octal. Additionally, their phase is also changing. The color-map indicates the normalized spike numbers as a function of the linear track position (yellow denotes the maximum and blue the minimum firing rate). B. The theoretical place field is in the middle of the track. This field is a result of the linear summation of the eight grid-like cells shown in A.

6.2.3 Place cell quantification

The following procedure was implemented to quantify place cell dynamics. For each pyramidal neuron, we first created the so called spike maps: each spike map consisted of the total number of spikes fired within a given space bin (1cm size). Spike maps were turned to rate maps by dividing spike counts with the time the animal spent in each space bin. Rate maps where processed with an 1-D Gaussian filter with sigma equal to 3.0, in line with the experimental procedures of our collaborators (Danielson et al., 2016b; Zaremba et al., 2017).

A number of metrics were subsequently used to characterize place field properties. These included: a) the specificity of the field in terms of the information content (spatial information) of cell discharge (Skaggs et al., 1993, 1996; Markus et al., 1994). Spatial information is the information (in bits) that a single spike conveys about the animal's location (i.e., how well cell firing predicts the animal's location). The spatial information content of a pyramidal model cell was calculated using the formula:

$$Spatial\ Information = \sum_{i=1}^{N} p_i \frac{\lambda_i}{\bar{\lambda}} \log_2 \frac{\lambda_i}{\bar{\lambda}}$$

where N is the total number of bins, p_i is the probability of occupancy of *i-th* bin, λ_i and λ represent the firing rate of each bin and the mean firing rate in Hz across all bins, respectively. Thus, a cell with high spatial informational content is likely to be a place cell. b) A second metric was the sparsity index of the spatial firing distribution, indicating the relative proportion of the track on which the cell fired:

$$Sparsity = \sum_{i=1}^{N} \frac{p_i \lambda_i^2}{\bar{\lambda}}$$

Notation is the same as before. For example, a sparsity index of *0.10* means that the cell fired on 10% of the track length. A good place cell should therefore have a low sparsity index. c) The selectivity score indicates how selective a pyramidal model cell is, based on its location-specific firing rate. The selectivity score is given by:

$$Selectivity = \frac{\max_{bin} \lambda}{\bar{\lambda}}$$

Where the nominator is the maximum firing rate and the denominator the overall mean firing rate of a model cell. Contrary to the sparsity index, the selectivity of a place cell should be as high, assuming a reasonable field size. d) Two additional metrics, the peak firing rate within a place field and the size of the place field were also used. Field size is given by the spatial extent (bins) around the peak firing rate location, in which the firing rate remains greater than 1 Hz.

6.2.4 Behavioral paradigm simulation

Experiments from collaborators reported a place-specific enrichment, namely an increase in the number of place cells encoding the reward-location in linear track experiments in mice (Zerembra et al, 2017). To simulate such learning-induced changes, we implemented two distinct scenarios, termed pre-learning and post-learning, whereby the enrichment was observed only in the post-learning scenario. Specifically, in pre-learning the artificial mouse was assumed to uniformly spend ~50ms (normal random distribution with mean and standard deviation 50 and 2 ms, respectively) in each space bin, in line with experimentally measured velocities (Cabral et al., 2014). In the post-learning condition, the mouse was assumed to spend more time (Hok et al., 2007) in the reward zone (normal random distribution with mean and standard deviation, 500 and 10 ms, correspondingly). This information was used to construct the path of locations visited and in turn the grid-like inputs.

All pyramidal cells in the network model received a convergent octal of grid-like inputs from both EC layer 3 and CA3. However, only 60% of them had input weights strong enough to generate a place field.

The remaining 40% had very small input weights, is essence representing a pool of silent place cells.. During post-learning, the weights of these silent places increased by 10. Together with the increased time spent in the reward zone, this manipulation was sufficient to generate the reward-zone specific enrichment effect observed experimentally (Zerembra et al, 2017).

6.2.5 Interneuronal manipulations

To study the role of different types of interneurons in place cell formation we simulated their deletion in the network model. Specifically, we removed: a) type of interneuron separately; b) all dendritic-targeting interneurons, c) all somatic-targeting interneurons, d) all axonic-targeting interneurons and e) all inhibitory neurons. Deletions were simulated as removal of a specific neuron type and all of its incoming and outgoing connections.

6.2.6 Network simulation and statistical analysis

The network model was simulated for 5000 and 1800 milliseconds (ms), with a time step of 0.1ms, for the pre- and post-learning protocols, respectively. The first 400ms were excluded from the analysis to enable the network to reach an equilibrium state. Simulations were repeated 10 times (runs), whereby each run represented a single passing of the linear track. Spike maps were generated using the summed activity within the 10 runs. Rate maps for each pyramidal model cell were calculated by dividing spike counts per bin with the time spent in each bin. Unless otherwise mentioned, error bars show the standard error of the mean.

Data analysis, figures and statistical analysis were done using custom made software in python 2.7.10™ (www.python.org). The two-sided, two-sample Kolmogorov–Smirnov test (K–S test) was used to compare density functions (Neuhäuser, 2011) while the t-test was used to compare their average values.

6.3 Results

6.3.1 Simulation of the behavioral (linear track) paradigm

According to experimental data from our collaborators, place cells encode the entire space (i.e., the linear track). To replicate this finding we tuned our model so as to generate a place cell every 5 cm of the track. Figure 23A shows the encoding of the linear track, which is well aligned with experimental data (Zaremba et al., 2017). This ability to encode all positions along the linear track was completely eliminated when removing all types of interneurons (Figure 23B).

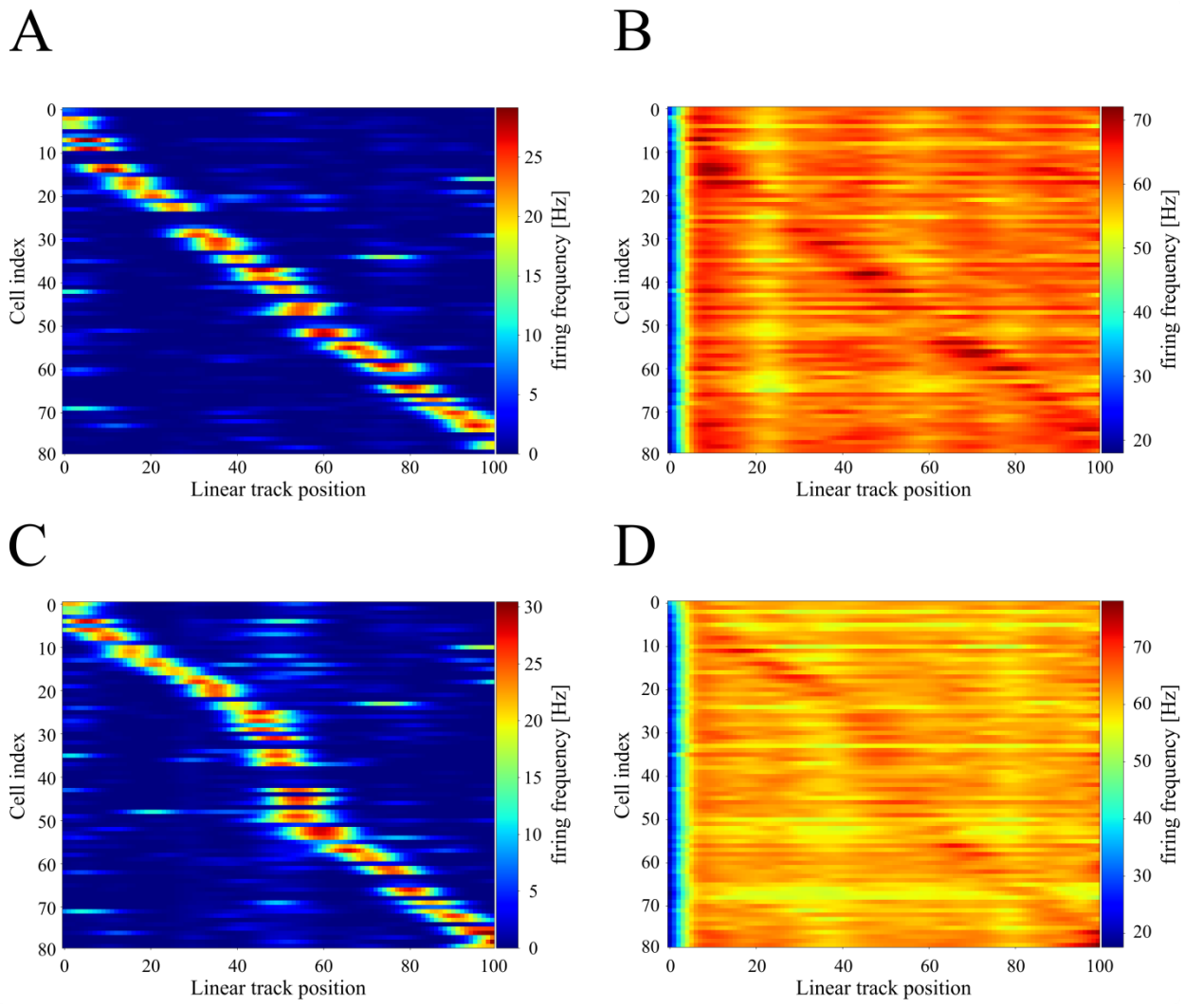

Figure 23. Place cell dynamics under pre- and post-learning protocol.

A. The firing rate of all pyramidal neurons under control conditions in the pre-learning protocol is shown as a function of space. Cell indexing is (sorted) according to peak firing rate position As shown by the elevated firing rates in the diagonal, the entire track is covered by place cells. B. Same as in A with inhibition removed. All place cells fire strongly in every position of the linear track C. Same as in A, under the post-learning condition. There is an increased representation of place cells in the reward zone (40-60 cm). D. Same as in B under the post-learning condition. Place cells fire strongly along the entire linear track.

In the post-learning condition, the mice spent more time in the reward zone and all synaptic weights of place cells encoding the reward zone increased by 10%. As a result, the network reproduced the experimentally observed enrichment in the number of place cells encoding the reward zone (Figure 23C). Removal of all inhibitory neurons eliminated the specificity of all place cells, leading to a significant drop in the spatial coding ability of the simulated network (Figure 23D). These simulations a) demonstrate the ability of the CA1 network model to reproduce both the pre- and the post-learning experimental findings regarding place-cell encoding of a linear track and b) reproduce the key role of inhibition in place cell formation (Royer et al., 2012).

6.3.2 Role of different interneurons

To investigate the contributions of different types of interneurons in place cell dynamics, we simulated the deletion (see §6.2.5) of each interneuron type independently, keeping all other parameters unchanged. We predict that BCs, VIPCCKs and OLMs have the largest contribution, as their removal impair, place cell formation under both pre-learning (Figure 24A) and post-learning (Figure 25B) conditions. The same conclusion can be reached by quantifying the place encoding capabilities of the CA1 network using the spatial information metrics (Figure 24B and Figure 25B).

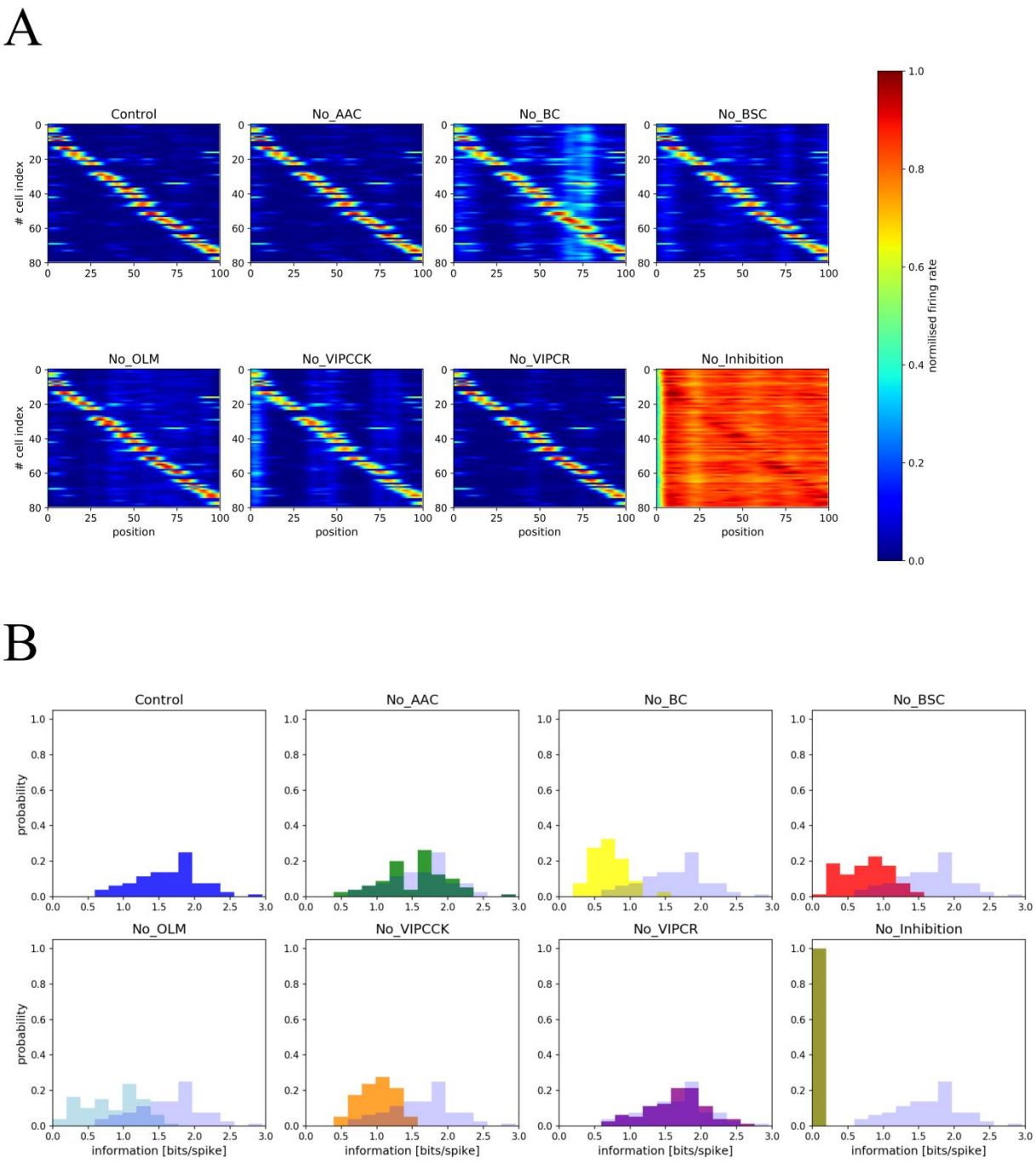

Figure 24. Place cell dynamics under distinct interneuronal lesions in the pre-learning condition.

A. While the entire track remains well represented by place cells in all but the total inhibition removal case, the level of background noise increases substantially. B. Probability density function of the spatial information calculated in bits/spike. Notably, when BCs, BSCs, OLMs and VIPCCKs are lesioned a significantly drop in information is observed. On the contrary, AACs and VIPCRs seem to have almost no effect on place cell formation.

The role of AACs cells is smaller, as the network remains capable of accurately encoding the linear track. On the contrary, the BSCs and OLMs, which provide the network with dendritic inhibition, reduce the place cell encoding efficiency, under both pre- and post-learning conditions (Figure 24 and Figure 25). Taken together, the above-mentioned results indicate that different interneuron types have distinct contributions to place cell dynamics, with BCs and VIPCCKs serving as key mediators.

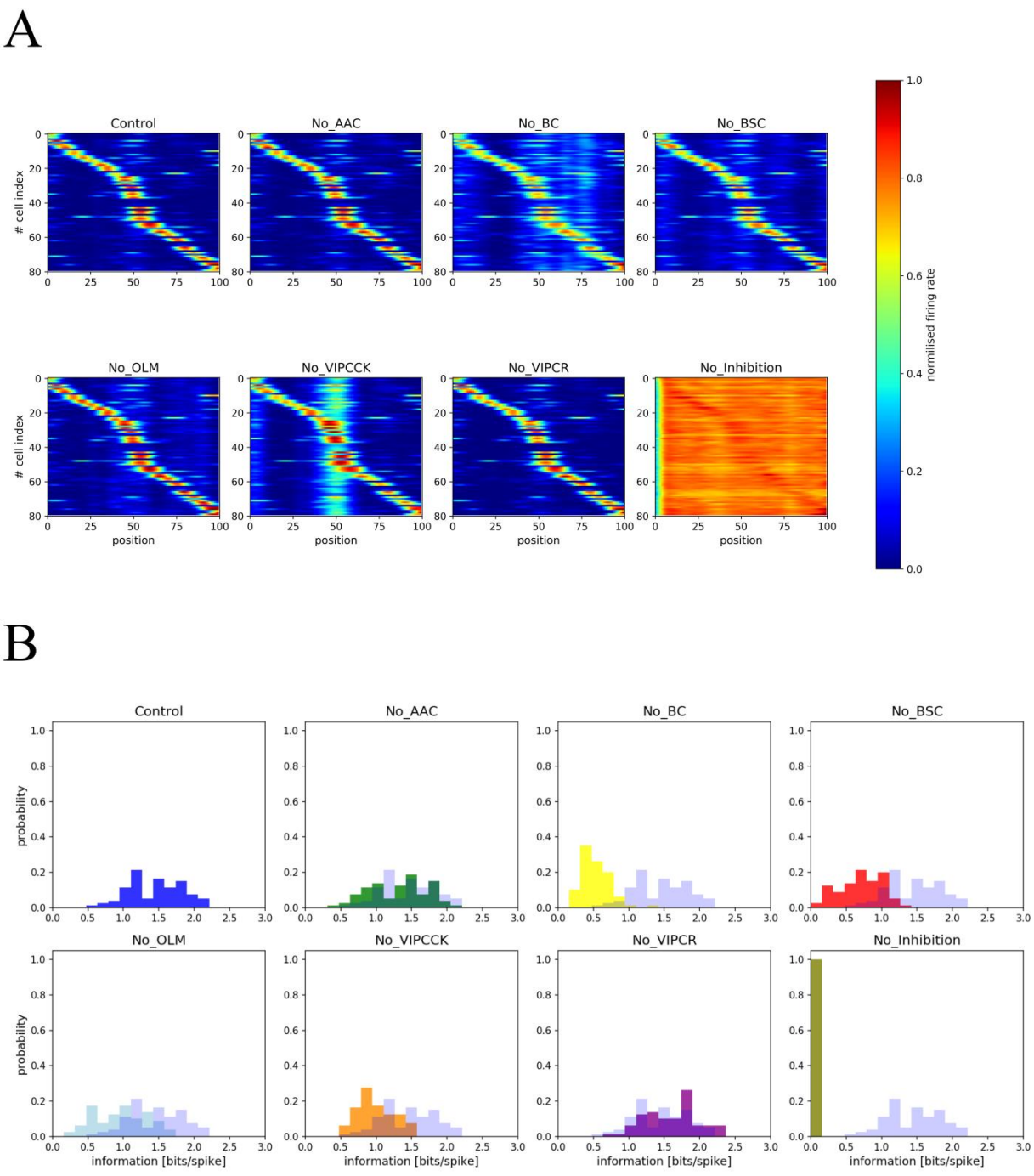

Figure 25. Place cell dynamics under various interneuronal lesions in the post-learning condition.

A. Place encoding is primarily affected by the deletion of BCs, VIPCCKs, BSCs and OLMs. B. Probability density function of the spatial information calculated in bits/spike. Notably, when BCs, BSCs, OLMs and VIPCCKs are lesioned a significant drop in information is observed. AACs and VIPCRs seem to have almost no effect on place cell formation.

Interneurons expressing VIP in CA1 mainly come from two classes; those that co-express CCK and those that co-express CR (Chamberland and Topolnik, 2012). The first class contacts CA1PCs at the soma, thus providing the network with additional perisomatic inhibition, while the latter is part of a disinhibitory circuit in CA1 contacting both BCs and OLMs. Experimental evidence suggests that in the absence of VIP cells, place cell enrichment during the reward zone is impaired. To assess whether this finding is causally linked to VIP-expressing neurons, we first simulated VIPCCK deletion in the pre- and post-learning conditions. In absence of VIPCCKs, the network lost its ability to encode the entire space and the number of place cells dropped substantially compared to the control in both pre- (Figure 24) and post-learning conditions (Figure 25).

Next, we removed VIPCRs from the network, thus reducing the level of disinhibition. This manipulation led to an increase in firing rates for both BCs and OLMs which in turn led to a decrease in pyramidal neuron firing rates. However, this reduction in excitability did not impair place cell formation and thus place encoding remained unaffected. These simulations suggest that soma-targeting but not disinhibitory VIP-expressing interneurons play a role in place cell formation and enrichment.

Next, we studied the role of dendritic vs. somatic/axonal inhibition in place cell formation. Hence, we implemented two model networks: one without dendritic inhibition to CA1PCs, i.e., BSCs and OLMs were removed, and a second without somatic and axonal inhibition, i.e., AACs, BCs and VIPCCKs were removed. Interestingly, in both cases we noticed that our network lost its ability to create place cells, and therefore the number of place cells reduced under both cases. This was evident either by inspecting the heat maps or by comparing the place cell metrics with the control case, under both pre- and post-learning conditions.

In summary, these simulations predict that the lesion of one interneuronal type at a time provoke only a small change in place encoding. However, some types and more specifically the BCs, VIPCCKs and the OLMs seem to have a greater effect on place cell formation. On the contrary, when inhibition is killed by

removing all interneurons the model failed in forming place cells. Interestingly, the VIPCR cells seem to have no effect on place cell formation. A possible explanation of this observation is that the used synaptic weights from those neurons onto BCs and OLMs were not optimized. These cells are poorly studied and thus, we moved forward to explore their weights.

6.3.3 Exploration of VIP^+/CR^+ synaptic weights

Given the lack of experimental data regarding the connectivity strength of VIPCR synapses, we performed an extensive parameter exploration to test whether these interneurons play a role under conditions that differ from those currently incorporated in our network model. For these simulations we systematically modified the weights from VIPCR to BCs and/or to OLMs and assessed spatial information, sparsity, selectivity and place field size.

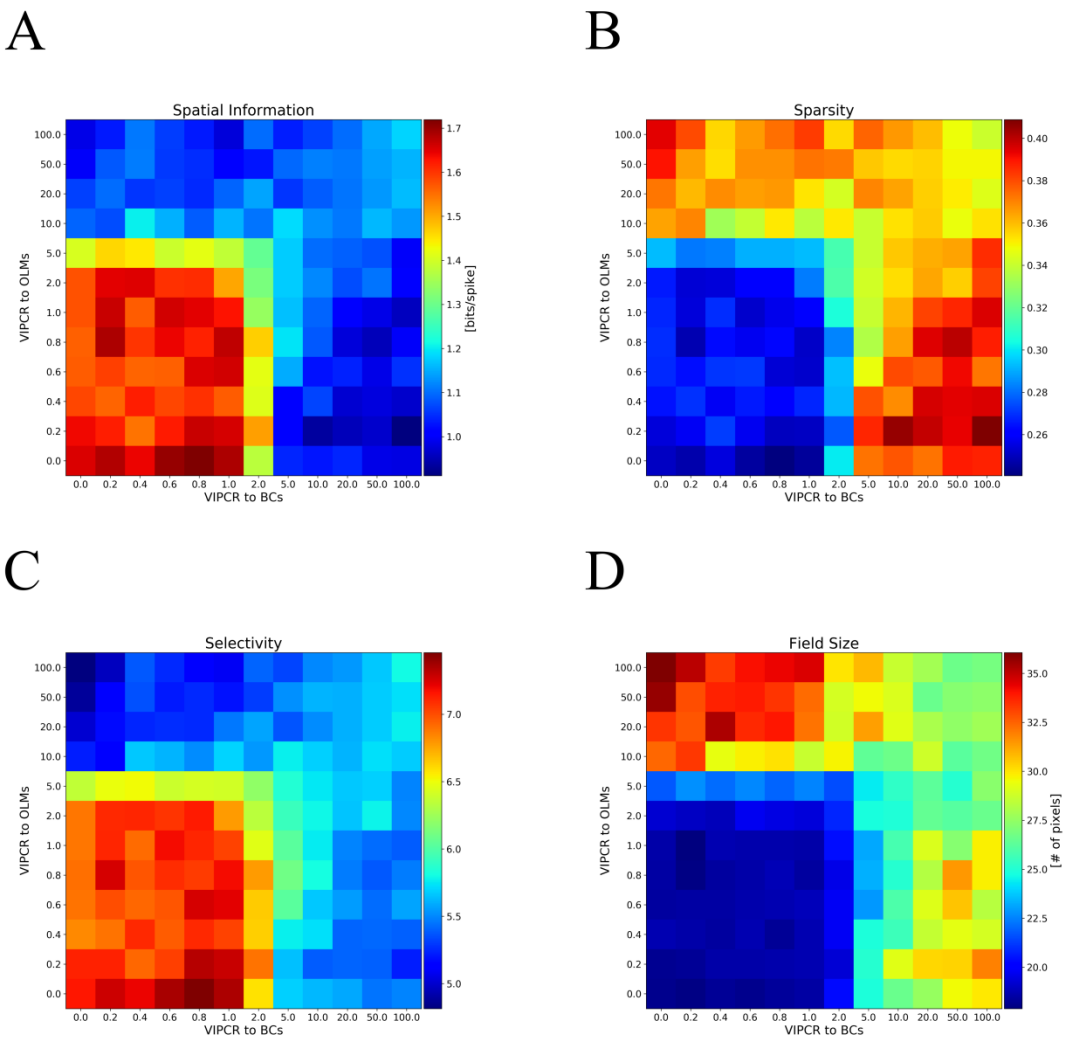

Figure 26. Parametric exploration of synaptic strength between VIPCRs and BCs/OLMs.

Synaptic weights were multiplied by a factor of 0.0 to 100.0, with unequal steps. A. Spatial information in bits/spike. Values shown are averages across all pyramidal cells. B. Sparsity index. All values are calculated as averages across all pyramidal cells. C. As in A and B, but here the selectivity is shown as the average over all pyramidal neurons. D. As in A., but here the place cell size is depicted as the average over all pyramidal cells.

These simulations identified a parameter sub-region that maximizes place cell formation efficiency Figure 26. Weights from 0.0 to 5.0 in the VIPCR to OLM connection, and 0.0 to 2.0 in the VIPCR to BC connection have significantly larger spatial information, selectivity and lower sparsity and field size. This suggests that weights used in our network model maybe be suboptimal for revealing the role of VIP

interneurons in place cell formation. It is of high importance to mention that connections from VIPCR to other interneurons are poorly studied experimentally and thus, the exploration of these values using our computational model is critical.

6.4 Discussion

The purpose of the current study was to determine the role of inhibition in place cell formation, and therefore to understand the mechanisms that underlie spatial memory formation. Towards this goal, we developed a biophysical CA1 network model consisting of 80 pyramidal cells and six different types of inhibitory interneurons: two AACs, two BSCs, two OLMs, two VIPCCKs, two VIPCRs and eight BCs. All neuronal types were constructed as per (Cutsuridis et al., 2010), apart from the VIPCR interneuron which was based morphologically on (Cutsuridis et al., 2010) and biophysically on (Konstantoudaki et al., 2014). Input to the network was provided by several grid-like cells which represent the EC LIII and CA3 predominant input to the CA1 area. In addition, all interneurons received inhibitory input from the septum in order to simulate the theta rhythm found in hippocampus (Buzsáki, 2002).

The main experiments of this project were to replicate the place cells that formed in mice hippocampi under the exploration of a linear track (Zaremba et al., 2017). Therefore, we have implemented the grid-like input in such a way that the whole linear track is covered with place cells and hence, the space is encoded by specific CA1PCs. Our model replicates both pre- and post-learning conditions, whereby the animal learns to stop in a specific location of the track where a reward is provided. Specifically, in the post-learning condition, under which the animal spends more time within the reward zone, our model captures the reported enrichment, namely the increase in the number of place cells firing within the reward zone. To explore how different types of interneurons contribute to place cell formation and/or reward zone enrichment, we simulated the deletion of each type of interneuron in the model. We predict that removal of all forms of inhibition is detrimental for place encoding while individual interneuron types have varying effects.

Specifically, removal of either BCs or VIPCCKs impairs place encoding capability while removal of AACs had minimal effect. Moreover, BSCs and OLMs appeared to be critical for place cell dynamics as when separately removed the network lost its efficiency in spatial encoding. Surprisingly, the VIPCRs which disinhibit the network had a very small effect on place cell formation. One possible explanation is that the synapses made by these neurons on BCs and OLMs were not strong enough and hence, in their absence the BC and OLM firing rate was slightly increased. However, when we manipulated the aforementioned weights their effect was significant.

Although this research extends our knowledge of place cell dynamics and the distinct role of different inhibitory neurons in this complex computational circuitry, more research is required to determine the efficacy of distinct interneurons in place cell dynamics.

Chapter 7 Conclusions

This dissertation aims to unravel some of the mysteries surrounding memory formation and storage in the brain. Therefore, the study of the hippocampus was critical as it is a fundamental brain region for memory formation, storage and retrieval and its function is highly associated with spatial navigation. This investigation will enhance our understanding of how memories are encoding in the brain and which are the key mechanisms that affect their efficient function. This dissertation is divided in two main projects; the first part is a thorough examination of pattern separation, while the second scrutinizes the spatial memory formation. Hence, a DG and a CA1 network were implemented in order to study the key hippocampal areas involved in the aforementioned tasks. The methodological approach taken in this study was a computational modeling approach, which would enable us to study aspects of these areas that were not studied yet, mainly because many features are hard to be studied experimentally.

7.1 Key players mediating pattern separation

The main goal of the current study was to determine, if any, the role of granular dendrites in pattern separation task. Pattern separation is the ability that our brain has to distinguish similar incoming information. There is a growing body of literature that recognizes the importance of DG in pattern separation. Due to several reasons, DG is considered as the perfect candidate to accomplish this task. One reason is that GCs found in DG outnumber both the incoming cell population (EC LII) and the next subregion, the CA3. Furthermore, the sparse connectivity from EC LII is another factor as well as the sparse firing of GCs in general. However, there is a little published data in literature about the morphology of GCs and also there has been no detailed investigation of the role of dendrites in pattern separation. Thus, the purpose of this investigation is to explore the relationship between GC dendrites and pattern separation providing insights on new players that mediate pattern separation efficacy.

By implementing a simple, yet biologically relevant, spiking neural network we aimed to identify the role of dendrites in the aforementioned computational task. Towards this aim, we built a hybrid spiking neural model with various dendritic compartments. The current study found that dendrites serve as another mechanism to pattern separation efficacy accomplishing this by mediating sparsity of GCs activity. Specifically, we found a positive correlation with dendritic number and pattern separation efficacy; as the dendritic number becomes greater, the pattern separation efficacy increased and also, when dendritic number was decreased we observed a significant pattern separation drop. However, the results of this study unravel other mechanisms through which the sparsity is mediated and the pattern separation performance is better such as the leak current, the somatic size and the synaptic weights suggesting that dendrites are not necessary and sufficient for pattern separation efficacy, rather they are an indirect mechanism that controls sparsity.

Next, we used a simplistic version of this model to study the explicit role of the mysterious MCs during a behavioral task. MCs are located in the polymorphic DG layer (or hilus) and are glutamatergic cells. They form a circuitry with GCs and BCs as they contact both of them. The most obvious finding to emerge from the analysis is that MCs are more excitable and less sparse comparing with DGs. On the contrary they had spatial tuning profiles and their firing was less stable across different environments. Using our model, we explored how their afferents affect pattern separation efficacy. In this direction, we have used our model and we test the DG network against a pattern separation protocol. Interestingly, we found that MC to BC connection was responsible for the high pattern separation efficacy under control conditions, and thus in a model with deletion of this connection the performance of the network significantly dropped. On the contrary, the excitatory connection from MCs to GCs seemed to have no effect in pattern separation performance.

Overall, this study strengthens the idea that dendrites are key mediators of memory processes. Although a direct link of dendritic structure and morphology with pattern separation efficacy was not found, their indirect role in this task should be taken into account as dendrites mediate sparsity in a positive way.

Together with the role of MCs in pattern separation, these findings enhance our understanding of how different mechanisms could eventually be involved in a mnemonic process such as pattern separation. Further experimental investigations regarding the role of granular dendrites and mossy cell in this mnemonic process is needed in order to unravel their contribution when pattern separation ability is highly demanded.

7.2 Exploring the role of distinct interneurons in place cell dynamics

The second aim of this study was to investigate the effects of inhibition and disinhibition in spatial memory. Spatial navigation is important for ordinary life and it is another form of memory in which hippocampus is widely believed that plays an important role. Specifically, different hippocampal and parahippocampal areas are involved in this task, such as the CA3 and CA1 hippocampal subregions and EC of medial temporal lobe. Hence, we used a computational model of CA1 network as there is a considerable amount of literature which implicates this region with spatial memory and navigational skills. These cells are spatially tuned, i.e., they fire when an animal is passing from a specific location in space. Additionally, several theories recognize the EC grid cells as a key mediator of place cell formation and thus, we have incorporated grid-like input to our network. Although it is widely known that inhibition is crucial for normal brain function, little has been done in order to investigate the exact role of inhibitory neurons in spatial memory. The CA1 subregion contains numerous types of interneurons and together with pyramidal cells form a very complex network. Thus, assessing spatial memory with a computational model eventually enabled us to examine individually each type of interneuron and its contribution to place cell formation and dynamics.

The most obvious finding to emerge from this study is that inhibition is necessary in order for place cells to be formed across the linear track. When inhibition is killed by removing all interneurons the network lost its ability to encode the space. Then we asked what, if any, are the effects of each one interneuron in place cell formation and dynamics. Interestingly, we have found that BCs and VCCKs had a major

impact, as well as OLMs and BSCs. However, in absence of AACs the place cell characteristics seem to be similar to ones found under control conditions. Contrary to expectations, we did not find a significant difference between control and VIPCR lesioned conditions. A possible explanation for these results may be the lack of adequate experimental evidence about the synaptic properties of VIPCR neurons and specially, we did not found their exact efferent properties in synapses formed from VIPCR to BCs and OLMs. Thus, a follow up question to ask is what would be the role of VIPCR if we change their synaptic weights. Towards this direction, we ran our model against the same input protocol for different synaptic weights and we could infer a more appropriate set of parameters under control conditions. Further studies, which take these variables into account, will need to be undertaken.

Despite its exploratory nature, this study offers some insight into place cell formation and characteristics in accordance with inhibitory neurons found in CA1 area. The present study confirms previous findings and contributes additional evidence that suggests a role of interneurons in spatial memory formation. However, further experimental and computational research is required to examine more accurate the passive and active properties of VIP^+ interneurons, as well as to define their connectivity properties.

Chapter 8 References

Acsády L, Kamondi A, Sík A, Freund TF, Buzsáki G (1998) GABAergic cells are the major postsynaptic targets of mossy fibers in the rat hippocampus. *J Neurosci* **18**:3386–3403.

Agster KL, Burwell RD (2009) Cortical efferents of the perirhinal, postrhinal, and entorhinal cortices of the rat. *Hippocampus* **19**:1159–1186.

Agster KL, Tomás Pereira I, Saddoris MP, Burwell RD (2016) Subcortical connections of the perirhinal, postrhinal, and entorhinal cortices of the rat. II. efferents. *Hippocampus* **26**:1213–1230.

Aimone JB, Deng W, Gage FH (2010) Adult neurogenesis: Integrating theories and separating functions. *Trends Cogn Sci* **14**:325–337.

Aimone JB, Deng W, Gage FH (2011) Resolving New Memories: A Critical Look at the Dentate Gyrus, Adult Neurogenesis, and Pattern Separation. *Neuron* **70**:589–596.

Ally BA, Hussey EP, Ko PC, Molitor RJ (2013) Pattern separation and pattern completion in Alzheimer's disease: Evidence of rapid forgetting in amnestic mild cognitive impairment. *Hippocampus* **23**:1246–1258.

Alme CB, Buzzetti RA, Marrone DF, Leutgeb JK, Chawla MK, Schaner MJ, Bohanick JD, Khoboko T, Leutgeb S, Moser EI, Moser M-B, McNaughton BL, Barnes CA (2010) Hippocampal granule cells opt for early retirement. *Hippocampus* **20**:1109–1123.

Amaral DG (1978) A Golgi study of cell types in the hilar region of the hippocampus in the rat. *J Comp Neurol* **182**:851–914.

Amaral DG, Ishizuka N, Claiborne BJ (1990) Neurons, numbers and the hippocampal network. *Prog Brain Res* **83**:1–11.

Amaral DG, Kurz J (1985) An analysis of the origins of the cholinergic and noncholinergic septal projections to the hippocampal formation of the rat. *J Comp Neurol* **240**:37–59.

Amaral DG, Lavenex P (2007) Hippocampal neuroanatomy. In: The hippocampus book, 1st ed. (Andersen P, Morris R, Amaral DG, Bliss T, O'Keefe J, eds), pp 37–100. New York: Oxford University Press, Inc.

Amaral DG, Scharfman HE, Lavenex P (2007) The dentate gyrus: fundamental neuroanatomical organization (dentate gyrus for dummies). In: The Dentate Gyrus: A comprehensive guide to structure, function, and clinical implications (Scharfman HE, ed), pp 3–22. Amsterdam: Elsevier

B.V.

Amaral DG, Witter MP (1989) The three-dimensional organization of the hippocampal formation: A review of anatomical data. *Neuroscience* **31**:571–591.

Aradi I, Holmes WR (1999) Role of multiple calcium and calcium-dependent conductances in regulation of hippocampal dentate granule cell excitability. *J Comput Neurosci* **6**:215–235.

Bakker A, Kirwan CB, Miller M, Stark CEL (2008) Pattern separation in the human hippocampal CA3 and dentate gyrus. *Science* **319**:1640–1642.

Bannister NJ, Larkman AU (1995a) Dendritic morphology of CA1 pyramidal neurones from the rat hippocampus: I. Branching patterns. *J Comp Neurol* **360**:150–160.

Bannister NJ, Larkman AU (1995b) Dendritic morphology of CA1 pyramidal neurones from the rat hippocampus: II. Spine distributions. *J Comp Neurol* **360**:161–171.

Bartos M, Vida I, Frotscher M, Geiger JRP, Jonas P (2001) Rapid signaling at inhibitory synapses in a dentate gyrus interneuron network. *J Neurosci* **21**:2687–2698.

Baude A, Bleasdale C, Dalezios Y, Somogyi P, Klausberger T (2007) Immunoreactivity for the GABAA receptor alpha1 subunit, somatostatin and Connexin36 distinguishes axoaxonic, basket, and bistratified interneurons of the rat hippocampus. *Cereb Cortex* **17**:2094–2107.

Bezaire MJ, Raikov I, Burk K, Vyas D, Soltész I (2016) Interneuronal mechanisms of hippocampal theta oscillations in a full-scale model of the rodent CA1 circuit. *Elife* **5**:1–106.

Bezaire MJ, Soltész I (2013) Quantitative assessment of CA1 local circuits: Knowledge base for interneuron-pyramidal cell connectivity. *Hippocampus* **23**:751–785.

Bokor H, Csáki Á, Kocsis K, Kiss J (2002) Cellular architecture of the nucleus reuniens thalami and its putative aspartatergic/glutamatergic projection to the hippocampus and medial septum in the rat. *Eur J Neurosci* **16**:1227–1239.

Bolz L, Heigele S, Bischofberger J (2015) Running Improves Pattern Separation during Novel Object Recognition. *Brain Plast* **1**:129–141.

Brette R, Gerstner W (2005) Adaptive Exponential Integrate-and-Fire Model as an Effective Description of Neuronal Activity. *J Neurophysiol* **94**:3637–3642.

Brette R, Goodman DFM (2011) Vectorized algorithms for spiking neural network simulation. *Neural Comput* **23**:1503–1535.

Brun VH, Otnass MK, Molden S, Steffenach H-A, Witter MP, Moser M-B, Moser EI (2002) Place cells

and place recognition maintained by direct entorhinal-hippocampal circuitry. *Science* **296**:2243–2246.

Buckmaster PS, Jongen-Rêlo AL (1999) Highly specific neuron loss preserves lateral inhibitory circuits in the dentate gyrus of kainate-induced epileptic rats. *J Neurosci* **19**:9519–9529.

Buhl EH, Halasy K, Somogyi P (1994) Diverse sources of hippocampal unitary inhibitory postsynaptic potentials and the number of synaptic release sites. *Nature* **368**:823–828.

Burgess N, Maguire EA, O'Keefe J (2002) The human hippocampus and spatial and episodic memory. *Neuron* **35**:625–641.

Burkitt AN (2006) A Review of the Integrate-and-fire Neuron Model: I. Homogeneous Synaptic Input. *Biol Cybern* **95**:1–19.

Burwell RD (2006) The Parahippocampal Region: Corticocortical Connectivity. *Ann N Y Acad Sci* **911**:25–42.

Burwell RD, Amaral DG (1998) Cortical afferents of the perirhinal, postrhinal, and entorhinal cortices of the rat. *J Comp Neurol* **398**:179–205.

Buzsáki G (2002) Theta Oscillations in the Hippocampus. *Neuron* **33**:325–340.

Cabral HO, Fouquet C, Rondi-Reig L, Pennartz CMA, Battaglia FP (2014) Single-Trial Properties of Place Cells in Control and CA1 NMDA Receptor Subunit 1-KO Mice. *J Neurosci* **34**:15861–15869.

Canto CB, Wouterlood FG, Witter MP (2008) What Does the Anatomical Organization of the Entorhinal Cortex Tell Us? *Neural Plast* **2008**:1–18.

Chamberland S, Topolnik L (2012) Inhibitory control of hippocampal inhibitory neurons. *Front Neurosci* **6**:1–13.

Chavlis S, Petrantonakis PC, Poirazi P (2017) Dendrites of dentate gyrus granule cells contribute to pattern separation by controlling sparsity. *Hippocampus* **27**:89–110.

Chavlis S, Poirazi P (2017) Pattern separation in the hippocampus through the eyes of computational modeling. *Synapse* **71**:e21972.

Chiang PH, Wu PY, Kuo TW, Liu YC, Chan CF, Chien TC, Cheng JK, Huang YY, Chiu C Di, Lien CC (2012) GABA Is Depolarizing in Hippocampal Dentate Granule Cells of the Adolescent and Adult Rats. *J Neurosci* **32**:62–67.

Claiborne BJ, Amaral DG, Cowan WM (1990) Quantitative, three-dimensional analysis of granule cell dendrites in the rat dentate gyrus. *J Comp Neurol* **302**:206–219.

Clark RE, Broadbent NJ, Squire LR (2005a) Hippocampus and remote spatial memory in rats. *Hippocampus* **15**:260–272.

Clark RE, Broadbent NJ, Squire LR (2005b) Impaired remote spatial memory after hippocampal lesions despite extensive training beginning early in life. *Hippocampus* **15**:340–346.

Clark RE, Broadbent NJ, Squire LR (2007) The Hippocampus and Spatial Memory: Findings with a Novel Modification of the Water Maze. *J Neurosci* **27**:6647–6654.

Coultrip R, Granger R, Lynch G (1992) A cortical model of winner-take-all competition via lateral inhibition. *Neural Networks* **5**:47–54.

Cutsuridis V, Cobb S, Graham BP (2010) Encoding and retrieval in a model of the hippocampal CA1 microcircuit. *Hippocampus* **20**:423–446.

Danielson NB, Kaifosh PW, Zaremba JD, Lovett-Barron M, Tsai J, Denny CA, Balough EM, Goldberg AR, Drew LJ, Hen R, Losonczy A, Kheirbek MA (2016a) Distinct Contribution of Adult-Born Hippocampal Granule Cells to Context Encoding. *Neuron* **90**:101–112.

Danielson NB, Zaremba JD, Kaifosh PW, Bowler J, Ladow M, Losonczy A (2016b) Sublayer-specific coding dynamics during spatial navigation and learning in hippocampal area CA1. *Neuron* **91**:1–14.

Das T, Ivleva EI, Wagner AD, Stark CEL, Tamminga CA (2014) Loss of pattern separation performance in schizophrenia suggests dentate gyrus dysfunction. *Schizophr Res* **159**:193–197.

Deng W, Aimone JB, Gage FH (2010) New neurons and new memories: how does adult hippocampal neurogenesis affect learning and memory? *Nat Rev Neurosci* **11**:339–350.

Desmond NL, Scott CA, Jane JA, Levy WB (1994) Ultrastructural identification of entorhinal cortical synapses in CA1 stratum lacunosum-moleculare of the rat. *Hippocampus* **4**:594–600.

Deuchars J, Thomson AM (1996) CA1 pyramid-pyramid connections in rat hippocampus in vitro: dual intracellular recordings with biocytin filling. *Neuroscience* **74**:1009–1018.

Dolleman-Van der Weel MJ, Witter MP (2000) Nucleus reuniens thalami innervates gamma aminobutyric acid positive cells in hippocampal field CA1 of the rat. *Neurosci Lett* **278**:145–148.

Dombeck DA, Harvey CD, Tian L, Looger LL, Tank DW (2010) Functional imaging of hippocampal place cells at cellular resolution during virtual navigation. *Nat Neurosci* **13**:1433–1440.

Dragoi G, Carpi D, Recce M, Csicsvari J, Buzsáki G (1999) Interactions between hippocampus and medial septum during sharp waves and theta oscillation in the behaving rat. *J Neurosci* **19**:6191–6199.

Eichenbaum H (2015) The Hippocampus as a Cognitive Map … of Social Space. *Neuron* **87**:9–11.

Eichenbaum H (2017) The role of the hippocampus in navigation is memory. *J Neurophysiol* **117**:1785–1796.

Einstein G, Buranosky R, Crain BJ (1994) Dendritic pathology of granule cells in Alzheimer's disease is unrelated to neuritic plaques. *J Neurosci* **14**:5077–5088.

Ekstrom AD, Kahana MJ, Caplan JB, Fields TA, Isham EA, Newman EL, Fried I (2003) Cellular networks underlying human spatial navigation. *Nature* **425**:184–188.

Eriksson PS (2003) Neurogenesis and its implications for regeneration in the adult brain. *J Rehabil Med* **35**:17–19.

Faghihi F, Moustafa AA (2015) A computational model of pattern separation efficiency in the dentate gyrus with implications in schizophrenia. *Front Syst Neurosci* **9**:1–12.

Francavilla R, Luo X, Magnin E, Tyan L, Topolnik L (2015) Coordination of dendritic inhibition through local disinhibitory circuits. *Front Synaptic Neurosci* **7**.

Freund TF, Buzsáki G (1996) Interneurons of the hippocampus. *Hippocampus* **6**:347–470.

Fyhn M, Molden S, Witter MP, Moser EI, Moser MB (2004) Spatial representation in the entorhinal cortex. *Science* **305**:1258–1264.

Gallistel CR (1990) The organization of learning. MIT press.

Geiger JRP, Lübke J, Roth A, Frotscher M, Jonas P (1997) Submillisecond AMPA receptor-mediated signaling at a principal neuron- interneuron synapse. *Neuron* **18**:1009–1023.

Ghosh S, Laxmi TR, Chattarji S (2013) Functional connectivity from the amygdala to the hippocampus grows stronger after stress. *J Neurosci* **33**:7234–7244.

Goodman DFM, Brette R (2009) The Brian simulator. *Front Neurosci* **3**:192–197.

Gur RC, Turetsky BI, Matsui M, Yan M, Bilker W, Hughett P, Gur RE (1999) Sex differences in brain gray and white matter in healthy young adults: correlations with cognitive performance. *J Neurosci* **19**:4065–4072.

Hafting T, Fyhn M, Molden S, Moser MB, Moser EI (2005) Microstructure of a spatial map in the entorhinal cortex. *Nature* **436**:801–806.

Halasy K, Somogyi P (1993) Distribution of GABAergic synapses and their targets in the dentate gyrus of rat: a quantitative immunoelectron microscopic analysis. *J Hirnforsch* **34**:299–308.

Hama K, Arii T, Kosaka T (1989) Three-dimensional morphometrical study of dendritic spines of the granule cell in the rat dentate gyrus with HVEM stereo images. *J Electron Microsc Tech* **12**:80–87.

Harney SC, Jones M V (2002) Pre- and postsynaptic properties of somatic and dendritic inhibition in dentate gyrus. *Neuropharmacology* **43**:584–594.

Hartley T, Lever C, Burgess N, O'Keefe J (2014) Space in the brain: how the hippocampal formation supports spatial cognition. *Philos Trans R Soc Lond B Biol Sci* **369**:20120510.

Hartmann D, Frotscher M, Sievers J (1994) Development of granule cells, and afferent and efferent connections of the dentate gyrus after experimentally induced reorganization of the supra- and infrapyramidal blades. *Acta Anat (Basel)* **150**:25–37.

Henze DA, Buzsáki G (2007) Hilar mossy cells: functional identification and activity in vivo. In: The Dentate Gyrus: A comprehensive guide to structure, function, and clinical implications (Scharfman HE, ed), pp 199–216. Amsterdam: Elsevier B.V.

Hines ML, Carnevale NT (1997) The NEURON simulation environment. *Neural Comput* **9**:1179–1209.

Hok V, Lenck-Santini P-P, Roux S, Save E, Muller RU, Poucet B (2007) Goal-Related Activity in Hippocampal Place Cells. *J Neurosci* **27**:472–482.

Hosp JA, Strüber M, Yanagawa Y, Obata K, Vida I, Jonas P, Bartos M (2014) Morpho-physiological criteria divide dentate gyrus interneurons into classes. *Hippocampus* **24**:189–203.

Huh CYL, Goutagny R, Williams S (2010) Glutamatergic neurons of the mouse medial septum and diagonal band of Broca synaptically drive hippocampal pyramidal cells: relevance for hippocampal theta rhythm. *J Neurosci* **30**:15951–15961.

Ikrar T, Guo N, He K, Besnard A, Levinson S, Hill AS, Lee HK, Hen R, Xu X, Sahay A (2013) Adult neurogenesis modifies excitability of the dentate gyrus. *Front Neural Circuits* **7**:204.

Ishizuka N, Weber J, Amaral DG (1990) Organization of intrahippocampal projections originating from CA3 pyramidal cells in the rat. *J Comp Neurol* **295**:580–623.

Izhikevich EM (2003) Simple model of spiking neurons. *IEEE Trans Neural Netw* **14**:1569–1572.

Jahr CE, Stevens CF (1990) Voltage dependence of NMDA-activated macroscopic conductances predicted by single-channel kinetics. *J Neurosci* **10**:3178–3182.

Jain S, Yoon SY, Zhu L, Brodbeck J, Dai J, Walker D, Huang Y (2012) Arf4 Determines Dentate Gyrus-Mediated Pattern Separation by Regulating Dendritic Spine Development. *PLoS One* **7**:1–15.

Jinde S, Zsiros V, Jiang Z, Nakao K, Pickel J, Kohno K, Belforte JE, Nakazawa K (2012) Hilar Mossy

Cell Degeneration Causes Transient Dentate Granule Cell Hyperexcitability and Impaired Pattern Separation. *Neuron* **76**:1189–1200.

Jinde S, Zsiros V, Nakazawa K (2013) Hilar mossy cell circuitry controlling dentate granule cell excitability. *Front Neural Circuits* **7**:14.

Jung MW, McNaughton BL (1993) Spatial selectivity of unit activity in the hippocampal granular layer. *Hippocampus* **3**:165–182.

Kirwan CB, Stark CEL (2007) Overcoming interference: an fMRI investigation of pattern separation in the medial temporal lobe. *Learn Mem* **14**:625–633.

Klausberger T, Somogyi P (2008) Neuronal Diversity and Temporal Dynamics: The Unity of Hippocampal Circuit Operations. *Science (80-)* **321**:53–57.

Kneisler TB, Dingledine R (1995) Spontaneous and synaptic input from granule cells and the perforant path to dentate basket cells in the rat hippocampus. *Hippocampus* **5**:151–164.

Knierim JJ, Neunuebel JP (2016) Tracking the flow of hippocampal computation: Pattern separation, pattern completion, and attractor dynamics. *Neurobiol Learn Mem* **129**:38–49.

Kohara K, Pignatelli M, Rivest AJ, Jung H-Y, Kitamura T, Suh J, Frank D, Kajikawa K, Mise N, Obata Y, Wickersham IR, Tonegawa S (2013) Cell type–specific genetic and optogenetic tools reveal hippocampal CA2 circuits. *Nat Neurosci* **17**:269–279.

Köhler C (1985) Intrinsic projections of the retrohippocampal region in the rat brain. I. The subicular complex. *J Comp Neurol* **236**:504–522.

Konstantoudaki X, Papoutsi A, Chalkiadaki K, Poirazi P, Sidiropoulou K (2014) Modulatory effects of inhibition on persistent activity in a cortical microcircuit model. *Front Neural Circuits* **8**:7.

Krueppel R, Remy S, Beck H (2011) Dendritic integration in hippocampal dentate granule cells. *Neuron* **71**:512–528.

Lacy JW, Yassa MA, Stark SM, Muftuler LT, Stark CEL (2011) Distinct pattern separation related transfer functions in human CA3/dentate and CA1 revealed using high-resolution fMRI and variable mnemonic similarity. *Learn Mem* **18**:15–18.

Larimer P, Strowbridge BW (2008) Nonrandom local circuits in the dentate gyrus. *J Neurosci* **28**:12212–12223.

Lee ACH, Brodersen KH, Rudebeck SR (2013) Disentangling Spatial Perception and Spatial Memory in the Hippocampus: A Univariate and Multivariate Pattern Analysis fMRI Study. *J Cogn Neurosci*

25:534–546.

Lee DW, Miyasato LE, Clayton NS (1998) Neurobiological bases of spatial learning in the natural environment: neurogenesis and growth in the avian and mammalian hippocampus. *Neuroreport* **9**:R15-27.

Lee SY, Foldy C, Szabadics J, Soltész I (2011) Cell-Type-Specific CCK2 Receptor Signaling Underlies the Cholecystokinin-Mediated Selective Excitation of Hippocampal Parvalbumin-Positive Fast-Spiking Basket Cells. *J Neurosci* **31**:10993–11002.

Leutgeb JK, Leutgeb S, Moser MB, Moser EI (2007) Pattern separation in the dentate gyrus and CA3 of the hippocampus. *Science* **315**:961–966.

Leutgeb JK, Leutgeb S, Treves A, Meyer R, Barnes CA, McNaughton BL, Moser MB, Moser EI (2005) Progressive transformation of hippocampal neuronal representations in "morphed" environments. *Neuron* **48**:345–348.

Leutgeb S, Leutgeb JK, Treves A, Moser MB, Moser EI (2004) Distinct Ensemble Codes in Hippocampal Areas CA3 and CA1. *Science (80-)* **305**:1295–1298.

Lübke J, Deller T, Frotscher M (1997) Septal innervation of mossy cells in the hilus of the rat dentate gyrus: an anterograde tracing and intracellular labeling study. *Exp brain Res* **114**:423–432.

Lübke J, Frotscher M, Spruston N (1998) Specialized electrophysiological properties of anatomically identified neurons in the hilar region of the rat fascia dentata. *J Neurophysiol* **79**:1518–1534.

Lynch M, Sayin U, Golarai G, Sutula T (2000) NMDA receptor-dependent plasticity of granule cell spiking in the dentate gyrus of normal and epileptic rats. *J Neurophysiol* **84**:2868–2879.

Maguire EA, Burgess N, O'Keefe J (1999) Human spatial navigation: cognitive maps, sexual dimorphism, and neural substrates. *Curr Opin Neurobiol* **9**:171–177.

Maguire EA, Burke T, Phillips J, Staunton H (1996) Topographical disorientation following unilateral temporal lobe lesions in humans. *Neuropsychologia* **34**:993–1001.

Markus EJ, Barnes CA, McNaughton BL, Gladden VL, Skaggs WE (1994) Spatial information content and reliability of hippocampal CA1 neurons: Effects of visual input. *Hippocampus* **4**:410–421.

Marr D (1971) Simple Memory : A Theory for Archicortex. *Philos Trans R Soc Lond B Biol Sci* **262**:23–81.

Marrone DF, Adams AA, Satvat E (2011) Increased pattern separation in the aged fascia dentata. *Neurobiol Aging* **32**:2317.e23-e32.

Mathern GW, Babb TL, Vickrey BG, Melendez M, Pretorius JK (1995) The clinical-pathogenic mechanisms of hippocampal neuron loss and surgical outcomes in temporal lobe epilepsy. *Brain* **118**:105–118.

McNaughton BL, Barnes CA, Meltzer J, Sutherland RJ (1989) Hippocampal granule cells are necessary for normal spatial learning but not for spatially-selective pyramidal cell discharge. *Exp brain Res* **76**:485–496.

McNaughton BL, Barnes CA, Mizumori SJY, Green EJ, Sharp PE (1991) Contribution of granule cells to spatial representations in hippocampal circuits: a puzzle. In: Kindling and Synaptic Plasticity: The Legacy of Graham Goddar (Morrell F, ed), pp 110–123. Boston: Springer-Verlag.

Megías M, Emri Z, Freund TF, Gulyás AI (2001) Total number and distribution of inhibitory and excitatory synapses on hippocampal CA1 pyramidal cells. *Neuroscience* **102**:527–540.

Morris RGM (2006) Elements of a neurobiological theory of hippocampal function: the role of synaptic plasticity, synaptic tagging and schemas. *Eur J Neurosci* **23**:2829–2846.

Motley SE, Kirwan CB (2012) A Parametric Investigation of Pattern Separation Processes in the Medial Temporal Lobe. *J Neurosci* **32**:13076–13084.

Muzzio IA, Kentros C, Kandel E (2009) What is remembered? Role of attention on the encoding and retrieval of hippocampal representations. *J Physiol* **587**:2837–2854.

Myers CE, Scharfman HE (2009) A Role for hilar cells in pattern separation in the dentate gyrus: A computational approach. *Hippocampus* **19**:321–337.

Myers CE, Scharfman HE (2011) Pattern separation in the dentate gyrus: A role for the CA3 backprojection. *Hippocampus* **21**:1190–1215.

Naber PA, Witter MP, Lopez da Silva FH (1999) Perirhinal cortex input to the hippocampus in the rat: evidence for parallel pathways, both direct and indirect. A combined physiological and anatomical study. *Eur J Neurosci* **11**:4119–4133.

Nadel L (1991) The hippocampus and space revisited. *Hippocampus* **1**:221–229.

Nakashiba T, Cushman JD, Pelkey KA, Renaudineau S, Buhl DL, McHugh TJ, Barrera VR, Chittajallu R, Iwamoto KS, McBain CJ, Fanselow MS, Tonegawa S (2012) Young dentate granule cells mediate pattern separation, whereas old granule cells facilitate pattern completion. *Cell* **149**:188–201.

Neuhäuser M (2011) Nonparametric Statistical Tests: A Computational Approach. New York: CRC Press.

Neunuebel JP, Knierim JJ (2012) Spatial Firing Correlates of Physiologically Distinct Cell Types of the Rat Dentate Gyrus. *J Neurosci* **32**:3848–3858.

Nitz D, McNaughton BL (2004) Differential modulation of CA1 and dentate gyrus interneurons during exploration of novel environments. *J Neurophysiol* **91**:863–872.

O'Keefe J, Burgess N, Donnett JG, Jeffery KJ, Maguire EA (1998) Place cells, navigational accuracy, and the human hippocampus. *Philos Trans R Soc B Biol Sci* **353**:1333–1340.

O'Keefe J, Dostrovsky J (1971) The hippocampus as a spatial map. Preliminary evidence from unit activity in the freely-moving rat. *Brain Res* **34**:171–175.

O'Keefe J, Nadel L (1978) The Hippocampus as a Cognitive Map. Oxford University Press.

O'Reilly RC, McClelland JL (1994) Hippocampal Conjunctive Encoding, Storage, and Recall: Avoiding a Trade-Off. *Hippocampus* **4**:661–682.

Olshausen BA, Field DJ (2004) Sparse coding of sensory inputs. *Curr Opin Neurobiol* **14**:481–487.

Park E, Dvorak D, Fenton AA (2011) Ensemble Place Codes in Hippocampus: CA1, CA3, and Dentate Gyrus Place Cells Have Multiple Place Fields in Large Environments Dickson CT, ed. *PLoS One* **6**:e22349.

Pernía-Andrade AJ, Jonas P (2014) Theta-Gamma-Modulated Synaptic Currents in Hippocampal Granule Cells In Vivo Define a Mechanism for Network Oscillations. *Neuron* **81**:140–152.

Petrantonakis PC, Poirazi P (2014) A compressed sensing perspective of hippocampal function. *Front Syst Neurosci* **8**:1–13.

Petrantonakis PC, Poirazi P (2015) Dentate Gyrus Circuitry Features Improve Performance of Sparse Approximation Algorithms Dehghani F, ed. *PLoS One* **10**:e0117023.

Pitkänen A, Pikkarainen M, Nurminen N, Ylinen A (2000) Reciprocal connections between the amygdala and the hippocampal formation, perirhinal cortex, and postrhinal cortex in rat. A review. *Ann N Y Acad Sci* **911**:369–391.

Poirazi P, Brannon T, Mel BW (2003a) Pyramidal Neuron as Two-Layered Neural Network. *Neuron* **37**:989–999.

Poirazi P, Brannon T, Mel BW (2003b) Arithmetic of subthreshold synaptic summation in a model CA1 pyramidal cell. *Neuron* **37**:977–987.

Quirk GJ, Muller RU, Kubie JL, Ranck JB (1992) The positional firing properties of medial entorhinal neurons: description and comparison with hippocampal place cells. *J Neurosci* **12**:1945–1963.

Ratzliff A d H, Howard AL, Santhakumar V, Osapay I, Soltész I (2004) Rapid deletion of mossy cells does not result in a hyperexcitable dentate gyrus: implications for epileptogenesis. *J Neurosci* **24**:2259–2269.

Ratzliff A d H, Santhakumar V, Howard AL, Soltész I (2002) Mossy cells in epilepsy: Rigor mortis or vigor mortis? *Trends Neurosci* **25**:140–144.

Rolls ET (2007) An attractor network in the hippocampus: theory and neurophysiology. *Learn Mem* **14**:714–731.

Roth A, Van Rossum MCW (2009) Modeling synapses. In: Computational modeling methods for neuroscientists (De Shutter E, ed), pp 139–160. Cambridge, MA: MIT press.

Royer S, Zemelman B V, Losonczy A, Kim J, Chance F, Magee JC, Buzsáki G (2012) Control of timing, rate and bursts of hippocampal place cells by dendritic and somatic inhibition. *Nat Neurosci* **15**:769–775.

Santhakumar V, Aradi I, Soltész I (2005) Role of mossy fiber sprouting and mossy cell loss in hyperexcitability: a network model of the dentate gyrus incorporating cell types and axonal topography. *J Neurophysiol* **93**:437–453.

Santoro A (2013) Reassessing pattern separation in the dentate gyrus. *Front Behav Neurosci* **7**:1–4.

Satvat E, Schmidt B, Argraves M, Marrone DF, Markus EJ (2011) Changes in task demands alter the pattern of zif268 expression in the dentate gyrus. *J Neurosci* **31**:7163–7167.

Scharfman HE (1991) Dentate hilar cells with dendrites in the molecular layer have lower thresholds for synaptic activation by perforant path than granule cells. *J Neurosci* **11**:1660–1673.

Scharfman HE (1995) Electrophysiological evidence that dentate hilar mossy cells are excitatory and innervate both granule cells and interneurons. *J Neurophysiol* **74**:179–194.

Scharfman HE (2016) The enigmatic mossy cell of the dentate gyrus. *Nat Rev Neurosci* **17**:562–575.

Scheff SW, Price DA (2003) Synaptic pathology in Alzheimer's disease: A review of ultrastructural studies. *Neurobiol Aging* **24**:1029–1046.

Schlaug G, Jäncke L, Huang Y, Steinmetz H (1995) In vivo evidence of structural brain asymmetry in musicians. *Science* **267**:699–701.

Schmidt-Hieber C, Bischofberger J (2010) Fast sodium channel gating supports localized and efficient axonal action potential initiation. *J Neurosci* **30**:10233–10242.

Schmidt-Hieber C, Jonas P, Bischofberger J (2004) Enhanced synaptic plasticity in newly generated

granule cells of the adult hippocampus. *Nature* **429**:184–187.

Schmidt-Hieber C, Jonas P, Bischofberger J (2007) Subthreshold dendritic signal processing and coincidence detection in dentate gyrus granule cells. *J Neurosci* **27**:8430–8441.

Schneider CJ, Bezaire MJ, Soltész I (2012) Toward a full-scale computational model of the rat dentate gyrus. *Front Neural Circuits* **6**:83.

Sik A, Penttonen M, Buzsáki G (1997) lnterneurons in the Hippocampal Dentate Gyrus : an In Vivo lntracellular Study. *Eur J Neurosci* **9**:573–588.

Skaggs WE, Mcnaughton BL, Markus EJ, Gothard KM (1993) An Information-Theoretic Approach to Deciphering the Hippocampal Code. In: Advances in Neural Information Process Systems (NIPS), 5, 5th ed. (Hanson S, Cowan J, Giles C, eds), pp 1030–1037.

Skaggs WE, McNaughton BL, Wilson MA, Barnes CA (1996) Theta phase precession in hippocampal neuronal populations and the compression of temporal sequences. *Hippocampus* **6**:149–172.

Sloviter RS, Lømo T (2012) Updating the lamellar hypothesis of hippocampal organization. *Front Neural Circuits* **6**:102.

Small SA, Chawla MK, Buonocore M, Rapp PR, Barnes CA (2004) Imaging correlates of brain function in monkeys and rats isolates a hippocampal subregion differentially vulnerable to aging. *Proc Natl Acad Sci U S A* **101**:7181–7186.

Smulders T V, Sasson AD, DeVoogd TJ (1995) Seasonal variation in hippocampal volume in a food-storing bird, the black-capped chickadee. *J Neurobiol* **27**:15–25.

Squire LR, Stark CEL, Clark RE (2004) The medial temporal lobe. *Annu Rev Neurosci* **27**:279–306.

Stachenfeld KL, Botvinick MM, Gershman SJ (2017) The hippocampus as a predictive map. *Nat Neurosci* **20**:1643–1653.

Steward O, Scoville SA (1976) Cells of origin of entorhinal cortical afferents to the hippocampus and fascia dentata of the rat. *J Comp Neurol* **169**:347–370.

Sun Y, Nguyen AQ, Nguyen JP, Le L, Saur D, Choi J, Callaway EM, Xu X (2014) Cell-type-specific circuit connectivity of hippocampal CA1 revealed through cre-dependent rabies tracing. *Cell Rep* **7**:269–280.

Swanson LW (1977) The anatomical organization of septo-hippocampal projections. *Ciba Found Symp*:25–48.

Takács VT, Klausberger T, Somogyi P, Freund TF, Gulyás AI (2012) Extrinsic and local glutamatergic

inputs of the rat hippocampal CA1 area differentially innervate pyramidal cells and interneurons. *Hippocampus* **22**:1379–1391.

Tejada J, Roque AC (2014) Computational models of dentate gyrus with epilepsy-induced morphological alterations in granule cells. *Epilepsy Behav* **38**:63–70.

Tomás Pereira I, Agster KL, Burwell RD (2016) Subcortical connections of the perirhinal, postrhinal, and entorhinal cortices of the rat. I. afferents. *Hippocampus* **26**:1189–1212.

Treves A, Rolls ET (1994) Computational Analysis of the Role of the Hippocampus in Memory. *Hippocampus* **4**:374–391.

Treves A, Tashiro A, Witter MP, Moser EI (2008) What is the mammalian dentate gyrus good for? *Neuroscience* **154**:1155–1172.

Trygve Solstad, Moser EI, Gaute T. Einevoll (2007) From Grid Cells to Place Cells: A Mathematical Model. *Hippocampus* **17**:801–812.

Turi GF, Liao Z, Li W-K, Zaremba JD, Grosmark A, Luo X, Topolnik L, Losonczy A (2016) Role of hippocampal VIP interneurons in reward-oriented spatial learning. **343**:6173.

Tyan L, Chamberland S, Magnin E, Camire O, Francavilla R, David LS, Deisseroth K, Topolnik LT (2014) Dendritic Inhibition Provided by Interneuron-Specific Cells Controls the Firing Rate and Timing of the Hippocampal Feedback Inhibitory Circuitry. *J Neurosci* **34**:4534–4547.

Ulanovsky N, Moss CF (2007) Hippocampal cellular and network activity in freely moving echolocating bats. *Nat Neurosci* **10**:224–233.

van Praag H, Kempermann G, Gage FH (2000) Neural consequences of environmental enrichment. *Nat Rev Neurosci* **1**:191–198.

Varga V, Losonczy A, Zemelman B V, Borhegyi Z, Nyiri G, Domonkos A, Hangya B, Holderith N, Magee JC, Freund TF (2009) Fast synaptic subcortical control of hippocampal circuits. *Science* **326**:449–453.

Vertes RP, Hoover WB, Do Valle AC, Sherman A, Rodriguez JJ (2006) Efferent projections of reuniens and rhomboid nuclei of the thalamus in the rat. *J Comp Neurol* **499**:768–796.

Vida I (2010) Morphology of Hippocampal Neurons. In: Hippocampal microcircuits: A Computational Modeler's Resource Book (Cutsuridis V, Graham BP, Cobb S, Vida I, eds), pp 27–67. New York: Springer.

Vorhees C V., Williams MT (2014) Assessing Spatial Learning and Memory in Rodents. *ILAR J* **55**:310–

332.

West MJ, Kawas CH, Martin LJ, Troncoso JC (2006) The CA1 Region of the Human Hippocampus Is a Hot Spot in Alzheimer's Disease. *Ann N Y Acad Sci* **908**:255–259.

West MJ, Slomianka L, Gundersen HJ (1991) Unbiased stereological estimation of the total number of neurons in thesubdivisions of the rat hippocampus using the optical fractionator. *Anat Rec* **231**:482–497.

Williams PA, Larimer P, Gao Y, Strowbridge BW (2007) Semilunar granule cells: glutamatergic neurons in the rat dentate gyrus with axon collaterals in the inner molecular layer. *J Neurosci* **27**:13756–13761.

Witter MP (2007) Intrinsic and extrinsic wiring of CA3: Indications for connectional heterogeneity. *Learn Mem* **14**:705–713.

Witter MP, Amaral DG (2004) The rat nervous system. In: Hippocampal formation (Paxinos G, ed), pp 635–704. San Diego: Elsevier Academic Press.

Wittner L, Henze DA, Záborszky L, Buzsáki G (2006) Hippocampal CA3 pyramidal cells selectively innervate aspiny interneurons. *Eur J Neurosci* **24**:1286–1298.

Yassa MA, Stark CEL (2011) Pattern separation in the hippocampus. *Trends Neurosci* **34**:515–525.

Yim MY, Hanuschkin A, Wolfart J (2015) Intrinsic rescaling of granule cells restores pattern separation ability of a dentate gyrus network model during epileptic hyperexcitability. *Hippocampus* **25**:297–308.

Zaremba JD, Diamantopoulou A, Danielson NB, Grosmark AD, Kaifosh PW, Bowler JC, Liao Z, Sparks FT, Gogos JA, Losonczy A (2017) Impaired hippocampal place cell dynamics in a mouse model of the 22q11.2 deletion. *Nat Neurosci*:1–64.

Zeidman P, Maguire EA (2016) Anterior hippocampus: the anatomy of perception, imagination and episodic memory. *Nat Rev Neurosci* **17**:173–182.

APPENDIX A – Grid like inputs mathematical formalization

In our model the net somatic potential in a hippocampal cell is expressed as a weighted sum of excitatory inputs from a set of *N* grid cells and some additional inhibitory inputs. The grid-cell functions are constructed from a sum of three two-dimensional sinusoidal grating, specified by their wave vectors. The grid-like functions are given in the following equation:

$$g_{\boldsymbol{w}}(x,y) = \frac{2}{3}\left(\frac{1}{3}\sum_{i=1}^{3} cos\big(\boldsymbol{k}_i(\boldsymbol{r}-\boldsymbol{r}_0)\big) + \frac{1}{2}\right)$$

where the subscript $w = (\lambda, \theta, r_0)$ specifies the spacing λ, the orientation θ, and the spatial position of the theoretical place cell $\boldsymbol{r}_0 = [x_0, y_0]^{\mathrm{T}}$ of the contributing grid cells, $\boldsymbol{r} = [x, y]^{\mathrm{T}}$ is the current position, and $\boldsymbol{k}$ denotes the wave vectors with $\frac{\pi}{3}$ and $\frac{2\pi}{3}$ angular differences, respectively.

$$k_i = \frac{1}{\lambda}\left[\cos\left(\theta + (i-1)\frac{\pi}{3}\right), \sin\left(\theta + (i-1)\frac{\pi}{3}\right)\right]^{\mathrm{T}}$$

The grid-like functions thus return the probability of generating a spike given the current position of the animal and the theoretical place field which we want to build.

Finally, we pass a sinusoidal filter in the abovementioned probabilities in order to take into account the theta modulation found in the hippocampal formation.

$$p(t) = g_{\boldsymbol{w}}(x,y)\frac{sin(2\pi \cdot f_{theta} \cdot \left(\frac{t}{1000}\right) + \varphi_{theta}) + 1}{2}$$

where $f_{theta} = 8\,Hz$ and $\varphi_{theta} = 0$ degrees denoting the theta-cycle frequency and phase, respectively, and *t* is the time in ms. If the probability $p(t)$ is greater than 0.7 a spike is generated for this specific grid-like cell. The process is repeated for all grid-like cells and for all theoretical place-fields. For any octal of grid-like cells we start with $\lambda = 3.0$ and $\theta = 0.0$ for the first cell and for any other cell belonging in the same octal its spacing and its orientation are increased by 0.5 and 0.4, respectively.

APPENDIX B – Ionic Channels used in CA1 model (Hodgkin-Huxley formalization)

Pyramidal Neurons

Pyramidal neurons consisted of various compartments such as soma, axon, radiatum (rad), lacunosum-moleculare (lm) and oriens (ori). Each compartment was governed by the following differential equations:

$$C_m \frac{dV_{soma}}{dt} = -\left(I_L + I_{Na} + I_{K_{dr}} + I_A + I_M + I_h + I_{sAHP} + I_{mAHP} + I_{CaL} + I_{CaR} + I_{CaT} + I_{buff} + I_{syn}\right)$$

$$C_m \frac{dV_{axon}}{dt} = -\left(I_L + I_{Na} + I_{K_{dr}} + I_M + I_{syn}\right)$$

$$C_m \frac{dV_{rad}}{dt} = -\left(I_L + I_{Na} + I_{K_{dr}} + I_A + I_M + I_h + I_{sAHP} + I_{mAHP} + I_{CaL} + I_{CaR} + I_{CaT} + I_{buff} + I_{syn}\right)$$

$$C_m \frac{dV_{lm}}{dt} = -\left(I_L + I_{Na} + I_{K_{dr}} + I_A + I_{syn}\right)$$

$$C_m \frac{dV_{ori}}{dt} = -\left(I_L + I_{Na} + I_{K_{dr}} + I_A + I_M + I_h + I_{sAHP} + I_{mAHP} + I_{CaL} + I_{CaR} + I_{CaT} + I_{buff} + I_{syn}\right)$$

where C_m is the membrane capacitance, V the membrane potential, I_L is the leak current, I_{Na} the fast sodium current, I_{Kdr} the delayed rectifier potassium current, I_A the A-type K^+ current, I_M the M-type K^+ current, I_h the hyperpolarizing h-type current, I_{CaL}, I_{CaR} and I_{CaT} the L-, R- and T-type Ca^{2+} currents, I_{sAHP} and I_{mAHP} the slow and medium Ca^{2+} activated K^+ currents, I_{buff} the calcium pump/buffering mechanism and I_{syn} the synaptic current.

The sodium current is described by:

$$I_{Na} = \bar{g}_{Na} \cdot m^2 \cdot h \cdot s \cdot (V - E_{Na})$$

where the extra variable s accounts for the dendritic location-dependent slow attenuation of the sodium current (Poirazi et al, 2003,a,b). The activation and inactivation parameters are given by:

$$m_{t+dt} = m_t + \left(1 + e^{-\frac{dt}{\tau_m}}\right) \cdot (m_\infty - m_t),\ \ m_\infty = \frac{1}{1 + e^{-\frac{V+40}{3}}},\ \ \tau_m = 0.05\ ms$$

$$h_{t+dt} = h_t + \left(1 + e^{-\frac{dt}{\tau_h}}\right) \cdot (h_\infty - h_t),\ \ h_\infty = \frac{1}{1 + e^{\frac{V+45}{3}}},\ \ \tau_h = 0.5\ ms$$

$$s_{t+dt} = s_t + \left(1 + e^{-\frac{dt}{\tau_s}}\right) \cdot (s_\infty - s_t), s_\infty = \frac{1 + (Na_{att}) e^{\frac{V+60}{2}}}{1 + e^{\frac{V+60}{2}}}$$

The time constant τ_s is given by the following equation:

$$\tau_s = \frac{0.00333(ms) e^{0.0024\left(mV^{-1}\right)(V+60)Q(\theta)}}{1 + e^{0.0012(mV^{-1})(V+60)Q(\theta)}}, Q(\theta) = \frac{F}{R(T+\theta)}$$

where $R = 8.315\ Joule/^oC$, $F = 9.648 \cdot 10^4\ Coulomb/mole$, $T = 273.16\ Kelvin$ and θ the temperature in degrees of ^oC. The N_{aatt} represents the attenuation of sodium current and varies linearly as function of distance from the soma, and takes values within range [0, 1] with zero denoting the maximum and one the minimum attenuation.

The delayed rectifier potassium current is governed by the equation:

$$I_{K_{dr}} = \bar{g}_{K_{dr}} \cdot m^2 \cdot (V - E_K)$$

The activation parameter is given by:

$$m_{t+dt} = m_t + \left(1 + e^{-\frac{dt}{\tau_m}}\right) \cdot (m_\infty - m_t),\ \ m_\infty = \frac{1}{1 + e^{\frac{V+42}{2}}},\ \ \tau_m = 2.2\ ms$$

The sodium and delayed rectifier channel properties are slightly different in the soma and axon comparing with the dendritic arbor (given above). To fit experimental data regarding the backpropagation of spike trains, soma and axon compartments have a lower threshold for Na^+ spike initiation (~ -57 mV) than dendritic ones (~ -50 mV). Thus, the activation and inactivation parameters for soma and axon were modified as follows.

For sodium channel

$$m_\infty = \frac{1}{1 + e^{-\frac{V+44}{3}}}, \;\; \tau_m = 0.05\, ms$$

$$h_\infty = \frac{1}{1 + e^{\frac{V+49}{3.5}}}, \;\; \tau_h = 1.0\, ms$$

For delayed rectifier channel

$$m_\infty = \frac{1}{1 + e^{-\frac{V+46.3}{3}}}, \;\; \tau_m = 3.5\, ms$$

The fast inactivating A-type K^+ current is described by:

$$I_A = \bar{g}_A \cdot n \cdot l \cdot (V - E_K)$$

The corresponding activation and inactivation parameters are given from equations below:

$$n_{t+dt} = n_t + \left(1 + e^{-\frac{dt}{\tau_n}}\right) \cdot (n_\infty - n_t), \;\; n_\infty = \frac{a_n}{a_n + \beta_n}, \;\; \tau_n = 0.2\, ms$$

$$a_n = \frac{-0.01(V + 21.3)}{e^{-\frac{V+21.3}{35}} - 1}, \;\; \beta_n = \frac{0.01(V + 21.3)}{e^{\frac{V+21.3}{35}} - 1}$$

$$l_{t+dt} = l_t + \left(1 + e^{-\frac{dt}{\tau_l}}\right) \cdot (l_\infty - l_t), \;\; n_\infty = \frac{a_l}{a_l + \beta_l}$$

$$\tau_l = 5 + 26\frac{V + 20}{10} \; if \; V > 20\, mV \; and \; \tau_l = 5\, ms \; elsewhere$$

$$a_l = \frac{-0.01(V + 58)}{e^{\frac{V+58}{8.2}} - 1}, \;\; \beta_l = \frac{0.01(V + 58)}{e^{-\frac{V+58}{8.2}} - 1}$$

The slowly activating voltage-dependent potassium current is given by the equations:

$$I_M = \bar{g}_M \cdot m \cdot 10^{-4} \cdot T_{adj}(\theta) \cdot (V - E_K), \;\; T_{adj}(\theta) = 2.3^{\left(\frac{\theta-23}{10}\right)}$$

And the corresponding activation parameter is governed by the following equations:

$$m_{t+dt} = m_t + \left(1 + e^{-\frac{dt \cdot T_{adj}(\theta)}{\tau_m}}\right) \cdot (m_\infty - m_t),\ \ m_\infty = \frac{a_m}{a_m + \beta_m},\ \ \tau_m = \frac{1}{a_m + \beta_m}$$

$$a_m = \frac{0.001(V+30)}{1 - e^{-\frac{V+30}{9}}},\ \ \beta_m = \frac{-0.001(V+30)}{1 - e^{\frac{V+30}{9}}}$$

The hyperpolarizing h-current is given by

$$I_h = \bar{g}_h \cdot tt \cdot (V - E_h)$$

The activation parameter is given by

$$tt_{t+dt} = tt_t + \left(1 + e^{-\frac{dt}{\tau_{tt}}}\right) \cdot (tt_\infty - tt_t),\ \ tt_\infty = \frac{1}{1 + e^{-\frac{V - V_{half}}{k_l}}},\ \ \tau_{tt} = \frac{e^{0.0378} \cdot \zeta \cdot gmt \cdot \left(V - V_{half}\right)}{qtl \cdot q10^{\frac{T-33}{10}} \cdot a0t \cdot (1 + a_{tt})}$$

$$a_{tt} = e^{0.00378 \cdot \zeta \cdot \left(V - V_{half}\right)}$$

where ζ, qtl and $q10$ are 2.2, 0.4, 1.0 and 4.5 respectively. The a0t is $0.00111\ ms^{-1}$, $V_{half} = -75\ mV$ and $k_l = -8$.

The slow after-hyperpolarizing current is given by

$$I_{sAHP} = \bar{g}_{sAHP} \cdot m^3 \cdot (V - E_K)$$

$$\frac{dm}{dt} = \frac{\frac{Cac}{1 + Cac} - m}{\tau_m},\ \ \tau_m = \max\left(\frac{1}{0.003ms^{-1} \cdot (1 + Cac) \cdot 3^{\frac{\theta - 22}{10}}}, 0.5\right), Cac = \left(\frac{ca_{in}}{0.025mM}\right)^2$$

The medium after-hyperpolarizing current is given by:

$$I_{mAHP} = \bar{g}_{mAHP} \cdot o \cdot (V - E_K)$$

$$o_{t+dt} = o_t + \left(1 + e^{-\frac{dt}{\tau_o}}\right) \cdot (o_\infty - o_t),\ \ o_\infty = a_o \cdot \tau_o,\ \ \tau_o = \frac{1}{a_o + \beta_o}$$

$$a_o = \frac{0.48ms^{-1}}{1 + \frac{0.18mM}{ca_{in}} \cdot e^{-1.68 \cdot V \cdot Q(\theta)}},\ \ \beta_o = \frac{0.28ms^{-1}}{1 + \frac{ca_{in}}{0.011mM \cdot e^{2.0 \cdot V \cdot Q(\theta)}}}$$

The somatic high-voltage activated (HVA) L-type Ca^{2+} current is described by

$$I_{CaL} = \bar{g}_{CaL} \cdot m \cdot \frac{0.001mM}{0.001mM + ca_{in}} \cdot ghk(V, ca_{in}, ca_{out})$$

$$m_{t+dt} = m_t + \left(1 + e^{-\frac{dt}{\tau_m}}\right) \cdot (m_\infty - m_t), \;\; m_\infty = \frac{a_m}{\tau_m}, \;\; \tau_m = \frac{1}{5(a_m + \beta_m)}$$

$$a_m = \frac{-0.055 \cdot (V + 27.01)}{e^{-\frac{V+27.01}{3.8}} - 1}, \;\; \beta_m = 0.94 \cdot e^{-\frac{V+63.01}{17}}$$

while the dendritic L-type calcium channels are given by

$$I_{CaL} = \bar{g}_{CaL} \cdot m^3 \cdot h \cdot (V - E_{Ca})$$

$$m_{t+dt} = m_t + \left(1 + e^{-\frac{dt}{\tau_m}}\right) \cdot (m_\infty - m_t), \;\; m_\infty = a_m, \;\; \tau_m = 3.6\, ms$$

$$h_{t+dt} = h_t + \left(1 + e^{-\frac{dt}{\tau_h}}\right) \cdot (h_\infty - h_t), \;\; h_\infty = a_h, \;\; \tau_h = 29\, ms$$

$$a_{m,h} = \frac{1}{e^{-(V+37)} + 1}, \;\; \beta_{m,h} = \frac{1}{e^{\frac{(V+41)}{0.5}} + 1}$$

The function *ghk* is calculated from the following set of equations:

$$ghk(V, ca_{in}, ca_{out}) = -x \cdot \left(1 - \frac{ca_{in}}{ca_{out}} \cdot e^{\frac{V}{x}}\right) \cdot f\left(\frac{V}{x}\right)$$

$$x = \frac{0.0853 \cdot (T + \theta)}{2}, \;\; f(z) = \begin{cases} 1 - \frac{z}{2} \; if \; |z| < 10^{-4} \\ \frac{z}{e^z - 1} \; otherwise \end{cases}$$

and ca_{in} and ca_{out} are the internal and external calcium concentrations, respectively.

The HVA R-type Ca^{2+} current is described by

$$I_{CaR} = \bar{g}_{CaR} \cdot m^3 \cdot h \cdot (V - E_{Ca})$$

$$m_{t+dt} = m_t + \left(1 + e^{-\frac{dt}{\tau_m}}\right) \cdot (m_\infty - m_t), \;\; m_\infty = a_m$$

$$h_{t+dt} = h_t + \left(1 + e^{-\frac{dt}{\tau_h}}\right) \cdot (h_\infty - h_t), \;\; h_\infty = a_h$$

For the somatic compartment, τ_m = 100 ms and τ_h = 5 ms, while for the dendritic compartments $\tau_m = 50\ ms$ and $\tau_h = 5\ ms$. The alpha and beta parameters for the somatic compartments are given by

$$a_{m,h} = \frac{1}{e^{-\frac{(V+60)}{3}} + 1}, \;\; \beta_{m,h} = \frac{1}{e^{(V+62)} + 1}$$

whereas for the dendritic compartments by

$$a_{m,h} = \frac{1}{e^{-\frac{(V+48.5)}{3}} + 1}, \;\; \beta_{m,h} = \frac{1}{e^{(V+53)} + 1}$$

The low-voltage activation (LVA) T-type Ca^{2+} current is given by

$$I_{CaT} = \bar{g}_{CaT} \cdot m^2 \cdot h \cdot \frac{0.001mM}{0.001mM + ca_{in}} \cdot ghk(V, ca_{in}, ca_{out})$$

$$m_{t+dt} = m_t + \left(1 + e^{-\frac{dt \cdot T_{adj}(\theta)}{\tau_m}}\right) \cdot (m_\infty - m_t), \;\; m_\infty = \frac{a_m}{a_m + \beta_m}, \;\; \tau_m = \frac{1}{a_m + \beta_m}$$

$$a_m = \frac{-0.196(V - 19.88)}{e^{-\frac{V-19.88}{10}} - 1}, \;\; \beta_m = 0.046 \cdot e^{-\frac{V}{22.73}}$$

$$h_{t+dt} = m_t + \left(1 + e^{-\frac{dt \cdot T_{adj}(\theta)}{\tau_h}}\right) \cdot (h_\infty - h_t), \;\; h_\infty = \frac{a_h}{a_h + \beta_h}, \;\; \tau_h = \frac{1}{0.68 \cdot (a_h + \beta_h)}$$

$$a_h = 0.00016 \cdot e^{-\frac{V+57}{19}}, \;\; \beta_h = \frac{1}{1 + e^{-\frac{V-15}{10}}}$$

Finally, a calcium pump/buffering mechanism is inserted at the cell soma and along the apical and basal trunk. The kinetic equations are given by

$$drive_{channel} = max\left(-f^e \cdot \frac{I_{Ca}}{0.2 \cdot F}, 0\right), f^e = 555.55, F = 9.648 \cdot 10^4 \text{ Coulomb}$$

$$\frac{dca}{dt} = \frac{drive_{channel}}{18} + \frac{10^{-4}mM - ca}{1400ms}$$

Interneurons

Axoaxonic, Basket, Bistratified and VIP$^+$/CCK$^+$ cells

All compartments of AAC, BC, BSC and VIPCCK are described by the following current equation:

$$C_m \frac{dV}{dt} = -\left(I_L + I_{Na} + I_{K_{dr},fast} + I_{K_{dr},slow} + I_A + I_{CaL} + I_{CaN} + I_C + I_{AHP} + I_{syn}\right)$$

where C_m is the membrane capacitance, V the membrane potential, I_L is the leak current, I_{Na} the sodium current, $I_{Kdr,fast}$ the fast delayed rectifier potassium current, I_A the A-type K^+ current, I_{CaL} and I_{CaN} the L- and N-type Ca^{2+} currents, I_C is the Ca^{2+}-dependent K^+ current (SK), I_{AHP} the calcium and voltage dependent K^+ current (BK), and I_{syn} the synaptic current.

The sodium current is given by:

$$I_{Na} = \bar{g}_{Na} \cdot m^3 \cdot h \cdot (V - E_{Na})$$

$$\frac{dm}{dt} = a_m \cdot (1 - m) - \beta_m \cdot m, \;\; a_m = \frac{-0.3 \cdot (V - 25)}{1 - e^{-\frac{(V-25)}{5}}}, \;\; \beta_m = \frac{0.3 \cdot (V - 53)}{1 - e^{\frac{(V-53)}{5}}}$$

$$\frac{dh}{dt} = a_h \cdot (1 - h) - \beta_h \cdot h, \;\; a_h = \frac{0.23}{e^{\frac{(V-3)}{20}}}, \;\; \beta_m = \frac{3.33}{1 + e^{-\frac{(V-55.5)}{10}}}$$

The fast delayed rectifier current is described by:

$$I_{K_{dr},fast} = \bar{g}_{K_{dr},fast} \cdot n_f^4 \cdot (V - E_K)$$

$$\frac{dn_f}{dt} = a_{n_f} \cdot (1 - n_f) - \beta_{n_f} \cdot n_f, \;\; a_{n_f} = \frac{-0.07 \cdot (V - 47)}{1 - e^{-\frac{(V-47)}{6}}}, \;\; \beta_{n_f} = 0.264 \cdot e^{\frac{V-22}{4}}$$

While the slow delayed rectifier current by:

The fast delayed rectifier current is described by:

$$I_{K_{dr},slow} = \bar{g}_{K_{dr},slow} \cdot n_s^4 \cdot (V - E_K)$$

$$\frac{dn_s}{dt} = a_{n_s} \cdot (1 - n_s) - \beta_{n_s} \cdot n_s, \;\; a_{n_s} = \frac{-0.028 \cdot (V + 22)}{1 - e^{-\frac{(V+22)}{-5}}}, \;\; \beta_{n_s} = \frac{0.1056}{e^{\frac{(V+25)}{40}}}$$

The A-type K^+ current is described by:

$$I_A = \bar{g}_A \cdot a \cdot b \cdot (V - E_K)$$

$$\frac{da}{dt} = a_a \cdot (1 - a) - \beta_a \cdot a, \;\; a_a = \frac{0.02 \cdot (13.1 - V)}{e^{\frac{(13.1-V)}{10}} - 1}, \;\; \beta_a = \frac{0.0175 \cdot (V - 40.1)}{e^{\frac{(V-40.1)}{10}} - 1}$$

$$\frac{db}{dt} = a_b \cdot (1 - b) - \beta_b \cdot b, \;\; a_b = 0.0016 \cdot e^{-\frac{V+13}{18}}, \;\; \beta_b = \frac{0.05}{e^{\frac{(10.1-V)}{5}} + 1}$$

The N-type Ca^{2+} current is given by:

$$I_{CaN} = \bar{g}_{CaN} \cdot c^2 \cdot d \cdot (V - E_{Ca})$$

$$\frac{dc}{dt} = a_c \cdot (1 - c) - \beta_c \cdot c, \;\; a_c = \frac{0.19 \cdot (19.88 - V)}{e^{\frac{(19.88-V)}{10}} - 1}, \;\; \beta_c = 0.046 \cdot e^{-\frac{V}{20.73}}$$

$$\frac{dd}{dt} = a_d \cdot (1 - d) - \beta_d \cdot d, \;\; a_d = 0.0016 \cdot e^{-\frac{V}{48.4}}, \;\; \beta_d = \frac{1}{e^{\frac{(39-V)}{10}} - 1}$$

The L-type Ca^{2+} current is given by:

$$I_{CaL} = \bar{g}_{CaL} \cdot m^2 \cdot h2(ca_{in}) \cdot ghk(V, ca_{in}, ca_{out}),\ \ h2(ca_{in}) = \frac{k_i}{k_i + ca_{in}}$$

$$\frac{dm}{dt} = \frac{m_\infty - m}{\tau_m},\ \ m_\infty = a_m \cdot \tau_m,\ \ \tau_m = \frac{1}{a_m + \beta_m}$$

$$a_m = \frac{15.69 \cdot (81.5 - V)}{e^{\frac{(81.5-V)}{10}} - 1},\ \ \beta_m = 0.29 \cdot e^{-\frac{V}{10.86}}$$

As in the previous section, the function ghk is given below:

$$ghk(V, ca_{in}, ca_{out}) = -x \cdot \left(1 - \frac{ca_{in}}{ca_{out}} \cdot e^{\frac{V}{x}}\right) \cdot f\left(\frac{V}{x}\right)$$

$$x = \frac{0.0853 \cdot (T + \theta)}{2},\ \ f(z) = \begin{cases} 1 - \frac{z}{2}\ if\ |z| < 10^{-4} \\ \frac{z}{e^z - 1}\ otherwise \end{cases}$$

where ca_{in} and ca_{out} are the internal and external calcium concentrations, respectively and $k_i = 0.001\ mM$.

The calcium and voltage dependent K^+ current (BK) is described by:

$$I_{AHP} = \bar{g}_{AHP} \cdot o \cdot (V - E_K)$$

$$o_{t+1} = o_t + \left(1 - e^{-\frac{dt}{\tau_o}}\right) \cdot (o_\infty - o),\ \ o_\infty = a_o \cdot \tau_o,\ \ \tau_o = \frac{1}{a_o + \beta_o}$$

$$a_o = \frac{0.48ms^{-1}}{1 + \frac{0.18mM}{ca_{in}} \cdot e^{-1.68 \cdot V \cdot Q(\theta)}},\ \ \beta_o = \frac{0.28ms^{-1}}{1 + \frac{ca_{in}}{0.011mM \cdot e^{2.0 \cdot V \cdot Q(\theta)}}}$$

The Ca^{2+}-dependent K^+ current is described by:

$$I_C = \bar{g}_C \cdot q^2 \cdot (V - E_K)$$

$$\frac{dq}{dt} = a_q \cdot (1-q) - \beta_q \cdot q, \;\; a_q = \frac{0.00246}{e^{-\frac{(12 \cdot \log_{10}([Ca^{2+}])+28.48)}{4.5}}}, \;\; \beta_c = \frac{0.006}{e^{\frac{(12 \cdot \log_{10}([Ca^{2+}])+60.4)}{35}}}$$

$$\frac{d[Ca^{2+}]_i}{dt} = \frac{5.2 \cdot 10^{-6}}{A \cdot d}\left(\frac{mol}{C \cdot m^3}\right)\sum_{T,N,L} I_{Ca} - \frac{[Ca^{2+}]_i - [Ca^{2+}]_o}{\tau}$$

where A is the surface area, d is the thickness, $\tau = 10\, ms$ is the calcium removal rate, and $[Ca^{2+}]_o = 5\, \mu M$ the resting calcium concentration.

O-LM cells

The OLM soma, axon and dendrites are described by the following equations:

$$C_m \frac{dV_{soma}}{dt} = -\left(I_L + I_{Na} + I_K + I_A + I_h + I_{syn}\right)$$

$$C_m \frac{dV_{axon}}{dt} = -(I_L + I_{Na} + I_K)$$

$$C_m \frac{dV_{dend}}{dt} = -\left(I_L + I_{Na} + I_K + I_A + I_{syn}\right)$$

Where Cm is the membrane capacitance, V the membrane potential, I_L the leak current, I_{NA} and I_K are the sodium and potassium currents, respectively. Additionally, I_A is A-type K^+ current, I_h the nonspecific cation current and I_{syn} the synaptic current.

The sodium current is given by:

$$I_{Na} = \bar{g}_{Na} \cdot m^3 \cdot h \cdot (V - E_{Na})$$

$$\frac{dm}{dt} = a_m \cdot (1-m) - \beta_m \cdot m, \;\; \frac{dh}{dt} = a_h \cdot (1-h) - \beta_h \cdot h$$

$$a_m^{soma,axon} = \frac{-0.1 \cdot (V+38)}{e^{-\frac{(V+38)}{10}} - 1}, \quad \beta_m^{soma,axon} = 4.0 \cdot e^{-\frac{V+63}{18}}$$

$$a_h^{soma,axon} = 0.07 \cdot e^{-\frac{V+63}{20}}, \quad \beta_h^{soma,axon} = \frac{1}{1 + e^{-\frac{(V+33)}{10}}}$$

$$a_m^{dend} = \frac{-0.1 \cdot (V+45)}{e^{-\frac{(V+45)}{10}} - 1}, \quad \beta_m^{dend} = 4.0 \cdot e^{-\frac{V+70}{18}}$$

$$a_h^{dend} = 0.07 \cdot e^{-\frac{V+70}{20}}, \quad \beta_h^{dend} = \frac{1}{1 + e^{-\frac{(V+40)}{10}}}$$

The potassium current is given by:

$$I_{Na} = \bar{g}_{Na} \cdot n^4 \cdot (V - E_K)$$

$$\frac{dn}{dt} = a_n \cdot (1-n) - \beta_n \cdot n$$

$$a_n^{soma,axon} = \frac{-0.018 \cdot (V-25)}{e^{-\frac{(V-25)}{25}} - 1}, \quad \beta_n^{soma,axon} = \frac{0.0036 \cdot (V-35)}{e^{\frac{(V-35)}{12}} - 1}$$

$$a_n^{dend} = \frac{-0.018 \cdot (V-20)}{e^{-\frac{(V-20)}{21}} - 1}, \quad \beta_n^{dend} = \frac{0.0036 \cdot (V-30)}{e^{\frac{(V-30)}{12}} - 1}$$

The transient potassium current is given by:

$$I_A = \bar{g}_A \cdot a \cdot b \cdot (V - E_K)$$

$$\frac{da}{dt} = \frac{a_\infty - a}{\tau_\alpha}, \quad a_\infty = \frac{1}{1 + e^{-\frac{(V+14)}{16.6}}}, \quad \tau_a = 5\ ms$$

$$\frac{db}{dt} = \frac{b_\infty - b}{\tau_b}, \quad b_\infty = \frac{1}{1 + e^{\frac{(V+71)}{7.3}}}, \quad \tau_b = \frac{1}{a_b - \beta_b}$$

$$a_b = \frac{9 \cdot 10^{-6}}{e^{\frac{V-26}{18.5}}}, \quad \beta_b = \frac{0.014}{0.2 + e^{-\frac{V+70}{11}}}$$

The non-specific cation channel is described by:

$$I_h = \bar{g}_h \cdot r \cdot (V - E_r)$$

$$\frac{dr}{dt} = \frac{r_\infty - r}{\tau_r}, \quad r_\infty = \frac{1}{1 + e^{\frac{(V+84)}{10.2}}}, \quad \tau_r = \frac{1}{e^{(-17.9-0.116 \cdot V)} + e^{(-1.84+0.09 \cdot V)}} + 100$$

VIP$^+$/CR$^+$ cells

The VIP/CR compartments are governed by the following equations:

$$C_m \frac{dV}{dt} = -\left(I_L + I_{Na} + I_{K_{dr}} + I_{K_{dr},slow} + I_D + I_{CaN} + I_{AHP} + I_{buff} + I_{syn}\right)$$

Where C_m is the membrane capacitance, V the membrane potential, I_L the leak current, I_{Na} and I_K are the sodium and potassium currents, respectively. Additionally, I_D is the A-type K^+ current, I_{AHP} the Ca^{2+}-dependent K^+ current, the I_{buff} a calcium pump/buffer and I_{syn} the synaptic current.

The fast sodium current is given by:

$$I_{Na} = \bar{g}_{Na} \cdot m^3 \cdot h \cdot (V - E_{Na})$$

$$\frac{dm}{dt} = \frac{m_\infty - m}{\tau_m}, \quad m_\infty = \frac{a_m}{a_m + \beta_m}, \quad \tau_m = \frac{1}{a_m + \beta_m}$$

$$a_m = \frac{-0.2816 \cdot (V + 28)}{e^{-\frac{(V+28)}{9.3}} - 1}, \quad \beta_m = \frac{0.2464 \cdot (V + 1)}{e^{\frac{(V+1)}{6}} - 1}$$

$$\frac{dh}{dt} = \frac{h_\infty - h}{\tau_h}, \quad h_\infty = \frac{a_h}{a_h + \beta_h}, \quad \tau_h = \frac{1}{a_h + \beta_h}$$

$$a_h = \frac{0.098 \cdot (V + 28)}{e^{\frac{(V+23.1)}{20}}}, \quad \beta_h = \frac{1.4 \cdot (V + 1)}{e^{-\frac{(V+25.1)}{10}} + 1}$$

The delayed rectifier potassium current is given by:

$$I_K = \bar{g}_K \cdot m^4 \cdot (V - E_K)$$

$$\frac{dm}{dt} = \frac{m_\infty - m}{\tau_m}, \quad m_\infty = \frac{a_m}{a_m + \beta_m}, \quad \tau_m = \frac{1}{a_m + \beta_m}$$

$$a_m = \frac{-0.018 \cdot (V - 13)}{e^{-\frac{(V-13)}{25}} - 1}, \quad \beta_m = \frac{0.0054 \cdot (V - 23)}{e^{\frac{(V-23)}{12}} - 1}$$

The fast Ca^{2+}- and voltage-dependent K^+ current is given by:

$$I_{AHP} = \bar{g}_{AHP} \cdot c^2 \cdot (V - E_K)$$

$$\frac{dc}{dt} = \frac{c_\infty - c}{\tau_c}, \quad c_\infty = \frac{a_c}{a_c + \beta_c}, \quad \tau_c = \max\left(\frac{1}{a_c + \beta_c}, 1.1\right)$$

$$a_c = \frac{-0.00642 \cdot (V + \log_{10}(1000 \cdot [ca_i])) - 0.1152}{e^{-\frac{(V+18)}{12}} - 1}, \quad \beta_c = 1.7 \cdot e^{-\frac{V+40 \cdot \log_{10}(1000 \cdot [ca_i]) + 152}{3}}$$

The slowly inactivation K^+ current is described by:

$$I_{K_{slow}} = \bar{g}_{K_{slow}} \cdot a \cdot b \cdot (V - E_K)$$

$$\frac{da}{dt} = \frac{a_\infty - a}{\tau_\alpha}, \quad a_\infty = \frac{1}{1 + e^{-\frac{(V+34)}{6.5}}}, \quad \tau_a = 10\ ms$$

$$\frac{db}{dt} = \frac{b_\infty - b}{\tau_b}, \quad b_\infty = \frac{1}{1 + e^{\frac{(V+65)}{6.6}}}, \quad \tau_b = \frac{3200}{1 + e^{-\frac{(V+63.6)}{4}}}$$

The N-type Ca^{2+} current is described by:

$$I_{CaN} = \bar{g}_{CaN} \cdot m^2 \cdot h \cdot h2(ca_i) \cdot (V - E_{Ca}), \quad h2(ca_i) = \frac{k_i}{k_i + ca_i}$$

$$\frac{dm}{dt} = \frac{m_\infty - m}{\tau_m}, \quad m_\infty = \frac{1}{1 + a_m}, \quad \tau_m = 1.5\ ms$$

$$a_m = e^{0.001 \cdot \zeta_m \cdot (V - V_{half_m}) \cdot Q(\theta)}$$

$$\frac{dh}{dt} = \frac{h_\infty - h}{\tau_h}, \quad h_\infty = \frac{1}{1 + a_h}, \quad \tau_h = 75\ ms$$

$$a_h = e^{0.001 \cdot \zeta_h \cdot \left(V - V_{half_h}\right) \cdot Q(\theta)}$$

Where $k_i = 0.025\, mM$, $V_{half,h}$ and $V_{half,m}$ are -21 and $-40\, mV$ respectively, and ζ_m and ζ_h are -3.4 and 2.0 respectively. The temperature function $Q(\theta)$ is given from the formula that mentioned before.

The D-type K^+ current is given by:

$$I_D = \bar{g}_D \cdot n \cdot l \cdot (V - E_K)$$

$$\frac{dn}{dt} = \frac{n_\infty - n}{\tau_n}, \quad n_\infty = \frac{1}{1 + a_n}, \quad \tau_n = \frac{\beta_n}{q_t \cdot a0n \cdot (a_n + 1)}, q_t = q_{10}^{\left(\frac{\theta - 24}{10}\right)}$$

$$a_n = e^{0.001 \cdot \zeta \cdot \left(V - V_{half_n}\right) \cdot Q(\theta)}, \beta_n = e^{0.00039 \cdot \zeta \cdot \left(V - V_{half_n}\right) \cdot Q(\theta)}, \zeta = -1.8 - \frac{1}{1 + e^{\frac{V+40}{5}}}$$

$$\frac{dl}{dt} = \frac{l_\infty - l}{\tau_l}, \quad l_\infty = \frac{1}{1 + a_l}, \quad \tau_l = \max(0.26 \cdot (V + 50), 2)$$

$$a_l = e^{0.003 \cdot \left(V - V_{half_l}\right) \cdot Q(\theta)}$$

where activation and inactivation half potentials are $V_{half,n} = -1\, mV$ and $V_{half,l} = -56\, mV$, respectively. The $a0n = 0.1\, ms^{-1}$, and the temperature sensitivity is $q_{10} = 5$.

Finally, a calcium pump/buffering mechanism is inserted at the cell soma and along the apical and basal trunk. The kinetic equations are given by

$$drive_{channel} = max\left(-f^e \cdot \frac{I_{Ca}}{0.2 \cdot F}, 0\right), f^e = 10000, F = 9.648 \cdot 10^4 \text{ Coulomb/mole}$$

$$\frac{dca}{dt} = \frac{drive_{channel}}{18} + \frac{50^{-6} mM - ca}{2200 ms}$$

PERSONAL DATA

Name/Surname	**SPYRIDON CHAVLIS**
Address	N. Plastira 100, Vasilika Vouton
	GR 700 13, Heraklion, Greece
Contact number	(0030) 2810 391264
FAX	(0030) 2810 391101
E-mail	chavlis.spiros@gmail.com
	schavlis@imbb.forth.gr
Nationality	Greek

EDUCATION & TRAINING

Dec 2013 – ongoing: Institute of Molecular Biology & Biotechnology (IMBB), Foundation for Research & Technology Hellas (FORTH)

- **PhD** candidate in Computational Biology Laboratory (http://dendrites.gr/)
- **Subject:** Investigating the role of dendrites in sparse representations in the hippocampus using computational models
- **Supervisor:** Research Director Dr Panayiota Poirazi
- **MSc Student supervision:**
  - Theodoros Tamiolakis Investigating the role of area CA2 in social memory formation using computational and experimental approaches, Feb 2017 - ongoing
  - Michalis Pagkalos The role of denrites in pattern completion using a computational modeling approach, Aug 2017 - ongoing
  - Panagiotis Linardos Deep learning approaches inspired from biological systems, Jul 2017 - ongoing

Sept 2012 – Sept 2013: Department of Bioengineering, Imperial College London

- **MSc** in Biomedical Engineering – **Major:** Neurotechnology
- **Key modules:** Machine Learning & Neural Computation, Computational Neuroscience, Computational Neurodynamics, Brain Machine Interfaces, Biomedical Imaging, Image Processing, Systems Physiology, Statistics & Data Analysis
- **Master thesis:** "What is the information capacity of a synapse" supervised by Lecturer Dr A. Faisal
- **Overall Classification:** Distinction (71.2/100)

Oct 2004 – June 2011: School of Mechanical Engineering, National Technical University of Athens (NTUA)

- **Diploma** in Mechanical Engineering (equivalent to MSc) – **Major:** Energy Engineering
- **Key modules:** Radiation Protection and Dosimetry, Biomedical Engineering: Medical Imaging & Radiotherapy, Bio-Fluid Mechanics & Biomedical Engineering, Interactions of Ionizing Radiations with Matter, Computational Fluid Dynamics
- **Diploma thesis:** "Study on the performance of an XRF unit using Monte Carlo simulation code" supervised by Associate Professor M. Anagnostakis
- **GPA:** Very Good (7.5/10)
- Participated and presented my Diploma thesis in the workshop "CHERNE 2012" (http://cherne2012.ntua.gr)

Oct 2001 – June 2004: 1st High School (Lyceum) at Glyka Nera, Greece

- **GPA:** 19/20

WORK/PROFESSIONAL EXPERIENCE

Oct 2017 – Ongoing: Teaching Assistant in MSc in Bionformatics, Department of Medicine, University of Crete

- Introduction to Mathematics: Linear Algebra

Oct 2016 – Sep 2017: Teaching Assistant in MSc in Bionformatics, Department of Medicine, University of Crete

- Introduction to Programming with Python
- Methods in Bioinformatics (Machine Learning algorithms)

Mar 2016 – Apr 2016: Teaching Assistant in Animal Physiology Lab, Department of Biology, University of Crete

- Computational neuroscience, part of undergraduate course "Animal Physiology"

Oct 2004 – Aug 2010 & Oct 2011 – Aug 2012: Self-employed as a Personal Tutor to Junior High School & High School students

- Taught Subjects: Mathematics, Physics, Chemistry, Biology
- Supervised and motivated students for the National Greek Exams

Aug 2010 – May 2011: Soldier in Greek army (fulfilled mandatory military duties)

List of Publications

1. **S. Chavlis**, P. Poirazi "Pattern separation in the hippocampus through the eyes of computational modeling", Synapse 2017 (doi: 10.1002/syn.21972)
2. N.B. Danielson, G.F. Turi, M. Ladow, **S. Chavlis**, P.C. Petrantonakis, P. Poirazi, A. Losonczy "In Vivo Imaging of Dentate Gyrus Mossy Cells in Behaving Mice", Neuron 2017 (doi: http://dx.doi.org/10.1016/j.neuron.2016.12.019)
3. **S. Chavlis**, P.C. Petrantonakis, P. Poirazi. "Dendrites of dentate gyrus granule cells contribute to pattern separation by controlling sparsity", Hippocampus 2017 (doi: 10.1002/hipo.22675)

Conference Papers

1. Kousanakis E., Dollas A., Sotiriades E., Papaefstathiou I., Pnevmatikatos D.N., Papoutsi A.,Petrantonakis P., Poirazi P., **Chavlis S.**, Kastellakis G., An Architecture for the Acceleration of a Hybrid Leaky Integrate and Fire SNN on the Convey HC-2ex FPGA-Based Processor, FCCM 2017 (IEEE) (doi: 10.1109/FCCM.2017.51)

Conferences

1. **S. Chavlis**, P. Bozelos, W. Li, G. Turi, A. Losonczy, P. Poirazi. "Investigating the Role of VIP$^+$ Interneurons in Learning-Related Place Cell Dynamics in Hippocampal Area CA1", FENS Regional Meeting 2017, Pecs, Hungury (http://www.fensfrm.hu/)
2. T. Tamiolakis, **S. Chavlis**, P. Poirazi. "Elucidating the Role of Different CA3 Hippocampal Neurons in Pattern Completion Using Computational Modelling", HBIO 2017, Heraklion, Greece (https://hscbio.wordpress.com/conferences-when/2017-2/) (**Selected for oral presentation**)
3. **S. Chavlis**, P. Bozelos, W. Li, G. Turi, A. Losonczy, P. Poirazi. "Investigating the Role of VIP$^+$ Interneurons in Learning-Related Place Cell Dynamics in Hippocampal Area CA1", HBIO 2017, Heraklion, Greece (https://hscbio.wordpress.com/conferences-when/2017-2/)
4. **S. Chavlis**, P.C. Petrantonakis, P. Poirazi. "Granule cell dendrites enhance pattern separation in dentate gyrus", CAJAL Brain Prize Course 2016 - Bordeaux, France (http://www.bordeaux-neurocampus.fr/fr/formation-doctorale/ecoles/cajal-2016-hippocampus.html) (**Among 20 participants**)
5. **S. Chavlis**, P.C. Petrantonakis, P. Poirazi. "Granule cell dendrites enhance pattern separation in dentate gyrus", AREADNE 2016, Santorini, Greece (http://areadne.org/) (**Selected among 6 best posters for oral presentation**)
6. **S. Chavlis**, P.C. Petrantonakis, P. Poirazi. "The role of dendrites in pattern separation in the dentate gyrus", Dendrites 2016, Heraklion, Greece (http://www.dendrites2016.gr/))
7. **S. Chavlis**, P.C. Petrantonakis, P. Poirazi. "Investigating the role of dendrites in pattern separation:A computational approach", FENS Regional Meeting 2015, Thessaloniki, Greece (http://www.ffrm2015.com/))

PERSONAL SKILLS & COMPETENCES

Awards / Scholarships

- Scholarship, IMBB, FORTH (ERC grant: *dEMORY*, Dec 2013 - ongoing)
- Partial Scholarship from Hippocampus Journal to attend *CAJAL Brain Prize Course 2016 - The Hippocampus: from Circuits to Cognition*

Positions of Responsibility and Interests

- **Reviewer for:** PeerJ Journal (https://peerj.com/)
- **Member of:** Hellenic Society for Neurosciences - FENS, Organization for Computational Neurosciences

Languages

- **Greek** – native language
- **English** – full professional proficiency
  - Certificate of Proficiency in English - The University of Michigan (17 May 2009)
  - IELTS(Academic Module) - Overall 7.0 (21 July 2012)
- **Spanish** – limited working proficiency
  - B2–DELE-Instituto Cervantes (20 May 2012)

IT Skills

- Operating systems: Microsoft Windows, Linux (debian based)
- Main applications: MS Office Suite, Libre Office Suite
- Programming languages: Python, C, Fortran(basic)
- Neural Simulators: BRIAN, NEURON, NEST (basic)
- Mathematical applications: Matlab, Mathematica, Mathcad
- Other applications: AutoCAD, LaTeX

Driving License

- Category **B** (20 Aug 2005) – Full clean EU (Greek) License

Interests

- **Music**
  - Courses in electrical bass in an official conservatory (10 years)
  - Courses in jazz music theory & composition
- **Basketball**